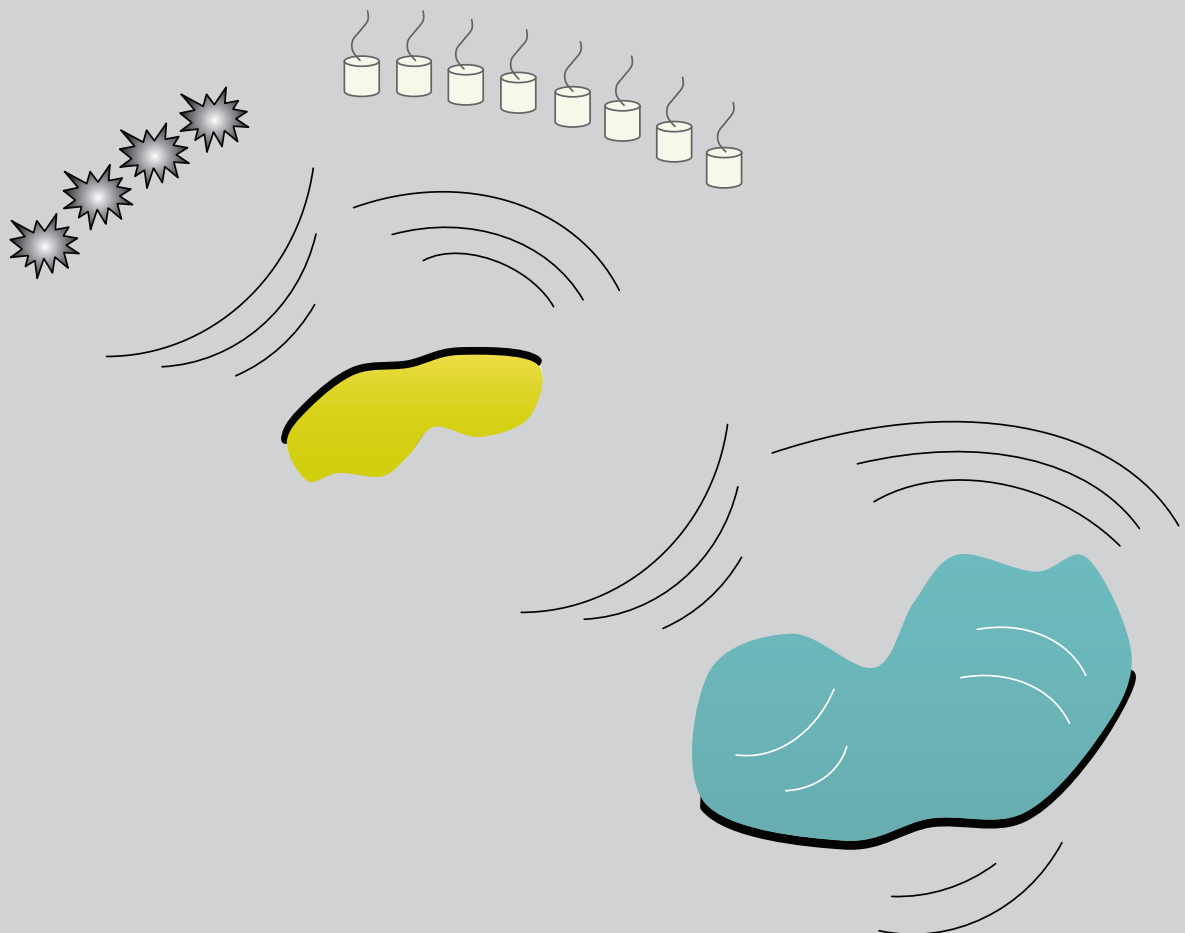


Ultrasound imaging for quantitative evaluation of magnetic density separation



Seyed Ali Sanaee

Ultrasound imaging for quantitative evaluation of magnetic density separation

Proefschrift

ter verkrijging van de graad van doctor
aan de Technische Universiteit Delft,
op gezag van de Rector Magnificus prof. ir. K.C.A.M. Luyben,
voorzitter van het College voor Promoties,
in het openbaar te verdedigen
op maandag 4 november 2013 om 10:00 uur

door

SEYED ALI SANAEE

Master of Engineering, Tohoku University, Japan
geboren te Tehran, Iran

Dit proefschrift is goedgekeurd door de promotoren:

Prof. dr. P.C. Rem

Prof. dr. ir. C.P.A. Wapenaar

Copromotor:

Dr. ir. M.C.M. Bakker

Samenstelling promotiecommissie:

Rector Magnificus,

voorzitter

Prof. dr. P.C. Rem,

Technische Universiteit Delft, promotor

Prof. dr. ir. C.P.A. Wapenaar,

Technische Universiteit Delft, promotor

Dr. ir. M.C.M. Bakker,

Technische Universiteit Delft, copromotor

Prof. dr. ir. R. Benedictus,

Technische Universiteit Delft

Prof. dr. G. Bonifazi,

Sapienza University of Rome, Italy

Prof. Dr-Ing. M.H. Tiorean,

Transilvania University of Brasov, Romania

Dr. ir. N. Fraunholcz,

Recycling Avenue BV, the Netherlands

Prof. dr. D.G. Simons,

Technische Universiteit Delft, reservelid

ISBN 978-90-5335-748-4

Copyright © 2013, by Seyed Ali Sanaee, Resources & Recycling, Faculty of Civil Engineering and Geosciences, Delft University of Technology, Delft, the Netherlands.

All rights reserved. No part of this publication may be reproduced, stored in a retrieval system or transmitted in any form or by any means, electronic, mechanical, photocopying, recording or otherwise, without the prior written permission of the author.

This research was financially supported by the European Commission in the framework of FP7 collaborative project “Magnetic sorting and ultrasound sensor technology for production of high purity secondary polyolefins from waste (W2Plastics)”.

Printed in the Netherlands by Ridderprint BV.

*This thesis is dedicated to my mother and father
for their kind support and encouragement.*

Contents

Chapter 1: Introduction	5
1.1 Research background	5
1.2 Research objectives.....	9
1.3 Research methodology	10
1.4. State of the art in acoustical imaging	11
References	13
Chapter 2: Ultrasound technology study.....	19
2.1. Imaging technologies	19
2.1.1. Principles of ultrasound imaging	19
2.1.2. Ultrasound sensors	21
2.1.3. Hydrodynamical probe casing	22
2.2. Signal processing	23
2.2.1. Ultrasound beam steering and focusing	23
2.2.2. Mid-end and back-end processing routines	25
2.3. Real-time ultrasound experiments	27
2.3.1. Real-time ultrasound imager.....	27
2.3.2. Image quality from experimental ultrasound	28
2.3.3. Data blending issues	31
2.4. MDS technologies and options for probe positioning	33
2.4.1. MDS technologies.....	33
2.4.2. Probe positioning	34
2.5. Quantitative analyses using real-time ultrasound	36
2.5.1. Image processing algorithms for PDD evaluation	37
2.5.2. Experiments in the MDS channel for PDD evaluation	39
2.5.3. Particle orientation, tracking and trajectory measurement.....	45
2.5.4. Materials identification	48
2.6. Evaluation of ultrasound imaging performance	50
References	51
Chapter 3: Linear acoustic theory for ferrofluids and plastics.....	53
3.1. Introduction.....	53
3.2. Equations of motion	54
3.3. Constitutive equation	55
3.4. The wave equation	57
3.5. Static pressure distributions and the MDS principle.....	58
3.6. Solutions to the wave equation	60
3.6.1. Plane waves.....	60
3.6.2. Green function.....	62
3.6.3. Specified Green functions	64

3.7. Acoustical characterization of polyolefin plastics	64
3.7.1. Attenuation in plastics.....	65
3.7.2. Measurement and classification of polyolefin groups	66
3.7.3. Signal strength in the MDS setting	69
3.7.4. Wave shielding due to critical refraction	71
References.....	73
Chapter 4: Ultrasound imaging in space-time domain.....	75
4.1. Introduction to imaging.....	75
4.2. Relation to the inverse scattering problem.....	76
4.3. Imaging principles.....	78
4.4. Time domain SAFT	80
4.5. Advancing on time domain SAFT	82
4.5.1. Aperture weighting	82
4.5.2. Adaptive weighting	83
4.5.3. Time-frequency domain SAFT	84
References.....	85
Chapter 5: Ultrasound imaging in the Fourier domain	87
5.1. Background and objectives	87
5.2. Fourier imaging overview	88
5.3. Wave field redatuming.....	91
5.3.1 Redatuming to a parallel plane interface.....	92
5.3.2 Redatuming to a sloping plane interface.....	94
5.4. F- SAFT	96
5.5. Stolt migration.....	96
5.6. SAFT and Redatuming	97
5.7. Phase shift migration.....	98
5.8. Non-stationary phase shift migration	100
5.9. Computational cost analysis of imaging algorithms	100
References.....	102
Chapter 6: Imaging performance	103
6.1. Data collection	103
6.2. Image quality.....	104
6.2.1. Sharpness and signal-to-noise-ratio	105
6.2.2. Spectral content of a dataset.....	107
6.3. Particle cross-section imaging	110
6.3.1. Imaging test objects	110
6.3.2. Principles of cross-section imaging	112
6.3.3. Acoustic information and signal strength	115
6.3.4. Cross-section imaging performance.....	119
6.4. Evaluation and recommendation for MDS applications	123
6.5. Statistics in online quantitative ultrasound	124

Chapter 7: Conclusions and recommendations	127
7.1. Conclusions	127
7.2. Recommendations	129
Appendices	131
A: Fourier transform	131
A.1. Fourier integral	131
A.2. Discrete Fourier Transform (DFT)	131
A.3. Parseval's theorem for DFT	131
B: Evaluation of complexity for imaging algorithms	132
Summary	135
Samenvatting	137
Acknowledgement	139
Curriculum Vitae	141

Chapter 1: Introduction

1.1 Research background

The recycling point of view

The presented work is an exploration into performance of ultrasound techniques, with a view towards development of ultrasound measurement tools for the recycling of solid wastes. A generic framework is developed for ultrasound evaluation of wet separation processes. In a wet separation technique, solid materials are processed in a fluid with the purpose of separating and sorting the different types of materials from the input waste mixture. As a special example, a breakthrough technology called *magnetic density separation (MDS)* has recently been developed. It uses ferrofluid to effectively separate materials, even when the mass densities are quite close. Moreover, in MDS the input waste mixture can be separated into multiple product streams in a single processing step. The requirement is that all the materials are either lighter than water or heavier than water, unless one is also content with products floating on the surface and sinking to the bottom (conventional sink-float principle).

A very early application of the basic principle of MDS is found in the recycling of mixed aluminium and copper scrap, which is relatively easy thanks to the large difference in mass density. The new developed MDS technology is a precision machine that promises to become the cost-effective method for the recycling of high quality products from waste, such as plastics and/or metals. The first target for MDS was the separation of the various polyolefin types originating from automobile waste, waste of electrical and electronic equipment (WEEE) and household waste [W2Plastics 2008]. A later MDS development targets plastics heavier than water and metals, in particular those from WEEE.

Plastic separation using traditional technology (e.g. sink-float) or sensor-based technology (e.g. infrared systems) is aimed at separating the end-of-life product, e.g. the whole plastic bottle or butter cup. This presents a problem, since different parts of a product may consist of different types of plastic (e.g. bottle cap, label and body). A big advantage of MDS in this respect is that the MDS feed requires the products to be shredded to smaller size, which also liberates the different plastics before separation. Note that the small particle size is required for MDS to ensure the uninterrupted flow of the ferrofluid.



Figure 1.1. Demonstration of the MDS principle. The lightest plastic balls float near the top and the heavier ones float deeper, i.e. closer to the magnet surface. The opaqueness of the ferrofluid is the reason for ultrasound imaging [W2Plastics 2008].

The reasons for the wide interest in thermoplastics are because they are well recyclable, have a high resale value, there is a lot of it going around and European plastic consumption is still increasing. For example, in 2005 already a total amount of 53 Mton plastics was produced, a third of which was polyolefin materials. It is well known that there are both environmental and economical motives for recycling plastics [Johansson 2007, Daiku 2001]. Separation of polyolefin types presents the highest challenge, because the specific mass densities are quite close and it requires advanced technology to separate them effectively.

In a MDS, the polyolefin waste particles are continuously fed (typically up to a 10000/s) into a straight channel in which a near-laminar flow of ferrofluid is maintained. The flow is led underneath a strong magnet that effectively creates a continuous, vertical mass density gradient in the ferrofluid [Bakker 2009]. Particles of different mass densities separate and equilibrate at different depths after which they can be extracted at the end of the channel using splitters and pumps to produce different output products in a single processing step. The basic physical principle of MDS is shown in Figure 1.1 where plastic balls of three different mass densities float at three distinctive equilibrium depths. An in-line monitoring system is required to visualize the moving particles in order to assess the separation performance. However, the ferrofluid is essentially black and optical camera systems proved useless. In contrast to light waves, acoustic waves have no such limitation, which led to the idea of developing an *ultrasound camera*. This motivated the present research into the performance of ultrasound imaging systems for the purpose of monitoring and quantitative analysis of the streams of polyolefin particles.

Acoustic imaging facts

The nature of acoustic wave propagation is employed in various fields for imaging inside opaque media where light waves cannot penetrate (cf. Figure 1.2). This has motivated the development of acoustical imaging methods, and mainly in the fields of medical ultrasound, seismic extrapolation and non-destructive testing (NDT). In medical diagnostics, one tries to visualize human tissues and organs. Acoustic research also has a long-standing history in exploration geophysics [Claerbout 1971, Claerbout 1976], where acoustic waves are used to study the internal earth layers. In NDT, ultrasound waves are transmitted into materials and structures to detect flaws, cracks and corrosion defects. Different types of sensors, instrumentation and frequency ranges are used in each field to match the requirements for measurement range and resolution. For example, geophones that are sensitive from a few Hz to a few kHz are used in reflection seismology to record sound energy, emitted by large seismic vibrators or dynamite sources, and reflected by internal geological layers. On the other hand, micron sized piezoelectric crystals are used to produce ultrasound waves for medical diagnostics inside arteries. In each field, the frequency range determines the achievable resolution and maximum depth of penetration. Typically, resolution is enhanced by increasing the frequency, which comes at the cost of a reduction in range, or depth of penetration, due to stronger attenuation of the higher frequencies. Therefore, the frequency range should be selected in a compromise to meet both resolution and range requirements. In seismic exploration, low frequencies between 5 and 100 Hz are used that can penetrate the earth's crust in the order of kilometres. In medical applications, high frequency ultrasound waves between 1 and 20 MHz may penetrate typically many centimetres down to just a millimetre or so into the human body, depending on the local properties of tissues.

Acoustical devices transmit waves inside the medium of interest. The incident waves are reflected at smooth material boundaries and/or scattered when the waves encounter a rough surface or material inhomogeneities smaller than the propagation wavelength. Imaging of surfaces may be based either on reflected waves, which have a directional dependence due to Snell's law, or scattering that seemingly can reflect the incident wave into many directions. It is therefore that all the main fields using ultrasound try to take full advantage of the possibility to use scattering as the main data for imaging. However, commercial thermoplastics, which are the subject of the current research, have the drawback that they are relatively homogeneous and also show little scattering due to the smooth polymer-chain build-up of the materials.

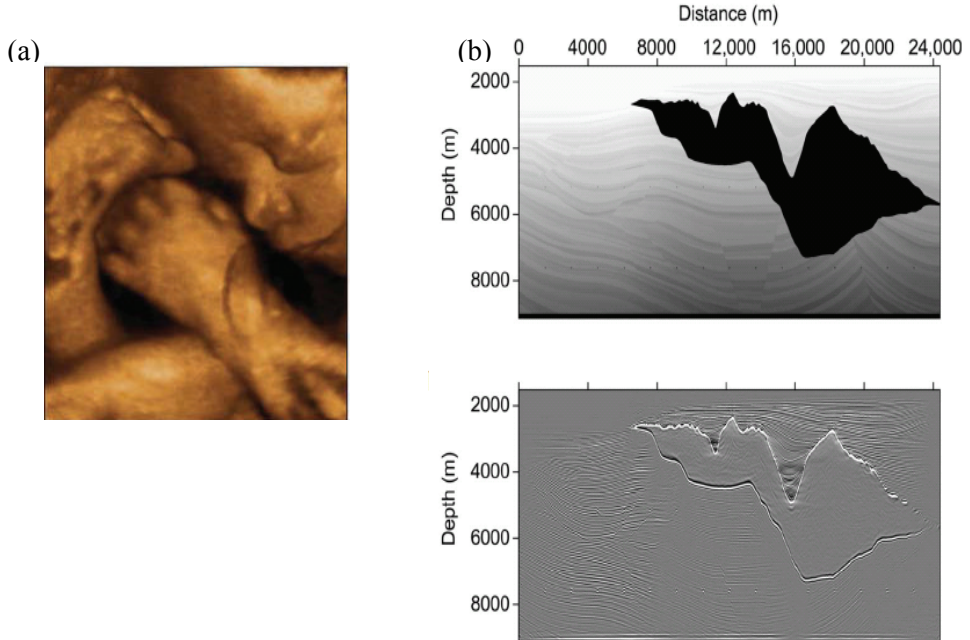


Figure 1.2. Acoustical imaging in medical diagnostics and geophysics. (a) 3D ultrasound image of the prenatal baby [Prager 2010]. (b) Top panel: a numerical velocity background model used for testing an imaging method in seismic extrapolation of a salt body representing a complex geologic structure. Bottom panel: image obtained using migration techniques [Wu 2008].

Imaging techniques rely on sensor positions to be favourably positioned with respect to the object and that these positions are accurately known in a common reference frame. Moreover, for many imaging methods it is mandatory that the sensors are evenly spaced along a line (or in a grid in case of 3D imaging). The acquisition of data from such accurately positioned sensors is greatly facilitated by sensor array technology. Besides the spatial distribution of the sensors, the information contained within a dataset is also determined by the bandwidth of sampled frequencies, which is mainly restricted by the sources and the finite bandwidth in which the sensors are sensitive.

From a mathematical and physical point of view, acoustical image forming is an inverse wave scattering problem [Devaney 1978]. In a forward linear acoustic problem all reflecting objects and medium properties are known and one calculates the resulting acoustic wave field. In the inverse case, one calculates the medium or object properties using only local measurements of the wave field. Where the forward linear problem is almost a trivial exercise, the inverse problem is non-linear and quite complex without even the guarantee that it can be solved uniquely. This underlying problem makes that imaging techniques, which are approximations

to this inverse problem, are not guaranteed to depict in all details the reality in which the dataset was collected.

The imaging technique is the link between the data and the final image. As a rule, the more the technique is based on physics, the better it can make good use of the wave information contained within the data, which should lead to a better result. Of course, it is inevitable that the calculation model used in imaging is less accurate, for example due to variations in wave velocity (temperature, pressure) or the estimated dimensions or position of boundaries and objects. The discrepancies between the calculation model and the true situation in which the data were scanned may also adversely affect the obtainable image quality.

1.2 Research objectives

The objectives of this thesis were to investigate and recommend fundamental concepts, techniques and technologies that are essential for realizing a real-time ultrasound system for wet recycling, dedicated to safeguarding and monitoring the quality of a waste separation process. That will involve basic monitoring of the critical areas of the separation medium and performing accurate analyses on the moving waste particles, which may lead to either quantitative or statistically accumulated MDS performance data.

The main challenge was to integrate the different fields of expertise and form the multidisciplinary basis that is typically required for research in sensor-based recycling technology. To give an indication of the research fields involved: acoustic theory on waves and fields, sensors and data processing technology, image forming techniques, image processing techniques, plastic waste processing and sorting technologies, and an intimate knowledge of plastic properties and the associated industrial waste recycling sector. At present, the field of recycling using ultrasound image forming and ultrasound quantitative analysis is just in its infancy, and very little literature can be found and most of the published works are specifically outcome of the present thesis [Ohtani 2006, Langton 1994, Bakker 2010, Sanaee 2011, Sanaee 2012-1, Sanaee 2012-2]. Because plastics are a major societal waste problem with an economic potential, the techniques investigated in this thesis are aimed at wet plastic waste processing. As an additional technical advantage, the separation liquid provides an excellent acoustic coupling to the ultrasound sensor probe. Arguably, the results from this research may lead to the first implementation of a quantitative ultrasound monitoring system designed for recycling. The type and bulk of materials and the processing applications and conditions found in recycling are very different from those found in other fields where ultrasound is already accepted as a key technology. Therefore, recycling will open up an entirely new field of ultrasound research, which requires new ideas and new perspectives on quantitative ultrasound.

1.3 Research methodology

As a first step in the building of the research framework, the possibilities and implications of introducing and operating a real-time ultrasound system in an industrial setting were investigated. For that purpose medical ultrasound technology was adapted, which as a commercially available type of machine has a high level of technology readiness. A portable, high-end class 2D medical imaging machine was chosen on the basis of image quality versus costs, which excluded for example the very expensive 3D imaging technology. The sensor probes were chosen, and modified where needed, to meet the limitations set by the MDS. Specific attention went to the limited accessibility of the channel for sensor probes and there were initial worries about the laminar ferrofluid flow. The potential of real-time ultrasound could now be established and demonstrated for both qualitative and (semi-) quantitative evaluations. A complication for the dominantly experimental part of this investigation was that the MDS technology itself was still under investigation to reach satisfactory laminar ferrofluid flow and separation performance. In fact, the MDS prototype was perfected only in the last months of the ultrasound project. The problem was that the MDS is simply unique, in that there is no other technology that can make different plastic particles float steadily at different depths in a liquid. Simple options such as oil-water layers in a basin were soon discarded as either unpractical or unrealistic. Therefore, the early research was performed in water tanks in the laboratory using particles on strings or pinned down on thin sticks to simulate the free floating behaviour, while the real in-situ MDS ultrasound results date from quite late in the project.

As a second part of the research, the theory of acoustic wave propagation in fluids is set up and a link between the fundamental inverse scattering problem and the physically better tractable imaging concept is investigated. Following this part of the framework, the general imaging concept is expanded into different imaging techniques and implemented in Matlab. This research benefited greatly from adapting the technologically promising parts of the state-of-the-art in acoustical imaging, developed in research fields such as medical ultrasound diagnostics, seismic exploration and non-destructive testing. The ultrasound data for the experimental part of this research was acquired from static scenes using generic test objects to represent the widely varying properties of waste particles in a dedicated laboratory setup. As a major step towards quantitative shape and size analysis of waste particles, the focus was on particle cross-section imaging.

A fundamental question within the research framework was the relation between the acoustical information contained in the ultrasound data, the capability of the imaging technique itself to make full use of that information, and the resulting ultrasound image quality. First, this research question was made more specific by using representative test objects, two complementary types of data set and a few of the most promising imaging techniques. In addition, the rather subjective matter of assessing image quality has been settled by evaluating the image in terms of performance indicators such as sharpness and shape consistency.

Based on the findings, recommendations could be given for the optimum use of ultrasound techniques in the next generation of solid waste recycling technology.

1.4. State of the art in acoustical imaging

The knowledge, knowhow and research advances in fields active in ultrasound imaging, and which are deemed most relevant to the present research, are discussed. To structure the vast literature on this topic, it is subdivided into four subparts: Ultrasound sensor technology, Imaging techniques, Data blending and Non-destructive testing (NDT).

Ultrasound sensor technology: Medical diagnostics shows an extensive body of research on ultrasound volumetric imaging of time varying objects, such as a beating heart. To produce the high resolution 3D images, rows of 2D sensor arrays, called *matrix arrays*, with on-board integrated electronics are under development. The manufacturing of these arrays is and remains a technological challenge because of the very high number of small elements contained in a matrix and the complexity of connecting them to the outside world. For example, if a 1D linear array has 128 elements, its 2D version will have $128 \times 128 = 16384$ elements, of which its huge amount of data puts a large burden on the processing hardware. Based on the spatial sampling requirement, the maximum width of a sensor element must be smaller than half the acoustic propagation wavelength ($300 \mu\text{m}$ for water at 5 MHz). For a 1D array this condition needs to be satisfied in just one dimension. However, for 2D arrays the condition must be satisfied in two directions, which restricts the achievable element size and complicates the manufacturing process. Progress on 2D sensor arrays may be found in [Oralkan 2003, Wygant 2008].

The development of high frequency ultrasound sensor arrays is mainly a response to the need for increased resolution. For example, in medical fields such as dermatology and ophthalmology to detect smaller anomalies, or in NDT for the purpose of improved fatigue crack sizing. Similar as for densely packed 2D arrays, the technological challenge is in being able to control the forming of tiny details from the brittle piezoelectric materials. A recent work [Liu 2012] has reported on a 50 MHz linear sensor array of 32 elements, each $24 \mu\text{m}$ wide at $36 \mu\text{m}$ pitch.

Sensor array technology with integrated electronics, which reduces equipment size and influences of ambient noise, can deliver more performance compared to costs. This means that the technology can become better and relatively cheaper with each generation, which is quite important when considering the expected return on investment and ultimately the acceptance of ultrasound quality inspection systems in the waste recycling industry.

Imaging techniques: A piezoelectric sensor array allows each sensor element to act as either transmitter or receiver. As a result, a *full dataset* of a linear array of N elements may acquire N^2 measurements, about half of which are redundant due to

the principle of reciprocity. A recent tendency is to use the full dataset in NDT and medical ultrasound imaging to improve image quality. An imaging method that can flexibly utilize the many permutations of transmitter and receiver positions is called synthetic aperture imaging [Jensen 2006, Trots 2010], which is essentially equal to SAFT, cf. Section 4.4. Although the possible benefits for image quality are duly recognized, the heavy computational overhead of this method has been a major drawback for its real-time implementation. A recent work has implemented the full dataset imaging in a wavenumber-frequency domain approach, which reduces the computational burden [Hunter 2008].

The image quality delivered by the conventional delay-and-sum beamforming methods can be tuned by introducing either aperture weights or adaptive weighting factors. Several methods have been proposed by researchers to further enhance the resolution and signal-to-noise-ratio of ultrasound images [Liao 2004] [Li 2003]. These methods are adaptive, meaning that the weighting factors are determined by the information carried by the data signals. Application in a high frequency ultrasound system has been demonstrated [Li 2004].

Achieving higher frame rates in ultrasound imaging has been investigated for its use in medical applications. An ultra high rate of 1000 frames per second has been reached by applying plane wave data [Montaldo 2009]. A recent study focused on beamforming of ultrasound plane wave data and imaging in the Fourier domain [Kruizinga 2012], which is potentially faster. The proposed method used a nonuniform fast Fourier transform (NUFFT) which reduced the computational burden.

A depth migration technique in seismic exploration maps recorded acoustic data into an image that should give a quantitative and accurate model of the layers of the earth crust. The state-of-the-art in seismic imaging is 3D depth migration of subsurface structures where each layer may have different wave velocity, density or anisotropic properties [Etgen 2009]. In principle, the depth migration technique requires an accurate velocity model of the subsurface structures to produce such a detailed image. But in an iterative approach the migration method may be used to build and estimate this *a priori* unknown velocity model. The disadvantage is that this defines a nonlinear imaging scheme, which may have the same drawbacks as the nonlinear inverse scattering problem.

Data blending: In a typical seismic acquisition survey the time intervals between firing two sources is taken long enough as to avoid the interference of different source responses in time. The number of shots is also kept to minimum to reduce the material costs and the survey time, which is associated with the high personnel costs. This means that the source domain is not always adequately sampled, in which case interpolation is performed to simulate the missing shot records. Recently, a new data acquisition strategy called *blending* has been developed in a response to overcome the data acquisition limitations [Beasley 1998, Berkhout 2008]. In blending acquisition, short time-delays are applied between firing sources, which results in overlapping multi-source responses in time. Processing has to be

applied to the blended data to reproduce the *deblended* data, which is then suitable for standard seismic imaging techniques. It has also been shown that the blended data may be directly processed in seismic migration techniques [Verschuur 2009]. Data blending offers mainly two advantages compared to conventional acquisition methods. First, the image quality is improved since the spatial source sampling may be denser by which the target is illuminated under many more different viewing angles. Secondly, the data acquisition survey time may be reduced since shots are repeated more quickly, which reduces costs.

Non-destructive testing (NDT): During the last three decades, the NDT community has seen the introduction of ultrasound imaging methods, specifically time domain SAFT [Doctor 1986] and frequency domain methods [Langenberg 1986, Busse 1992]. The degree of success of these methods is widely varying but the industry is still experimenting with different techniques and technologies, for example imaging defects by using inverse wave field extrapolation [Portzgen 2007]. It is also shown that images may be obtained from mode converted waves in metal structures by applying the proper wave velocity of the corresponding mode converted wave in the imaging process [Portzgen 2008]. In other examples, the beam profile of a finite-sized transducer may be included in the frequency-domain model to enhance spatial resolution [Stepinski 2007], which is a well-known compensation technique in an attempt to model the physics more closely. Recent work has extended the frequency domain methods to deal with complicated imaging geometries and configurations [Olofsson 2010, Skjelvareid 2011]. In other NDT related work the focus is on anisotropic materials [Spies 2003]. Judging from the intensity and level of research into ultrasound imaging, it is concluded that the NDT community has not widely profited from the initial introduction of imaging techniques. It is only the last decade or so that ultrasound imaging is in the forefront of research and NDT technology development. Most likely this increased interest is sparked by the significant improvements in performance of ultrasound imaging hardware and software and its wider availability.

References

- [Bakker 2009] E. J. Bakker, P. C. Rem, and N. Fraunholcz, Upgrading mixed polyolefin waste with magnetic density separation, *Waste Management*, Vol. 29, Issue 5, pp. 1712-1717, May 2009.
- [Bakker 2010] M. C. M. Bakker and S. A. Sanaee, Capabilities of Ultrasound for Monitoring and Quantitative Analysis of Polyolefin Waste Particles in Magnetic Density Separation (MDS), *The Open Waste Management Journal*, Vol. 3, pp. 117-126, 2010.

[Beasley 1998] C. J. Beasley, R. E. Chambers and Z. Jiang, A new look at simultaneous sources: *68th Annual International Meeting, SEG, Expanded Abstracts*, pp 133-135, 1998.

[Berkhout 2008] A. J. Berkhout. Changing the mindset in seismic data acquisition, *The Leading Edge*, 27, pp. 924-938, 2008.

[Busse 1992] L. J. Busse. Three-dimensional imaging using a frequency-domain synthetic aperture focusing technique, *IEEE Transactions on Ultrasonics, Ferroelectrics, and Frequency Control*, Vol. 39, No.2, pp. 174-179, March 1992.

[Claerbout 1971] J. F. Claerbout, Toward a unified theory of reflector mapping, *Geophysics*, Vol. 36, No. 3, pp. 467-481, June 1971.

[Claerbout 1976] J. F. Claerbout, *Fundamentals of geophysical data processing*, McGraw-Hill Book Co., Inc., New York, 1976.

[Daiku 2001] H. Daiku, T. Inoue, M. Tsukahara, H. Maehata, and K. Kakeda, Electrostatic separation technology for waste plastics – development of a high-purity type separator for plastics, *Proceedings of the Second International Symposium on Environmentally Conscious Design and Inverse Manufacturing*, pp. 562-565, Tokyo, December 2001.

[Devaney 1978] A. J. Devaney, Nonuniqueness in the inverse scattering problem, *J. Math. Phys.* 19 (1978), pp. 1526-1531.

[Doctor 1986] Doctor, S.R., Hall, T.E., Reid, L.D. SAFT- the evolution of a signal processing technology for ultrasonic testing, *NDT International* 19 (3), pp. 163-167, 1986

[Etgen 2009] John Etgen, Samuel H. Gray and Yu Zhang. An overview of depth imaging in exploration geophysics, *Geophysics*, Vol. 74, No.6, pp. WCA5-WCA17, November-December 2009.

[Hunter 2008] Alan J. Hunter, Bruce W. Drinkwater and Paul D. Wilcox. The Wavenumber Algorithm for Full-Matrix Imaging Using an Ultrasonic Array, *IEEE Transactions on Ultrasonics, Ferroelectrics, and Frequency Control*, Vol. 55, No.11, pp. 2450-2462, November 2008.

[Jensen 2006] Jorgen Arendt Jensen, Svetoslav Ivanov Nikolov, Kim Lokke Gammelmark and Morten Hogholm Pedersen. Synthetic aperture ultrasound imaging, *Ultrasonics*, Vol. 44, pp. 5-15, 2006.

[Johansson 2007] J. E. Johansson. Plastics – the compelling facts and figures, Proceedings of the *Sixth IdentiPlast Biennial Conference on the Recycling and Recovery of Plastics*, Brussels, 2007.

[Kruizinga 2012] Pieter Kruizinga, Frits Mastik, Nico de Jong, Antonius F. W. van der Steen and Gijs van Soest. Plane-Wave Ultrasound Beamforming Using a Nonuniform Fast Fourier Transform, *IEEE Transactions on Ultrasonics, Ferroelectrics, and Frequency Control*, Vol. 59, No.12, pp. 2684-2691, December 2012.

[Langenberg 1986] K. J. Langenberg, M. Berger, Th. Kreutter, K. Mayer and V. Schmitz. Synthetic aperture focusing technique signal processing, *NDT International*, Vol. 19, Issue 3, pp. 177-189, June 1986.

[Langton 1994] C. M. Langton, J. B. Hull, S. Braker and A. R. Jones. Identification and characterization of reclaimed and recycled polymers by ultrasound attenuation, *Journal of Alloys and Compounds*, Vol. 211-212, pp. 419-423, September 1994.

[Li 2003] Pai-Chi Li and Meng-Lin Li. Adaptive Imaging Using the Generalized Coherence Factor, *IEEE Transactions on Ultrasonics, Ferroelectrics, and Frequency Control*, Vol. 50, No.2, pp. 128-141, February 2003.

[Li 2004] Meng-Lin Li, Wei-Jung Guan and Pai-Chi Li. Improved Synthetic Aperture Focusing Technique with Applications in High-Frequency Ultrasound Imaging, *IEEE Transactions on Ultrasonics, Ferroelectrics, and Frequency Control*, Vol. 51, No.1, pp. 63-70, January 2004.

[Liao 2004] C.-K. Liao, M.-L. Li and P.-C. Li. Optoacoustic imaging with synthetic aperture focusing and coherence weighting, *Optics Letters*, Vol. 29, No.21, pp. 2506-2508, November 1, 2004.

[Liu 2012] Changgeng Liu, Qifa Zhou, Frank T. Djuth and K. Kirk Shung. High-Frequency (>50 MHz) Medical Ultrasound Linear Arrays Fabricated From Micromachined Bulk PZT Materials, *IEEE Transactions on Ultrasonics, Ferroelectrics, and Frequency Control*, Vol. 59, No. 2, pp. 315-318, February 2012.

[Montaldo 2009] Gabriel Montaldo, Mickael Tanter, Jeremy Bercoff, Nicolas Benech and Mathias Fink. Coherent Plane-Wave Compounding for Very High Frame Rate Ultrasonography and Transient Elastography, *IEEE Transactions on Ultrasonics, Ferroelectrics, and Frequency Control*, Vol. 56, No. 3, pp. 489-506, March 2009.

[Ohtani 2006] K. Ohtani and M. Baba, An Identification Approach for Object Shapes and Materials Using an Ultrasonic Sensor Array, *The Proceedings of SICE-ICASE International Joint Conference*, pp. 1676-1681 Busan, 2006.

[Olofsson 2010] Tomas Olofsson. Phase Shift Migration for Imaging Layered Objects and Objects Immersed in Water, *IEEE Transactions on Ultrasonics, Ferroelectrics, and Frequency Control*, Vol. 57, No.11, pp. 2522-2530, November 2010.

[Oralkan 2003] Omer Oralkan, A. Sanh Ergun, Ching-Hsiang Cheng, Jeremy A. Johnson, Mustafa Karaman, Thomas H. Lee and Butrus T. Khuri-Yakub, Volumetric Ultrasound Imaging Using 2-D CMUT Arrays. *IEEE Transactions on Ultrasonics, Ferroelectrics, and Frequency Control*, Vol. 50, No. 11, pp. 1581-1594, November 2003.

[Prager 2010] R. W. Prager, U. Z. Ijaz, A. H. Gee and G. M. Treece. Three-dimensional ultrasound imaging, *Proceedings of the Institution of Mechanical Engineers*, pp. 193-224, 2010.

[Portzgen 2007] Niels Portzgen, Dries Gisolf and Gerrit Blacquiere. Inverse Wave Field Extrapolation: A Different NDI Approach to Imaging Defects, *IEEE Transactions on Ultrasonics, Ferroelectrics, and Frequency Control*, Vol. 54, No.1, pp. 118-127, January 2007.

[Portzgen 2008] Niels Portzgen, Dries Gisolf and Dirk J. Verschuur. Wave Equation-Based Imaging of Mode Converted Waves in Ultrasonic NDI, with Suppressed Leakage from Nonmode Converted Waves, *IEEE Transactions on Ultrasonics, Ferroelectrics, and Frequency Control*, Vol. 55, No.8, pp. 1768-1780, August 2008.

[Sanaee 2011] S. A. Sanaee and M. C. M. Bakker. Ultrasound Techniques for Control and Quantitative Measurements in Density Separation of Polyolefins, *The Proceedings of the International Conference on Solid Waste 2011-Moving Towards Sustainable Resource Management*, Hong Kong SAR, P. R. China, 2-6 May 2011.

[Sanaee 2012-1] Seyed Ali Sanaee and M. C. M. Bakker. Ultrasound imaging techniques in density separation of polyolefin waste, *Environmental Technology*, vol. 33, no. 22, pp. 2585-2593, November 2012.

[Sanaee 2012-2] Seyed Ali Sanaee and Maarten C. M. Bakker. Ultrasound Imaging for Quantitative Measurement of Immersed Plastic Waste Particles, *The Proceedings of 18th World Conference on Nondestructive Testing*, Durban, South Africa, 16-20 April 2012.

[Skjelvareid 2011] Martin H. Skjelvareid, Tomas Olofsson, Yngve Birkelund and Yngvar Larsen. Synthetic Aperture Focusing of Ultrasonic Data From Multilayered Media Using an Omega-K Algorithm, *IEEE Transactions on Ultrasonics, Ferroelectrics, and Frequency Control*, Vol. 58, No.5, pp. 1037-1048, May 2011.

[Spies 2003] Spies, M. and Jager, W. Synthetic aperture focusing for defect reconstruction in anisotropic media, *Ultrasonics* 41 (2), pp. 125-131, 2003.

[Stepinski 2007] Tadeusz Stepinski. An Implementation of Synthetic Aperture Focusing Technique in Frequency Domain, *IEEE Transactions on Ultrasonics, Ferroelectrics, and Frequency Control*, Vol. 54, No.7, pp. 1399-1408, July 2007.

[Trots 2010] Ihor Trots, Andrzej Nowicki and Marcin Lewandowski. Synthetic Transmit Aperture Method in Medical Ultrasonic Imaging. *World Academy of Science, Engineering and Technology*, Vol. 64, pp. 294-297, 2010.

[Verschuur 2009] D. J. Verschuur and A. J. Berkhouit. Target-oriented, Least-squares Imaging of Blended Data. *Proceedings of 2009 SEG Annual Meeting*, pp. 2889-2893, Houston, 25-30 October 2009.

[Wu 2008] Ru-Shan Wu, Yongzhong Wang and Mingqiu Luo. Beamlet migration using local cosine basis, *Geophysics*, Vol. 73, No. 5, pp. S207-S217, September-October 2008.

[Wygant 2008] Ira O. Wygant, Xuefeng Zhuang, David T. Yeh, Omer Oralkan, A. Sanli Ergun, Mustafa Karaman and Butrus T. Khuri-Yakub. Integration of 2D CMUT Arrays with Front-End Electronics for Volumetric Ultrasound Imaging, *IEEE Transactions on Ultrasonics, Ferroelectrics, and Frequency Control*, Vol. 55, No. 2, pp. 327-342, February 2008.

[W2Plastics 2008] Website of W2Plastics 2008. Available at <http://www.w2plastics.eu>.

Chapter 2: Ultrasound technology study

2.1. Imaging technologies

2.1.1. Principles of ultrasound imaging

Ultrasound refers to a sound wave with frequencies beyond the range of the human ear, which is approximately 20 kHz. Imaging refers to a technique for visualizing surfaces in direct view of the sensors and discriminating objects in three-dimensional space. Ultrasound imaging technology has proven a powerful tool in monitoring applications and quality inspection. It finds its application in fields such as medical diagnostics and non-destructive testing, e.g. materials evaluation or integrity inspection of structures.

Medical ultrasound technology has been under development since the 1950s. During the last decades the capabilities of electronics and computational power of the microprocessor have increased enormously, allowing for ultrasound to turn into an even more widely applied imaging tool. For example, advanced medical ultrasound imagers are portable and relatively inexpensive and therefore provide the best point of departure for real-time MDS ultrasound research. They provide high resolution images with real-time capability, allowing for in-situ capturing of images and video streams, typically at a rate of 25 images per second. The images are commonly captured using a 1D-linear array (*probe*), resulting in a 2D image showing the reflection maps retrieved from a sheet-window of observation. The state-of-the-art focuses on the development of 3D imaging using a 2D matrix of sensors. Such a matrix with its many sensors produces a huge amount of data that demands a massive increase in computational power. Since the processing hardware is the most expensive part of the ultrasound system, this means that 3D imaging technology may only become economically viable for applications in the recycling industry in some ten years time.

Medical ultrasound imaging is based on waves reflected back to the sensor array, which requires just one probe. This may be compared to the transmitted waves, which detection would require two probes to be positioned in front and behind the object that is to be imaged, unless it would be possible to position some kind of strong reflector behind the object [Carson 1977]. The following steps are essential for creating a 2D reflection image in a medical application. First, the probe with its many small piezoelectric sensors, now approximating point sources, are excited to produce ultrasound waves, which typically range between 2 and 20 MHz. Sound waves are scattered when propagating in and out of the different human tissues with their different acoustic properties, e.g. organs, blood vessels, fat or bone. With each change in tissue the reflected and transmitted waves will travel in a new direction in accordance with Snell's law, provided the different tissues are homogenous and have a smooth interface. Otherwise, if the encountered tissue is strongly scattering, the incident acoustic wave will be scattered in all directions.

Some of the reflected acoustic energy will find its way back to the probe, which sensors now function as receivers (and approximate point receivers) to record the signals. If the wave propagation speed in each type of tissue is known, one may calculate the distance from the probe where the reflections occurred. The detected waves also carry useful information in their amplitude and frequency content (i.e. the spectrum), which may be employed to identify the type of materials encountered by the detected sound waves.

An imaging algorithm processes the data on the basis of their temporal and spatial information and constructs the 2D image, which reveals details of the scanned part of the human interior as variations in pixel intensity. Filtering operations may be carried out on the obtained image to reduce noise or to enhance the visibility of small details that support the sonographer in his diagnosis. The software also allows the raw ultrasound data to be represented as *modes* to facilitate their interpretation. A medical imager typically offers the following modes:

- A-mode: refers to a 1D *A-scan* plot or *Amplitude plot*, indicating the distance of an object from the sensor array. Imaging is achieved by multiplying recorded time with half the wave speed of the homogenous medium in between the reflector and the sensor arrays.
- B-mode: refers to a 2D *B-scan* image or *Brightness-mode image*. The sensors in a linear array scan the data in a 2D plane in response to a single acoustic pulse. The B-scan shows the received amplitudes as pixel intensities.
- M-mode: also known as *Motion-mode* is where a high pulse repetition is used to show the mechanical motions of boundaries, such as the heart pumping. This is achieved by showing a sequence of B-mode or A-mode scans in real-time, usually in response to all sensors being fired at the same time.

A major advantage in the medical field is the flexibility by which the sonographer can access the interior of the patient, i.e. the probe may be easily moved along the skin to obtain the best view of the problem area. This kind of flexible access will not be possible in an industrial MDS setting. The probe has far less manoeuvrability in the narrow separation channel, it is not allowed to cause significant turbulence and, moreover, due to the speed of the moving polyolefin particles there is no time for any human operator to obtain the best view on a specific particle of choice. These issues must be solved for a successful application of ultrasound imaging to MDS.

2.1.2. Ultrasound sensors

Most ultrasound sensors employ the electro-mechanical energy conversion behaviour of piezoelectric materials to produce and detect acoustic waves. In transmission, the piezoelectric element is excited by a high voltage pulse (100V/100 ns) to generate acoustic waves. In detection, the sensor converts part of the incident acoustic energy into a varying electric charge over the piezoelectric crystal, which is converted to a detectable voltage using an electronic amplification circuit. This results in a signal which voltage is proportional to the strength of the detected acoustic wave. The brittle and thin piezoelectric element is covered by a protecting layer that also matches its high acoustical impedance (PZT: $3e7 \text{ kgm}^{-2}\text{s}^{-1}$) to the lower impedance of the external propagation medium (water: $1.5e6 \text{ kgm}^{-2}\text{s}^{-1}$). Depending on the application, the sensor may also be fitted with an acoustical lens to fix a focal depth. The back surface of the piezoelectric element is glued to a backing material that broadens the bandwidth of the sensor through vibration damping. As a single sensor unit this assembly is commonly referred to as *transducer*, while for a linear array incorporating many small sensor elements the assembly is usually referred to as *a probe* or *an array*.

A single transducer is called a *piston-transducer* if it is sensitive to surface-normal deformations, for which the piezoelectric crystal axis should be aligned accordingly. The complementary type is called a *shear wave transducer* as it is most sensitive to horizontal (in-plane) shear deformations. The single transducer is commonly encased in a robust steel housing and requires of course just one data acquisition channel. However, to produce a 2D scan with a transducer requires mechanical scanning capability, which results in a much lower acquisition speed than offered by arrays. The possibility to perform fast and accurate line scans makes the sensor array a superior technology for imaging.

Linear sensor arrays contain typically 32–128 sensors arranged in a straight line. The sensors can be excited or read, either individually or in groups of typically 4 to 16 sensors. The timing specifications for exciting and/or reading the subsequent sensor groups will produce different ultrasound beam characteristics. Using this option, the direction and/or focus of the produced or sensing acoustic beam can be changed electronically.

Figure 2.1 shows how a single piezoelectric plate can be used to produce an array. The material, matching layers and backing material are first bonded to a sandwich-like structure. Besides improving the bandwidth, the backing material also absorbs vibrations that may enter the probe casing. A saw blade cuts into the sandwich structure to produce the spacing between the sensors. The element thickness d determines the resonance frequency of the crystal, i.e. the centre frequency of the sensor. Several matching layers must be attached to the exposed side of the crystal to achieve the required impedance matching between the sensors and the external propagation medium. On top of the matching layers an acoustic lens may be attached for elevation focusing (cf. Figure 2.3), which limits the sensitivity of the sensors to a sheet-window of observation.

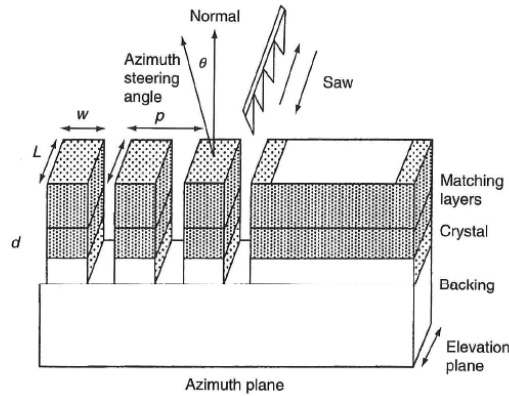


Figure 2.1. A sandwich structure is diced by a saw to create multiple sensor elements [Szabo 2004].

2.1.3. Hydrodynamical probe casing

The commercial medical probes are designed for handheld operation, which has led to ergonomic probe casings. However, to function inside a flowing liquid without causing significant turbulence it should be hydrodynamic instead. Here, for efficiency, it was chosen to adapt the complete interior sensor array and cabling of a commercial probe and only modify its plastic casing. It is noted that, in view of the flatness of the sensor part of the probe, it could never be employed in a view against the flow. A more hydrodynamic design for the probe casing was produced with rapid prototyping. The concept is illustrated in Figure 2.2. The retrofitted plastic casing created a more hydrodynamic back and sides, which allowed the probe to be used in viewing directions with the flow and normal to the flow.

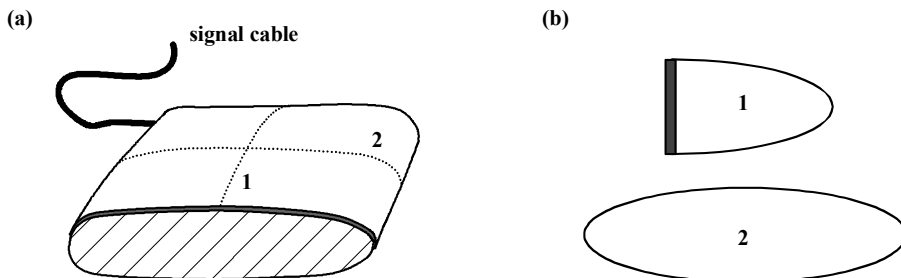


Figure 2.2. (a) Hydrodynamic improvement for the probe casing. (b) Cross sections indicated in (a)

2.2. Signal processing

2.2.1. Ultrasound beam steering and focusing

A linear array offers the possibility to manipulate its sensitivity profile by means of electronic time delays (or phase delays) during data collection or, in a reciprocal way, during excitation. The beam profile of a row of sensors depends on the individual sensor size, the number of sensors that can be fitted within a propagation wavelength and on the time delay applied to each sensor. The wavelength should be longer than three times the size of a sensor to allow for effective beam steering. By applying time delays the energy may be enhanced in a predefined direction or focused in a predefined point in space. The typical profile for a group of elements in an array is shown in Figure 2.3.

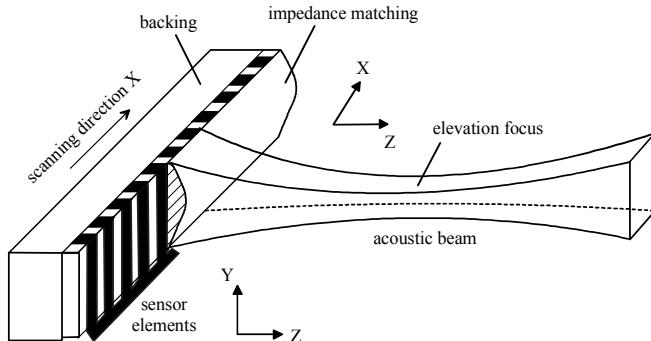


Figure 2.3. Beam steering in the xz -plane is produced by applying time delays to the sensors. The beam profile in the yz -plane is fixed to create an elevation focus, complying with the near field limit.

The two distinctive acoustic regions of a sensor or a group of combined sensors are called *near field* and *far field*. In the near field the beam first narrows and approximately assumes the width of the sensor or the combined group of sensors. Here the beam is essentially composed of intricate interference patterns produced by the different frequencies in the wave field. After a distance, called the *near field limit*, the beam diverges at which point the acoustic pressure distribution becomes quite smooth and much better predictable. This is the far field pattern. For a single, round sensor the near field limit may be determined as

$$d_{\text{nearfield}} = a^2/\lambda, \quad \text{Eq. (2.1)}$$

where a is the radius of the sensor and λ the propagation wavelength. The formula gives more generic insight, because it shows that the beam is sharper when more sensors are combined and effectively create one large sensor. Thus, combining sensors narrows the beam but enhances the sensitive range of the probe. In Figure 2.3 a sensor group produces a 3D beam which may be analysed in the xz and yz cross sections. The acoustic elevation focus (or near field limit) determines the fixed, narrow beam in the yz -plane. By grouping and timing sensors the width and direction of the beam may be steered in the xz -plane. An ultrasound image is formed by transmitting a beam under a range of angles, gathering the reflection data and subsequently delaying and summing these data to achieve synthetic focusing in all the relevant observation points.

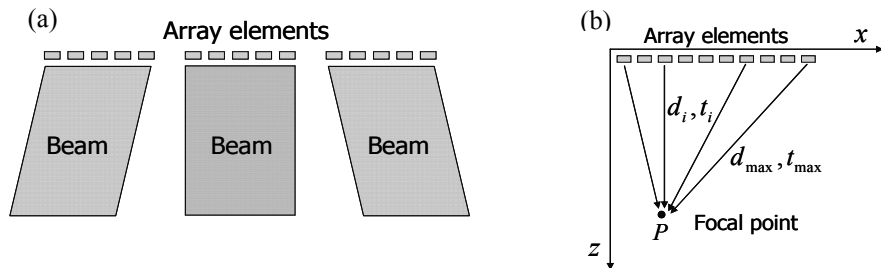


Figure 2.4. (a) Beam steering for a linear array affects the direction of the window of observation. This is achieved by exciting the sensors with predefined time-delayed pulses.

Beam forming may be divided in steering and focusing. In beam steering the direction of the beam follows from Huygens's principle, by which the wave front may be thought to be synthesized from the interference of many elementary point source excitations. The required time-delays in sequential firing of the elements to achieve steering in direction θ is

$$\Delta t = d \sin \theta / c . \quad \text{Eq. (2.2)}$$

Here, d is the distance between the centres of neighbouring sensor elements, or the distance between the centres of groups of elements, and c is the wave propagation velocity. When steering, the beam spans either a rectangular or a parallelogram shaped window of observation, as shown in Figure 2.4(a).

In ultrasound focusing the sensors are also excited with calculated time-delays, but with the purpose of colliding the arrival times (in-phase) in a given point in space. Figure 2.4(b) shows the principle. The propagation time it takes the wave to travel the one-way distance d_i from sensor element i to the focus is given by

$$t_i = d_i/c . \quad \text{Eq. (2.3)}$$

To collide all waves in the focal point takes time delays according to

$$\Delta t_i = t_{\max} - t_i , \quad \text{Eq. (2.4)}$$

where t_{\max} is the maximum propagation time corresponding to the sensor element that is farthest from the focal point. Since the principle of focusing is reciprocal it also applies to collected data. To that end, the same time delays and coherent adding (stacking) of different sensor signals is applied, which procedure is referred to as *delay-and-sum beam forming*.

When a focus is created it will significantly increase the signal strength for objects in and near the focus, but it also increases the background noise level that is formed by both incoherent noise (ambient noise sources) and coherent noise (e.g. micro-scattering of the generated waves). The result is a non-uniform sensitivity and noise level in the reconstructed image, which complicates any image processing step that may be necessary to reach the desired quality level. To create a more uniform result involves varying the focus depth in steps and gathering consecutive data sets, which principle is depicted in Figure 2.5. In commercial medical imagers several focuses may be chosen at the cost of slowing down the achievable frame rate.

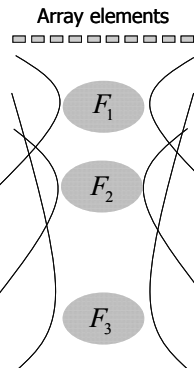


Figure 2.5. Multiple focuses produced during transmission.

2.2.2. Mid-end and back-end processing routines

The processing operations in imaging may be subdivided into three stages: *front-end processing*, related to the raw data acquisition and beam steering, *mid-end processing* and *back-end processing*. Mid-end processing applies to operations performed on the beam-formed data before an ultrasound image can be produced.

For example, for improving the SNR in an image one may subsequently apply filtering, detection, time gain compensation and compression methods. In back-end processing the operator may employ image processing to improve (in a subjective way) the quality and interpretability of details in the image. The main operations are briefly reviewed:

- A signal contains both amplitude and phase information, but for representation in gray-scale intensities the phase is discarded in favour of the envelope. The envelope is obtained as the absolute value of the analytical signals.
- Acoustic waves attenuate due to geometrical spreading as they travel in the propagation medium. A simple method, although non-physical in nature, is to use time-dependent gain compensation (TGC). Later arriving signals are amplified more strongly to correct for propagation attenuation and possibly also for material dependent acoustic losses.
- After TGC, the signals are compressed logarithmically to reduce the large dynamic range of ultrasound data. The idea is that small echoes carry as least as much relevant information as strong ones and compression puts them in the same dynamic range.
- A typical artefact that can obscure small details in ultrasound images is *speckle*. Speckle is due to wave scattering at small inhomogeneities, typically smaller than a wavelength. These generate constructive and destructive interference patterns that show up in the image as spots of low and high intensities, hence the name. Frequency compounding may be applied as a countermeasure. To that end, the original signal spectrum is split up in a number of sub-bands using narrow band-pass filters. The sub signals are then detected and compressed in the usual way. Since the SNR is different in each sub-band a spectral weighting function is used to level the SNR. The sub-band signals are then stacked to form the final image. The sub-bands contain phase-incoherent speckle patterns that average out by stacking. The frequency compounding procedure is shown in Figure 2.6.
- By combining images from different angles of the same object, one may also reduce speckle and improve both the contrast and SNR in the image. This is called *spatial compounding*. To this end one first takes multiple view images of the object, while taking note of the exact angle and translation of the sensor array in each case with respect to a common reference frame. Subsequently the images are transformed back to a reference position by applying linear 2D translation/rotation matrix operations. The final image is the (weighted) average of the transformed images.

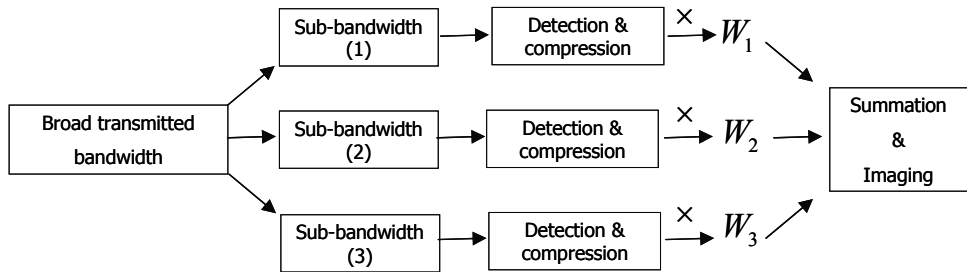


Figure 2.6. Frequency compounding: a broad spectrum is split up using narrow band filters to form sub-band signals. Stacking of the filtered signals suppresses the phase-incoherent speckle patterns. Some improvement may be obtained using weighting functions.

2.3. Real-time ultrasound experiments

2.3.1. Real-time ultrasound imager

Figure 2.7 shows the commercial medical imager device that is used for the monitoring and storing of images, which may then be analyzed for both static and moving particles in ferrofluid. The supplied probe has 128 elements with an aperture of 35 mm and was excited by pulses in the bandwidth of 3-10 MHz at the centre frequency of 5 MHz. The imager produces real-time ultrasound images and stores them either as separate images in BMP format or as a video stream in AVI format. The imager produces images at a maximum rate of 25 frames per second. It is noted that the frame rate is dependent on machine settings such as the viewing depth. For enhanced interpretation the video streams were imported into Matlab where they were converted back to separate images. As is obvious from Figure 2.7, the imager comes with a variety of functionalities, many of which are related to personalized image enhancing options. Those options are not of interest for this research as we intend to retrieve the ‘objective image’. However, some settings may be used to improve the image quality, for example selecting the dynamic range, without significant subjective interference with the image contents.



Figure 2.7. The portable commercial medical imager with matched probe.

2.3.2. Image quality from experimental ultrasound

The algorithms of the medical imager are designed for human tissue and handheld probe operation to obtain the best viewing angle. The MDS, as an industrial application, poses several challenges to the adaptation of this type of technology:

- The acoustic properties of human and animal tissue are close to that of water [Ludwig 1950], while plastics are generally more reflective and more attenuating.
- Maintaining image quality with limited, and only indirect, access to the probe. The probe should not be moved too much as it may disturb the laminar flow, while adjusting the viewing angle proves crucial for optimum image quality in medical applications.
- The possible influences of the magnetic field on the sensitivity of the piezoelectric sensors and the attenuating properties of the ferrofluid on image quality.

Figure 2.8 shows the experimental set-up for capturing ultrasound images of moving plastic particles inside a ferrofluid. Three typical particles of different shape and material from car shredder waste are attached to a thin string that is wrapped over two wooden rolls. The typical speed and motions of particles in the MDS is thus approximated by rotating the rolls from above the fluid with a string

(not shown). The particles were 10-20 mm long, 5-10 mm wide and 2 mm thick. The available observation range was a few mm to 120 mm from the probe.



Figure 2.8. Experimental set-up for simulation of moving particles in the black ferrofluid. Note that the wooden frame is partially taken out from the tank so that it would be visible in the photo.

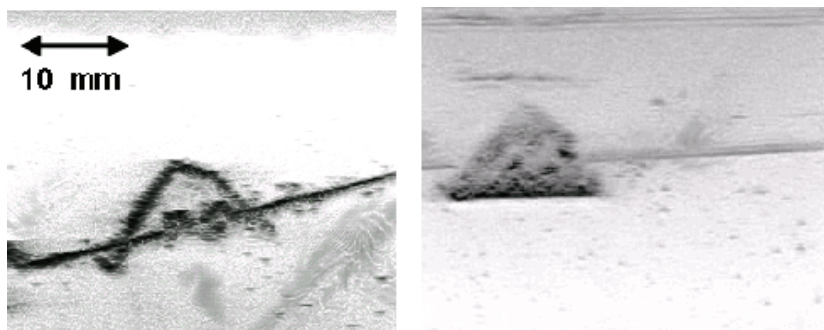


Figure 2.9. Ultrasound images of a plastic particle in ferrofluid. Left panel: static scene. Right panel: particle moving at 30 cm/s.

Figure 2.9 shows images captured from a movie sequence of a triangular plastic particle. The particle is observed in a static scene and while moving up to 30 cm/s. In both cases the shape of the particle is recognizable, clear, and relatively sharp, with smallest visible details of about 0.5 mm. The capability of the medical imager to detect small details from surface scattering in real-time is also clear from the thin string to which the particle was attached. It is noted that the viewing angle

of the probe was different for the moving particle. Other particles, also polypropylene and polyethylene, gave images of comparable quality.

The good shape consistency and sharpness of the ultrasound images is also demonstrated in Figure 2.10 that shows a M13 bolt and screw thread, which present easily identifiable shapes. The left panel shows the image when the whole underside of the bolt (no thread here) is irradiated from the left. Figures 2.9 and 2.10 could easily be mistaken for frontal views but are of course side views. Note therefore that the imaged surface must lie not only within the probe's observation window (xz -plane in Figure 2.3) but also within the few millimetres thick sheet formed by the deflected acoustic beam profile (yz -plane in Figure 2.3). The right panel in Figure 2.10 shows a cross section of the top of the bolt, also for irradiation from the left side. Here the long screw thread causes a shadow as it reflects the incident waves while also causing scattering at the threading, which in the reconstruction appears as a blur to the right side of the thread.

The 2D character of the ultrasound wave beam suggests that images of moving objects that are only partly inside the wave beam could be interpreted as cross-section views. From a number of these partial images the shape and perhaps even the volume of the complete object could be reconstructed using interpolation or morphing techniques [Kilian 2008]. The possibility is strongly suggested by the images in Figure 2.11 that shows three cross-section views of a polypropylene flat plate (2 mm thick) with two distinctive features ('the ears').

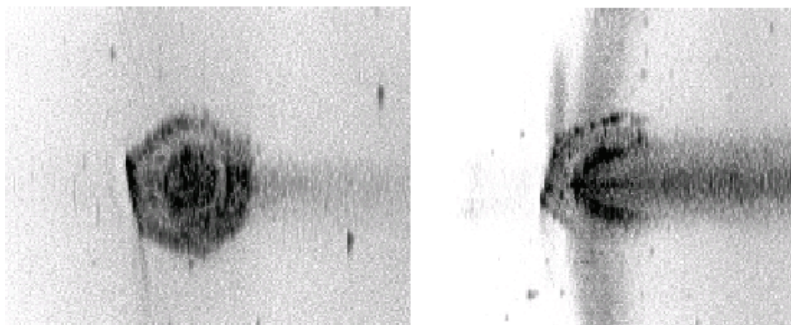


Figure 2.10. Metal screw thread with bolt, irradiated from the left side by ultrasound. Left panel: Bolt underside. Right panel: Bolt top and thread with a shadow and blurring effect.

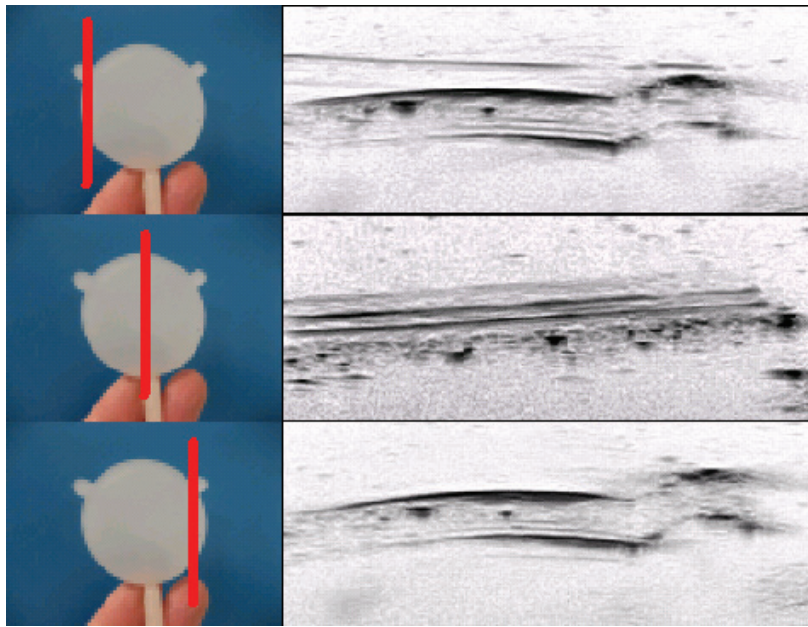


Figure 2.11. From top to bottom three ultrasound cross-section images of a plastic plate, shown on the left side. The thick lines in the photos indicate the plane in which the image was taken.

Two remarks are in order. First, since ultrasound waves will penetrate plastic material an image such as Figure 2.11 also shows also the back-wall of the plate. However, the medical imager does not recognize the difference in acoustic wave speed between water and plastic. Therefore the reconstructed thickness of the plastic plate will not be accurate. Second, the volume reconstruction is facilitated by the fact that most plastic waste particles are flakes and therefore flat (<3 mm thick). This makes them float in a predictable horizontal orientation in the MDS ferrofluid after the main density separation, i.e. just before they are removed from the fluid into the product. At the known flowing depth and preferred orientation, the particles can be observed from a favourable viewing angle by the ultrasound probe to minimize shadowing effects.

2.3.3. Data blending issues

Medical imaging technology necessitates a human operator to maintain or regain image quality. This is related to technology robustness, i.e. the ability to produce a good quality image under the varying conditions in which the probe has to function. One aspect relates to limitations of contemporary medical imaging hardware.

In a demonstrating test, three plastic plates according to the setup of Figure 6.2(a) (Section 6.2.1) were imaged using the medical imager in Figure 2.12(a). As

a demonstration of hardware limitation, an additional reflector (a flat glass plate) was placed at 50 mm depth and out of the set depth range of the imager. The figure gives a decent enough image of the three plates, but also artefacts may be observed, particularly the wavy horizontal lines at 15-20 mm depth. The likely cause is the fact that the water tank is large and water attenuates very little, which makes that long-travelling reflected waves can blend in with the imager data. Note therefore that to build a frame the medical imager fires a sensor group and then has to wait for data to come in from the chosen depth range before being able to fire the next sensor group. There were even blended waves reflected from the water surface which were easy to identify in the real-time images. Also, selecting a different depth range on the medical imager shifted the artefacts to a different depth. To prove this is the real cause, the same scene was tested using a manually scanned dataset and was processed by time-domain SAFT (cf. Section 4.4) to provide the image in Figure 2.12(b). Since the data acquisition took much longer to scan, this image is not affected by reflectors outside of the imaging depth range.

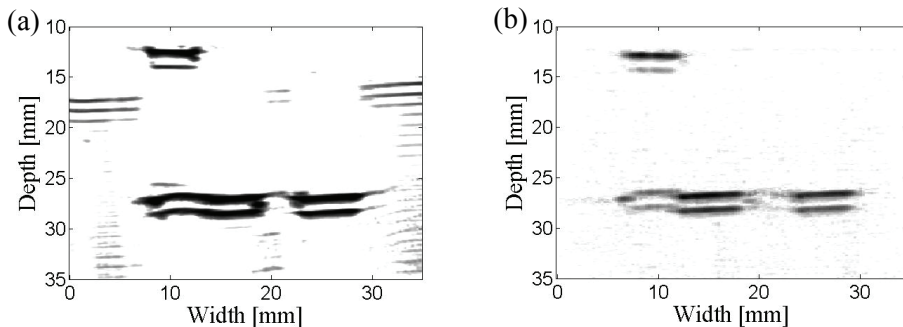


Figure 2.12. Setup with three plates and an added reflector out of depth range. (a) Medical imager result. (b) Same scene but using manually scanned data and SAFT.

Robustness against strong reflectors in low attenuating propagation media is important because these conditions are common in the MDS channel (e.g. ferrofluid, channel walls and splitters). Moreover, in an industrial setting it is undesirable to have an operator continuously on standby to restore image quality. This future ultrasound system design problem may in principle be solved by implementing a blended data acquisition strategy [Berkhout 2008]. This means firing sensors in a quick and randomized succession. It makes data acquisition much faster and avoids the reflection data blending, since the longer travelling waves will only arrive after the whole frame data has already been collected. Note that the time between two frames is easily a few milliseconds, which is too long for any reflected ultrasound wave to retain significant energy and be blended in with the next frame data. The challenge in a data blending strategy is to de-blend the

recorded data [Wapenaar 2012], so receiver responses may again be causally traced back to the transmitters.

2.4. MDS technologies and options for probe positioning

2.4.1. MDS technologies

In the MDS a suspension of water and ferrous nano-particles acts as the separating medium which flows inside a dynamically confined channel to allow for a large throughput of polyolefin particles, cf. Figure 2.13. By applying a strong magnetic field from the top, the ferrofluid effectively causes a gradient in mass density ranging from low at the top ($<850 \text{ kg m}^{-3}$) to practically the density of water at the bottom. Plastic particles are inserted at one end of the channel and will separate and finally reach a steady position at the depth where their mass density complies locally with the effective density of the fluid. From that point onwards the products can be extracted from the channel using splitters and pumps. The effective mass density of the ferrofluid and the exact equilibrium depth of plastic particles can be calculated by taking into account the forces applied by magnetic field and gravity on the fluid. This will be formulated in detail in Chapter 3. In Figure 2.13, the top conveyor removes floating materials and prevents them from sticking to the magnet. The bottom conveyor runs synchronous, to sustain the laminar flow, and removes the sink fraction from the channel.

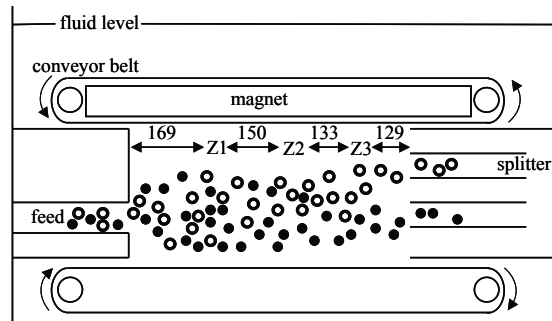


Figure 2.13. The immersed channel MDS as it separates two types of polyolefin particles into two streams. Measurements are performed at three different locations, marked as Z1, Z2 and Z3 (dimensions in mm but not depicted to scale: the channel from top belt to bottom belt is 103 mm deep).

This chapter presents the ultrasound data measured inside this type of separation channel for two different MDS versions.

1. **Open channel MDS:** This first trial version used a long, flat belt for the bottom conveyor which was forcefully shaped to form the rectangular cross section of the channel. The liquid was pumped in and out of the belt from the two open ends. This fluid flow design proved difficult to stabilize due to the open top, the strongly non-uniform cross section of the channel and the difficulties in controlling the flow in and out of the channel.
2. **Immersed channel MDS:** A fully functional prototype. The channel has a uniform cross section and the inlet and outlets of the fluid are completely immersed. Moreover, the fluid inlet and outlet parts are redesigned and produce very little turbulence.

2.4.2. Probe positioning

In the MDS the sensor array will be positioned permanently in the channel to gather images for monitoring control purposes or for quantitative measurement of particles streams or fluid flow characteristics. The relative position and viewing angle of the probe are of importance for maintaining image quality during the continuous MDS operations. To explore the options a theoretical study is made based on geometrical considerations. The optimum option follows by considering factors such as flow direction, available space for manoeuvring the probe and the beam profile produced by the sensor array. The options are characterised in terms of:

1. Particles monitoring capacity (particles per second)
2. Capacity rate (particles per image)
3. Redundancy (images per particle)

The following parameters are assumed:

- 35 mm probe aperture.
- 120 mm maximum scanning range, starting 5 mm from the probe.
- 25 images per second frame rate.
- 250 mm/s flow velocity of the ferrofluid
- Plastic particles have a circular shape, 11 mm in diameter and 2 mm thick.

Figure 2.14(a) gives an impression of the separation channel. The polypropylene (PP) and polyethylene (PE) particle streams are flowing out of the page. The relative depths of the splitters at the end of the channel are indicated. The most suitable probe positioning options are numbered 1 to 3, where the complementary positions are indicated as 'a' and 'b'. Figure 2.14(b) shows the interpretation of maximum particle stacking and particles view in the probe observation window for the three characterising parameters.

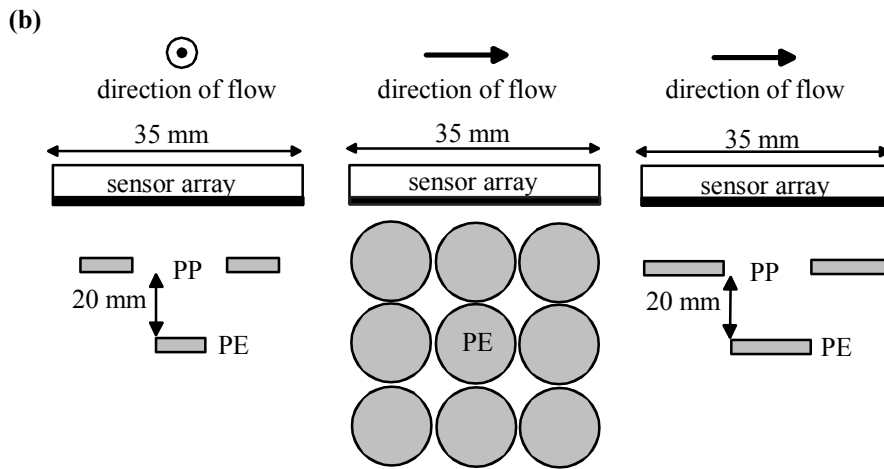
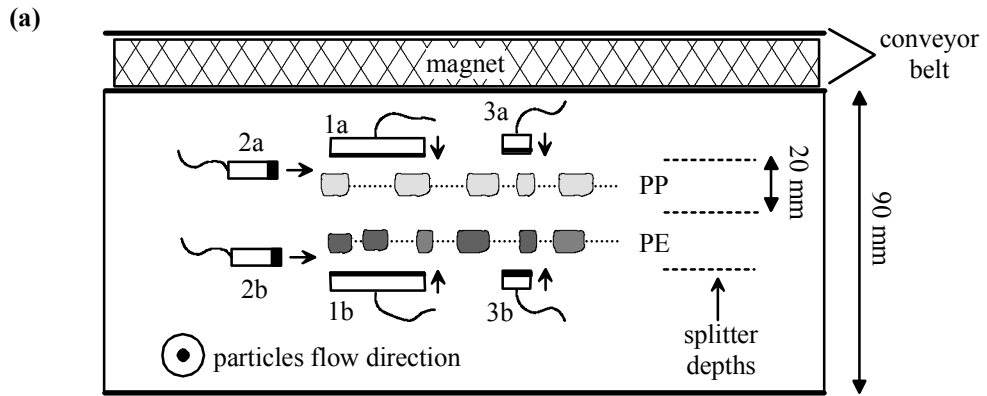


Figure 2.14. (a) Cross section view of the MDS channel with three possible array viewing positions and angles. (b) Interpretation of maximum monitoring view and capacity for moving round plastic particles in array positions indicated in (a). From left to right the panels correspond to array positions 1a, 2a and 3a.

The following assumptions apply for particles counting capacity:

- The particle streams of PP and PE float at unique depths
- Particles are perfectly ordered inside the viewing window with 1 mm spacing
- Only particles in full view of the observation window are counted.
- The ultrasound only sees the top particle (not the one hidden underneath)

- The number of particles over distance in a single row is limited to three, since particle edge scattering increasingly obscures the view on farther lying particles.

The characterising parameters for the different options are listed in Table 2.1.

Table 2.1. Particles statistics for different options for probe positioning.

Option	Viewing angle	Observed streams	Capacity rate (part./image)	Capacity (part./second)	Redundancy (images/part.)
1a/1b	Vertical	both	3	60	1
2a/2b	horizontal	top / bottom	9	60	3
3a/3b	Vertical	both	3	20	3

The a-positions are preferred from a practical point of view as they allow the probe cable to be led out of the MDS channel without crossing the particle streams. Positions 2 and 3 have a redundancy of three, meaning that a particle may be analysed on the basis of three independent images. Therefore, positions 2 and 3 appear good options if a high degree of accuracy (reliability) is needed. Besides, by tracking the particle in the three subsequent images, its speed may be measured. Position 1 appears best suited for depth detection or particle counting. Overall, position 2 seems the most attractive option in Table 2.1 as it also allows observing a maximum of nine particles at the same time. Note that in positions 1 and 3, the ultrasound beam penetrates inside the plastic particles and therefore provides a cross-section view of the particles which is linked to the particle thickness and volume. On the other hand, in position 2, the ultrasound waves are scattered at the surface of the particles which offers the chance to measure the particle surface area.

Two remarks are in order. First, Table 2.1 should be recalculated when the average particle size, the flow speed and/or the video frame rate is significantly different. Second, the imager takes intermittent snapshots (images), so particles will be missed if they move through the probe observation window faster than snapshots are taken. The proper interpretation in that case is that the imager effectively samples an MDS particles stream in time; i.e. the video only registers intermittent parts of a streamline of particles.

2.5. Quantitative analyses using real-time ultrasound

The medical imager generates the real-time images in a compact video format. These video streams are read into Matlab and split into separate images that are amenable for quantitative analysis on plastic waste particles. The main challenge is the development of suitable image processing procedures, i.e. a sequence of routines that can bring out the desired quantitative information. Therefore the objective here is not to build statistics, which would require massive data and

computational effort for analyses, but to demonstrate the principles by which a quantitative procedure may be developed. To this end, three fundamental procedures are developed and implemented in Matlab. The first calculates the particle density distribution (PDD) over the MDS channel depth. The second procedure tracks an individual particle so its particular motions may be studied. The Third procedure performs material detection of the plastic, based on ultrasound reflectivity as related to the relative pixel brightness in the images. Experiments were conducted in two versions of the MDS, as explained in Section 2.4.1. The corresponding experimental restrictions are:

- The open channel MDS provided a poor accessibility for the probe due to the magnet and conveyor belts. This restricted the possible options from Table 2.1 to option 1b (cf. Figure 2.14(a)).
- For the experiments using polyolefin materials in the immersed channel, the same restrictions for the probe accessibility apply as for the open channel version. The preferred probe position is 1b. However, due to the improvements made on the new MDS, the amount of air bubbles and foam is less, which improves the image quality.
- For the experiments using heavy plastics in the immersed channel MDS, the magnet was placed underneath the channel, making the MDS suitable for processing plastics heavier than water, e.g. PS, ABS or PVC. The advantage for ultrasound is that the whole length of the channel can be made accessible by replacing the top conveyor with a fixed PVC plate in which three holes are drilled in a line for probe access. Note that this replacement has the effect to increase the flow turbulence. The holes are at the inlet where the particles are inserted (Z1 in Figure 2.13), at the middle of the channel (Z2) and the last one close to the end of the channel (Z3) where the particles are extracted into the products. Therefore, the available options for the immersed MDS are options 1a and 3a (cf. Figure 2.14(a)).

A major drawback for obtaining image quality with both types of MDS was the foaming of the ferrofluid from the particles feed. In particular, for the experiments using heavy plastics in the immersed MDS the foam was heaviest, since under normal operations it would be continuously removed by the top conveyor which was temporarily removed to allow probe access to the channel. Foam was accumulating on the probe face and blocked the sensor view already within 15 to 20 seconds. The foaming was most severe near the inlet zone (Z1).

2.5.1. Image processing algorithms for PDD evaluation

One of the major objectives of the ultrasound system is to visualize the streams of particles floating in the separation channel. This should indicate the spatial positions of the particles in the channel depth. In principle, one should observe the accumulation of particles in different equilibrium depths as they travel further in

the channel to produce different product streams. Next to the particles positions in depth, other parameters such as number, volume or mass of particles processed by MDS could be used as quite useful quantitative information for evaluating the separation performance. For this purpose, particle density distribution (PDD) is measured from the real-time ultrasound images. Here, we introduce two processing routines which will be applied on the experimental data in the next sections.

The maximum intensity for each pixel (i,j) in the images of the video stream was determined to reveal the particles distribution over depth. Here, i and j represent the pixels in row and column respectively. The following procedure is repeated for all (i,j) pixels in the image:

$$\begin{aligned}
 I_0^{PDD}(i,j) &= 0 \\
 \text{for } n=1:N \\
 A_n(i,j) &= \begin{cases} 0, & I_n(i,j) \leq I^{NOISE}(i) \\ I_n(i,j), & I_n(i,j) > I^{NOISE}(i) \end{cases} \quad \text{Eq. (2.5)} \\
 I_n^{PDD}(i,j) &= \max(I_{n-1}^{PDD}(i,j), A_n(i,j)) \\
 \text{end} .
 \end{aligned}$$

Here, $I_n^{PDD}(i,j)$ is resulting particle distribution from the N images (I_n) in the video stream, and operator ‘max’ selects in a comparison the highest pixel intensity.

Due to the settings of the medical imager such as focus points or TGC, the signal-to-noise-ratio (SNR) would not be uniform everywhere in an image. In addition to the machine settings, the small air bubbles (foam) and dust particles carried by the flow could also affect the noise level in the image. This indicates that the SNR depends on the position of particles with respect to the probe. Therefore, for particle detection, the signal of the particles should be compared with the local noise level at the location where the particle has been observed. Obviously, a particle is detected only if the signal is higher than the noise. Note that due to the non-uniform SNR, some particles could have higher contrast than others. However, this does not influence the PDD analysis since the objective here is solely to detect or count particles and the level of contrast in the image is not relevant in this case. To detect particles, a non-linear background image noise level was determined. As it was shown by the measurements, the noise varied mostly in depth direction rather than in horizontal direction. Therefore, an image noise array denoted by $I^{NOISE}(i)$ was determined to act as a noise threshold, for which the maximum pixel intensity of the first few particle-free images was used.

The second procedure counts the number of pixels as a function of depth. For each row i , the number of pixels above noise level is counted for all other columns j , while this count is extended all the N images in the video. This procedure is expressed as:

$$I_0^{PDD}(i) = 0$$

for $n=1:N$

$$A_n(i, j) = \begin{cases} 0, & I_n(i, j) \leq I^{NOISE}(i) \\ 1, & I_n(i, j) > I^{NOISE}(i) \end{cases} \quad \text{Eq. (2.6)}$$

$$I_n^{PDD}(i) = I_{n-1}^{PDD}(i) + \sum_{j=1}^J A_n(i, j)$$

end.

2.5.2. Experiments in the MDS channel for PDD evaluation

Open channel MDS using polyolefin plastics

The particle density distribution (PDD) is determined for an open channel MDS using two batches of polyolefin plastics from WEEE. The first was high density polyethylene (HDPE) and the other polypropylene (PP). For calibration purposes the original batches were first pre-separated in specific density ranges using alcohol sink-float separation: PP in the range 900-910 kg m⁻³ and PE in the range 940-950 kg m⁻³. The polyolefin flakes had a length of 7-9 mm and were 3 mm thick. For both tests a few hundred particles proved sufficient to create some statistics. The fluid flow was maintained at a velocity of 100 mm/s. Note that in this experiment, the pure PP and PE batches were fed separately into the MDS channel. The probe was set up at the bottom as in option 1b in Figure 2.14(a). The resulting video stream was imported in Matlab and split into the PP and PE video streams. The procedure of Eq. (2.5) was implemented to create Figure 2.15 which shows the result as a function of increasing depth in the MDS channel (flipped orientation). It reveals an offset between the average flowing depth of the streams of PP (low density) and HDPE (high density). This validates the principle of the MDS, which separates polyolefin types despite their relatively small mass density differences. In addition, PDD was also determined based on Eq. (2.6) which resulted in Figure 2.16. It is observed that the particle distributions partly overlap, for which there are two likely explanations. Attached gas bubbles and light-weight pollutants such as grease cause particles to become lighter and float nearer to the upper surface of the ferrous liquid. Another possible cause is some turbulence in the flow, most likely caused by the rather poor inlet design of the open channel MDS. These are typical engineering issues to be improved in the MDS technology, but they were clearly identified using the ultrasound imaging technology. By using a graphical presentation like Figure 2.15 in a continuous industrial operation, an

operator may correct the splitter position for the optimum extraction of HDPE and PP products, which constitutes an online tuning capability. In the present case the optimum splitter position would be found around 40 mm depth.

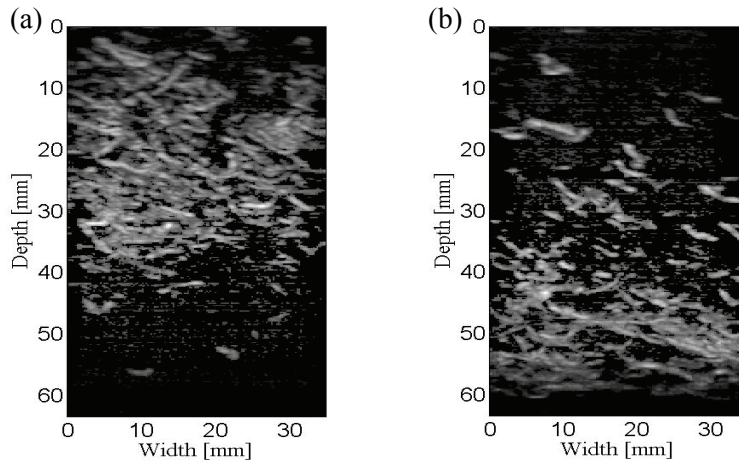


Figure 2.15. Particles density distribution with depth in the open channel MDS. (a) PP particles distribution. (b) HDPE particles distribution.

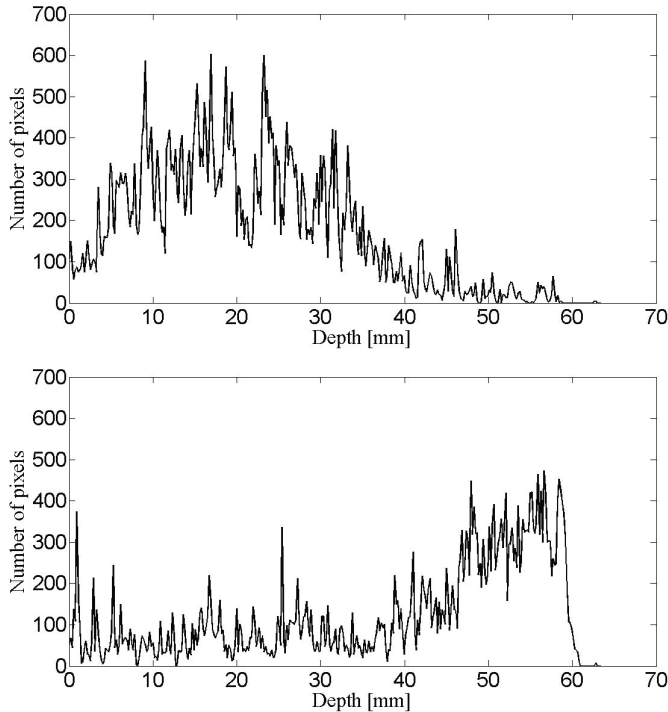


Figure 2.16. Particle density distribution as a function of depth of the open channel MDS. The ultrasound images were processed for PP stream (top panel), and for PE stream (bottom panel).

Immersed channel MDS using polyolefin plastics

In addition to the open channel MDS, the PDD is investigated for polyolefin materials but now using an immersed channel MDS of a pilot plant facility. The feeding materials were mixtures of PP and PE particles from the Romanian household waste. The probe was positioned at option 1b as shown in Figure 2.14(a). The fluid flow in the channel was kept at the speed of 200 mm/s which is two times faster than that of the open channel MDS. This makes the separation more challenging since it is more difficult to produce a laminar flow profile at higher speeds. A video-stream with time-duration of 25 [s] was imported in Matlab for further data processing. The PDD was calculated using Eq. (2.5) to give the image in left panel of Figure 2.17. The particles are observed everywhere in the depth range of 13 mm to 80 mm and it makes it difficult to distinguish the presence of the two separate streams. Note that this is a different scenario from Figure 2.15 because here the two products are fed together as a mixture in MDS and at the same time. Although the PDD has covered a wide range in Figure 2.17, it can be shown that the majority of particles floated at certain depths. Eq. (2.6) was used to

produce PDD as illustrated in right panel of Figure 2.17. In Figure 2.17, one may detect the two separate peaks representing to the two separate PP and PE product streams. Apparently, the amount of PP particles is more than PE particles due to the larger surface area under the curve for PP stream. Figure 2.17 suggests that, PP particles are distributed in depth range of 13-55 mm, and PE particles in range of 55-80 mm. This give an average depth of 35.6 mm and 63.4 mm for PP and PE streams respectively.

The probe position 1b gives a cross-section view of the floating particles (cf. Section 2.4.2). As an interpretation, the procedure of Eq. (2.6) gives an indication of the total particle cross-section area at each depth of all the observable particles in terms of detected pixels with intensity above the noise level. The total cross-section area can be translated into the total number of particles, volume and consequently total processed mass by MDS. For this analysis, the following assumptions are made:

- The average particle length, width and thickness are 4 mm, 4 mm and 2 mm respectively.
- A cross-section area of a single particle is 8 mm^2 which is corresponded to 128 pixels in the image.
- The imaging was performed at a rate of 18 frame/s. So, the time interval between the frames is 55.6 [ms].

For the PP stream, the total number of particles was 893 with a total mass of 26 g assuming a mass density of 900 kg m^{-3} . For PE stream, the total number of particles was 248 which gives a total processed mass of 7.5 g for a mass density of 940 kg m^{-3} . Note that a particle of an average length of 4 mm passes quickly through the thin ultrasound beam in a time period of 20 [ms]. This is almost 3 times shorter than the time-interval between the imaging frames, which means at least two in three particles were not detected by the imaging system.

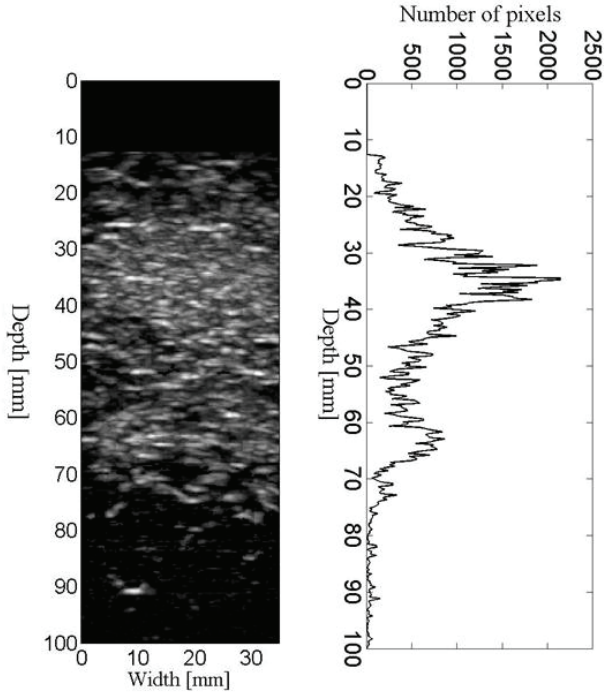


Figure 2.17. PDD with depth in the immersed channel MDS for polyolefin plastics. Left panel: PDD according to Eq. (2.5). Right panel: PDD according to Eq. (2.6).

Immersed channel MDS using heavy plastics

The PDD is determined for an immersed channel MDS using batches of plastics, heavier than water. The magnet was installed underneath the channel to create an effective mass density range of 1140 kg m^{-3} at the top to 1830 kg m^{-3} near the bottom of the channel. A batch of light PVC and rubber ($\sim 1150 \text{ kg m}^{-3}$) and a batch of heavy PVC ($\sim 1400 \text{ kg m}^{-3}$) from window frame waste were prepared. Before the tests the two different batches were first fully mixed and then manually fed to the MDS. The fluid flow was maintained at 180 mm/s. The probe option was 1a in Figure 2.14(a) and the scan positions used were Z2 and Z3, respectively. Figure 2.18 shows the depth distributions according to the counting procedure of Eq. (2.6).

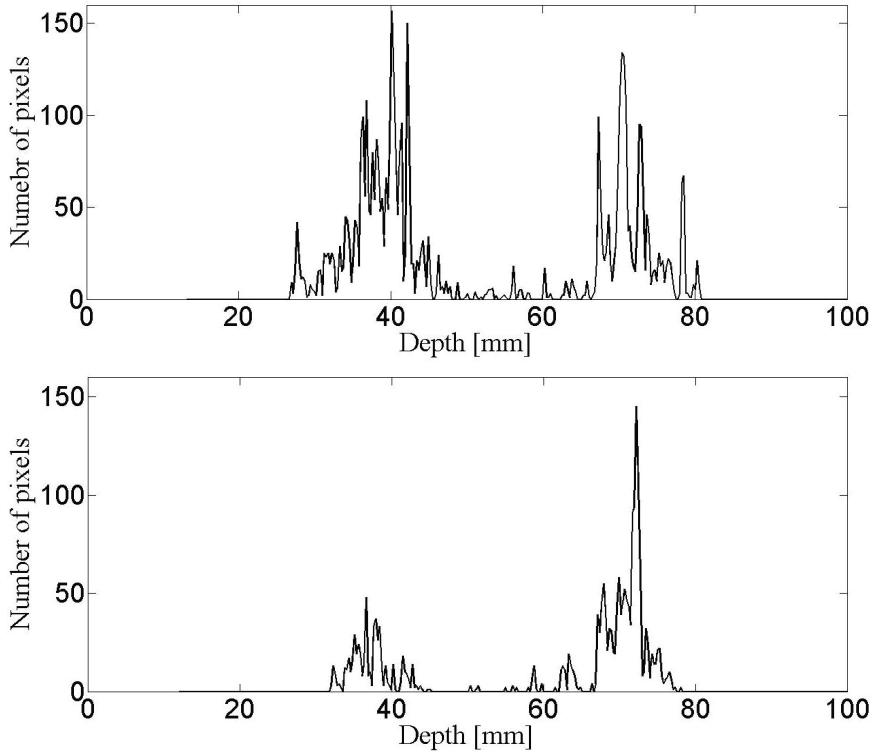


Figure 2.18. Particle density distribution as a function of depth of the immersed channel MDS. The ultrasound images were taken at position Z2, 319 mm from feed entrance (top panel), and at position Z3, 452 mm from the feed entrance and 129 mm from the extraction splitters (bottom panel).

The two product streams are well separated in Figure 2.18 in both the observation points, and obviously much improved compared to the open channel MDS in Fig. 2.15. The convergence of the streams of plastic over the 133 mm distance between Z2 and Z3 may be investigated by calculating the mean and standard deviation (STD) of the floating depth in Table 2.2. It proves the only significant change is the 38% decrease in STD from Z2 to Z3 for the light PVC, which indicates that light plastics need a longer time (longer distance) than heavier plastics to converge into a coherent stream. This may be explained by the larger effective ferrofluid density near the heavier plastic, which forces those particles more strongly into their equilibrium position, while the heavier material attenuates turbulence (e.g. fluid-particle or particle-particle interactions) more strongly. This implies that the MDS for heavy plastics separation may do with a shorter channel (and a cheaper MDS) than the one for light plastics.

Table 2.2. Particle depth statistics for light and heavy PVC at scan positions Z2 and Z3.

	Z2	Z3
Light PVC	mean: 38.4 mm STD: 4.4 mm	mean: 37.3 mm STD: 2.7 mm
Heavy PVC	mean: 71.8 mm STD: 3.4 mm	mean: 70.5 mm STD: 3.3 mm

2.5.3. Particle orientation, tracking and trajectory measurement

The PDD analysis discussed in Section 2.5.2 focused solely on distribution of the particles along the channel depth where quantitative information such as their number or mass could be extracted. Next to the depth position of a particle, its orientation in the flow at a certain depth could yield useful information on the flow profile. As an example, Figure 2.19 shows three imaging frames of particles for the experiment using immersed channel MDS and polyolefin plastics analyzed in Section 2.5.2. Note that the probe position was 1b and particles are imaged only at one frame. Under ideal conditions, a flat shaped particle moves in a laminar flow with its flat side oriented horizontally in the flow. This is indeed what is observed in Figure 2.19(a). It shows cross-section views of three 1 mm thick particles marked by a white circle. The particles are oriented horizontally in the flow. However, in Figure 2.19(b), although it still gives a cross-section view but the particle is deviated from the horizontal direction. In Figure 2.19(c), the particle is oriented almost parallel to the beam i.e. normal to the flow direction where the probe gives a surface view of the particle rather than a cross-section view as to be expected for the probe at position 1b. Another interpretation of the image in Figure 2.19(c) would be a cross-section view of a very large particle with 4mm thickness which is highly unlikely to happen. For the last two cases, the fact that the particles are not oriented horizontally in the flow is associated with the flow characteristic which would have been not ideally laminar. This is a useful feedback for the MDS operator since a laminar flow profile is expected especially at outlet zone (few centimetres before the splitters) where the probe was placed.

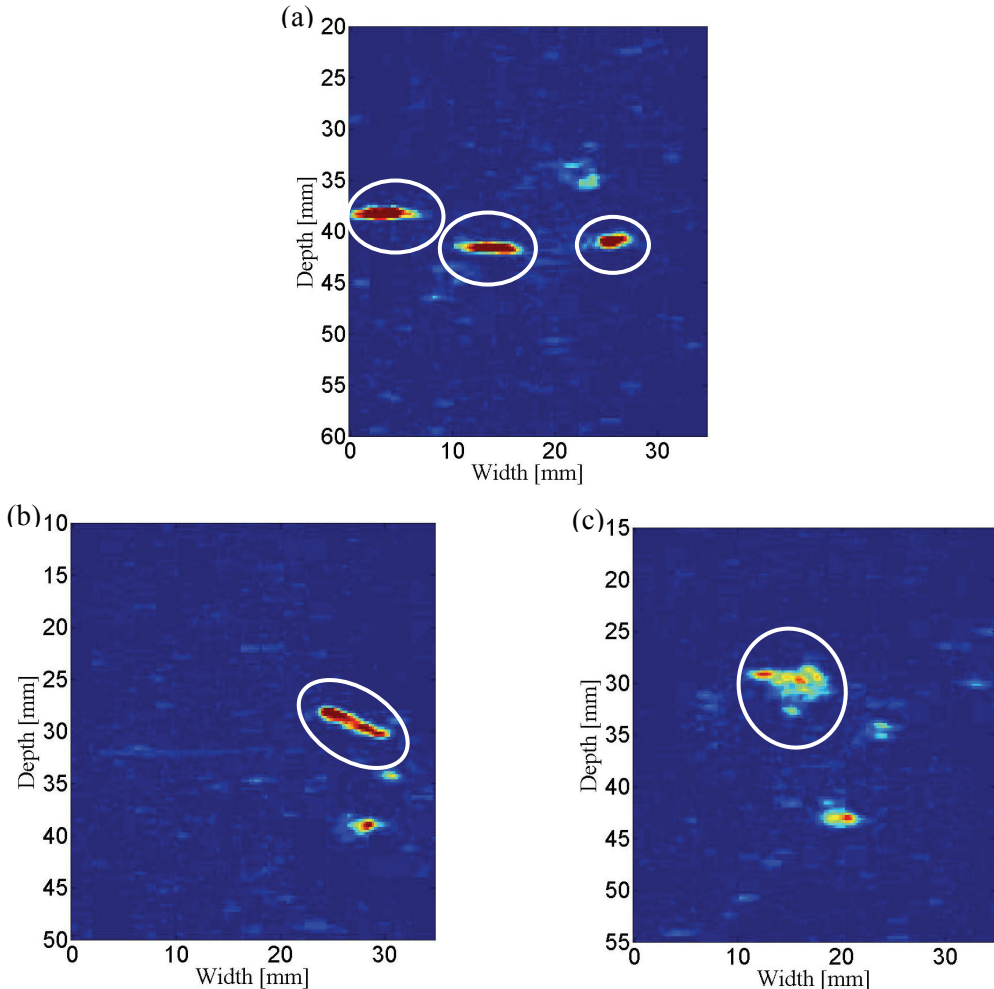


Figure 2.19. Imaging the orientation of particles in the MDS channel. (a) Three particles oriented horizontally. (b) An inclined particle. (c) A particle oriented normally with respect to the flow giving a surface view instead of a cross-section view.

The motions of individual particle should be tracked and visualized in detail in consecutive images to provide valuable data for experimental studies of intricate particles-fluid or particle-particle interactions in the MDS channel. Position 3a in Figure 2.14(a) serves this purpose quite well since its redundancy is three (Table 2.1), which means we may expect to catch the same particle completely in three images. However, a requirement for repeated detection in position 3a is that the target particle should flow exactly in-line within the few millimetres thin elevation beam produced by the probe (yz -plane in Figure 2.3), which reduces the chance of catching those particles. Since the usable time window

of observation was maximum 15 seconds at Z1 before foaming fully obscured the view, it was not possible to build on statistics and only several tens of particles were detected. However, most of them apparently moved horizontally through the fluid channel as they were caught in only one image, while only two particles could be caught in multiple images.

Figure 2.20(a) shows the maximum pixel intensities of a particle caught in five subsequent frames where the MDS was supposedly set to a flow speed of 180 mm/s. This measurement was taken at position Z1 and shows a light PVC particle of ~ 5 mm cross section moving from left to right and gradually moving upwards. The video was taken at a rate of 18 frames/s so the time interval between subsequent frames was 55.6 ms. Using the centre of the particle as a reference, the particle velocity in horizontal and vertical directions could be calculated as 148 mm/s and 15 mm/s, respectively. This gives a particle trajectory of 149 mm/s under an angle of 5.8° with respect to the assumed ideal horizontal trajectory.

Since the particle cannot move faster or slower than the flow speed in the horizontal direction, it must be concluded the flow speed is substantially lower at the particle depth. The relatively rising speed of the particle is substantial, since if it were to continue the whole length of the channel (581 mm), although unlikely, it would rise by some 59 mm. Note that Z1 is still close to the fluid inlet.

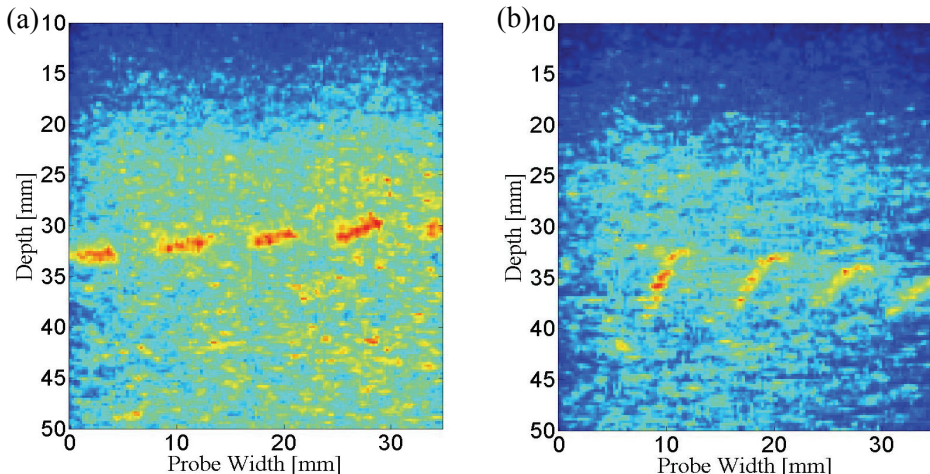


Figure 2.20. Tracking of individual particles in the MDS channel. (a) A rising particle detected at position Z1. (b) A rotating particle detected at position Z2.

Figure 2.20(b) shows the sequence for a curved, light PVC particle of ~ 10 mm cross section. Four images were used, taken from position Z2. The particle was moving from left to right and appears to be rotating forward to what could be equilibrium in a horizontal orientation. In that case, the noteworthy point is that the

particle appears to rotate around its lower left edge that remains at the same depth, which can only be explained if that edge has already reached equilibrium depth. In another interpretation it concerns a quite large and rather warped particle that moved sideways through the ultrasound beam and exposed in each image a different cross section of itself, while remaining at the same effective depth and, apparently, in a somewhat upright position. The latter interpretation seems rather less plausible, but shows that a 2D-type of view should be interpreted with care.

2.5.4. Materials identification

Different types of plastics exhibit different reflectivity to acoustic waves, which behaviour is attributed to the material acoustical impedance. For instance, PP has higher acoustic impedance than LDPE and therefore is a stronger reflector. The reflection amplitude corresponds to the pixel brightness in the imager video.

A basic experiment was conducted for two irregular-shaped particles of PP and LDPE. The array is scanned over the particles from the same distance. Figure 2.21 shows images of the two particles. It is just observable that the PP particle is a bit brighter than the LDPE particle, but using image processing this difference proves more convincing. The average pixel intensity for each particle was calculated using all available video images. A noise level was determined based on the first particle-free images. The pixel brightness ratio of PP to LDPE was 1.5, which confirms the stronger reflectivity of PP.

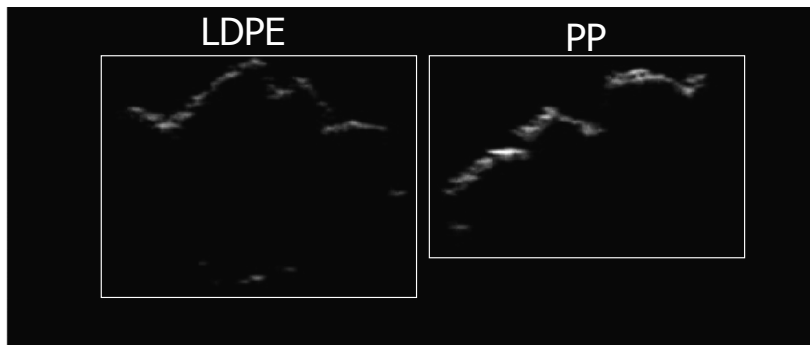


Figure 2.21. Difference in pixel brightness of irregular-shaped PP and LDPE particles.

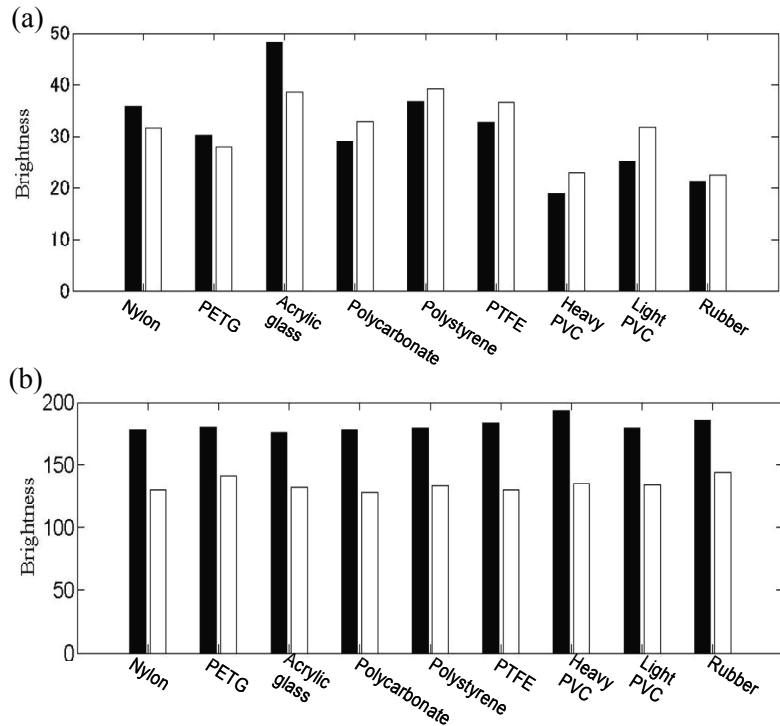


Figure 2.22. Difference in pixel brightness of different types of heavy plastics. Black and white vertical bars represent the 0-10 MHz and 0.3.5 MHz bands respectively. The vertical axis is the pixel brightness which runs from 0-255. (a) Reflectivity expressed as the average pixel brightness. (b) Reflectivity expressed as the maximum pixel brightness.

In the next experiment, a set of nine different types of heavy plastics were selected to test their reflectivity in the image. The materials included nylon, polyethylene terephthalate glycol (PETG), acrylic glass (also known as plexiglas), polycarbonate, polystyrene, Polytetrafluoroethylene (PTFE or commonly known as teflon), heavy density PVC, light density PVC and rubber. A number of 10-15 flakes were scanned by the probe for each plastic type. In computer, the pixel brightness values are stored as integers in the range of 0-255. Figure 2.22(a) shows the chart for average pixel brightness of the plastics. To investigate the effect of frequency range on reflectivity, the scan was performed in two different frequency bands: 0-10 MHz (black vertical bars) and 0-3.5 MHz (white vertical bars). For 0-10 MHz range, it suggests that the highest contrast in reflectivity is between acrylic glass and heavy PVC with a ratio of 2.5. The ratio is lower for other types of plastics. For 0-3.5 MHz range, the highest contrast is between polystyrene and rubber with a ratio of 1.7.

Next to the average pixel brightness, the maximum pixel brightness is also plotted in Figure 2.22 (b). It is clear that the difference in maximum brightness is not significant for different plastic types which is similar both frequency bands. Therefore, the average pixel brightness would be a better marker for material identification rather maximum brightness.

2.6. Evaluation of ultrasound imaging performance

Off-the-shelf, real-time medical imaging technology was studied to investigate the potential of ultrasound imaging for monitoring and quantitative analyses of the plastic particles in the MDS channel. The only required technical modification was to the sensor probe, which was fitted with a hydrodynamic casing to minimise flow disturbances. Tests were aimed at determining the quality, reproducibility and potential information contents of the images, which led to the following findings.

Potential of imaging technology

- Ultrasound technology is applicable under MDS processing conditions. The sensor array functions well in ferrofluid, and does not appear influenced in its sensitivity or achievable resolution by either the magnetic field or the ferrofluid nano-particles. The ferrofluid wave speed proved practically equal to that of water.
- Monitoring is a feasible application in MDS. Under the optimum viewing angle and probe positioning the images showed good shape consistency and sufficient detail (0.5-1 mm) for object surfaces in direct view of the array. Smaller objects were apparently also detectable, such as gas bubbles or specks of dust, since these were displayed at the minimum detail resolution by the commercial software.
- Quantitative analyses are feasible in MDS, because the images contain valuable information that is relevant for MDS processing and quality control. The ultrasound may be used for counting particles, for measuring the plastic particle density distribution (PDD), it allows tracking and calculation of the particle trajectories and it shows potential for plastic materials identification based on reflectivity. For example, the PDD may be used by an operator to optimize the MDS splitter positions for extracting quality products, which constitutes an online quality control capability, and the particles tracking allows the MDS flow to be assessed for optimization of the flow conditions. The requirement for each type of analysis is acceptable image quality, which strongly depends on the degree of foaming and dust particles in the ferrofluid and on the accessibility for an ultrasound probe in the narrow MDS channel.
- The statistics of the particle motions, as detected by ultrasound, are a direct measurement of the degree of turbulence in the channel, which is a major factor in separation accuracy. An operator is therefore able to use ultrasound to

determine optimal separation, or to see whether some external mechanism is causing excessive turbulence and so mal-separation.

Limitations of the commercial 2D medical imaging technology

- An operator is required to maintain image quality, since the optimum viewing angle is critical for image quality.
- The medical imaging is not robust to strong reflectors, such as metals (e.g. splitters) or plastics (channel walls) or the hard rubber of the conveyor belts. These cause disturbing artefacts to show up in the images. The cause of these artefacts is linked to the details in the imaging software and data acquisition strategy in the hardware which were not quite clear to the user. However, it is expected some artefacts are due to data blending. In medical imaging elements are fired consecutively to build an imaging frame, and data acquisition has to wait to receive the complete signals for a specific ROI before the next set of elements can be fired. This waiting time is long and yet short such that the reflections from the previous firing can still end up in the next acquisition as a blended measurement.
- The medical imaging software is of course matched to acoustic properties of tissues and not to plastic waste materials. Consequently, the physics of acoustic wave transmission in and out of reflecting plastic particles is not correctly accounted for. The corresponding acoustic information is therefore left unused and is suppressed at best, using smart processing to prevent them from causing imaging artefacts.
- The commercial medical imager presents a black box; its software and hardware are dedicated for the medical market, copy-right protected and not accessible for our research purposes.

Based on these findings an investigation is warranted into the possibilities of enhanced ultrasound imaging and quantitative analysis for MDS. For example, the physics of acoustic wave transmission in and out of reflecting plastic particles should be studied for its potential quantitative information. Part of this study are optimum data acquisition strategies and imaging techniques that may improve image quality and eliminate the need for sustained human intervention under industrial MDS conditions. In particular, further study should take account of the need for online applicability, i.e. real-time potential and least computational effort.

References

[Berkhout 2008] A. J. Berkhout. Changing the mindset in seismic data acquisition, *The Leading Edge*, 27, pp. 924-938, 2008.

[Carson 1977] Paul L. Carson, Thomas V. Oughton, William R. Hendee and Avtar S. Ahuja. Imaging soft tissues through bone with ultrasound transmission

tomography by reconstruction, *Medical Physics*, Vol. 4, No. 4, pp. 302-309, Jul./Aug. 1977.

[Szabo 2004] T. L. Szabo, Diagnostic Ultrasound Imaging: Inside Out. Elsevier 2004.

[Ludwig 1950] G. D. Ludwig, The velocity of sound through tissues and the acoustic impedance of tissues, *JASA*, vol. 22, no. 6, pp. 862-866, May 2004.

[Kilian 2008] P. Kilian, New visualization tools: computer vision and ultrasound for MIS navigation. *Int. J. Med. Robotics. Comput. Assist. Surg.*, vol. 4, pp. 23-31, January 2008.

[Wapenaar 2012] Kees Wapenaar, Joost van der Neut and Jan Thorbecke. Deblending by direct inversion, *Geophysics*, Vol. 77, No. 3, pp. A9-A12, May-June 2012.

Chapter 3: Linear acoustic theory for ferrofluids and plastics

3.1. Introduction

The acoustic equations form the basis for different technologies based on acoustic wave fields. In particular, the ultrasound imaging technique is aimed at visualizing and measuring properties of plastic waste particles suspended in a ferrofluid. The equations describe wave fields in terms of state variables in space and time, representing the acoustic pressure and acoustic particle velocity. To appreciate the possible information contained in a scanned acoustic dataset it is essential to first develop a fundamental understanding of the physics behind the collected data signals. Combined with experimental insights and a tactical measurement strategy it allows one to extract information which is not readily apparent from visual inspection of, for example, a plotted B-scan. Moreover, a fundamental understanding of the physics offers possibilities for developing new measurement techniques.

In wet waste processing the 5-15 mm sized plastic waste particles are fully immersed in a liquid (usually water), by which information can be carried solely by compression waves. Plastic is a solid matter which sustains both compressional and shear wave modes. As measurements will show, shear modes in the small plastic particle may contribute signals to the acoustic data, but these are less strong and carry less useful information for imaging than compressional modes. In particular, signals carried by multi-mode converted waves are quite weak in comparison and their role may be neglected. This allows introduction of a modelling approach in which the multi-mode nature of small plastic particles is neglected and elastic wave propagation may be approximated using the equations for liquids.

In a wet separation technique such as MDS the ferrofluid is close to an ideal fluid such as water. Therefore the viscosity may be neglected in the liquid in which the plastic particles are immersed. However, inside the plastics the waves may attenuate more strongly due to different mechanisms that are effectively modelled using a linear relaxation function. Plastic waste is shredded to the smaller sized particles that are suitable for MDS processing and therefore the particles are commonly quite homogeneous and isotropic. A small complication with some softer plastics is that cutting and ripping actions during shredding may cause strain hardening at the edges of the particle, which may cause a degree of anisotropy. This small complication will be ignored in the acoustic equations.

Sensor arrays produce levels of acoustic pressure and displacement which are far below the threshold where acoustical material properties would start to vary or where surfaces would start to deform relative to a few wavelengths. In other words, the wave fields may be described using the linearized equations, since quantities such as mass density and compressibility are accurately approximated by constants.

First the linearized equations of motion and the constitutive equation for the ferrofluid are constructed. From these the acoustic wave equation for the ferrofluid is derived. Basic solutions for the static pressure fields generated by body forces are analysed to explain the physical principle behind MDS. Subsequently, basic solutions to the dynamic wave equation are analysed both in the space-time domain and in the wavenumber-frequency domain. Finally, the different types of polyolefin waste plastics are experimentally characterized.

3.2. Equations of motion

The state variables of the linearized acoustic wave field are the pressure P [Pa] and the particle velocity vector \mathbf{V} [m/s]. Consider the deformation and motions of an infinitesimal volume $V^e = \Delta x \Delta y \Delta z$ of magnetized ferrofluid in a Cartesian coordinate system, as shown in Figure 3.1. Newton's second law states that the inertial forces oppose the exerted force:

$$\mathbf{F} = \rho \frac{\partial \mathbf{V}}{\partial t} V^e. \quad \text{Eq. (3.1)}$$

Here \mathbf{V} represents the average velocity vector inside the infinitesimal volume. The net force vector is the sum of different forces. The first are gradients in the pressure which cause forces on the faces of the cubic element. For example, examine the pressures at the opposite faces A and B in Figure 3.1. Since the element is infinitesimal the pressure at face B may be obtained by first order Taylor expansion from the pressure at face A . The force component in the x -direction is:

$$F_x = P \Delta y \Delta z - (P + \frac{\partial P}{\partial x} \Delta x) \Delta y \Delta z = -\frac{\partial P}{\partial x} \Delta x \Delta y \Delta z. \quad \text{Eq. (3.2)}$$

Similarly, it is straightforward to apply the same procedure to the faces perpendicular to the other axes and show that those force components are:

$$F_y = -\frac{\partial P}{\partial y} \Delta x \Delta y \Delta z, \quad F_z = -\frac{\partial P}{\partial z} \Delta x \Delta y \Delta z. \quad \text{Eq. (3.3)}$$

In total, the force on the element due to pressure is given by the vector:

$$\mathbf{F}^{\text{pressure}} = -V^e \nabla P. \quad \text{Eq. (3.4)}$$

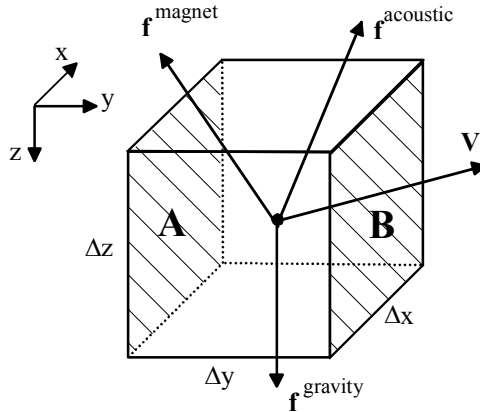


Figure 3.1. Cubic infinitesimal element with volume V^e . Indicated with respect to the cube centre are the average velocity vector V and three body forces.

In addition, as shown in Figure 3.1, three externally imposed body forces may act on the element. These are caused by gravity, a magnetic field and acoustic sensors. In an acoustic sensor, a high voltage is applied to the piezoelectric crystals which make them oscillate at very high frequencies (2-7 MHz). These oscillations are then propagated as acoustic pressure waves and will exert a force $\mathbf{f}(t)$ on the fluid. Combining all contributions to the net force in Eq. (3.1) yields:

$$\mathbf{F} = -V^e \nabla P + V^e \mathbf{f}^{bf}. \quad \text{Eq. (3.5)}$$

The body forces in Eq. (3.5) are specified as

$$\mathbf{f}^{bf} = g \rho \mathbf{e}_z + \nabla \mathbf{M} \cdot \mathbf{B} + \mathbf{f}(t). \quad \text{Eq. (3.6)}$$

Here, $g=9.81 \text{ m/s}^2$ and \mathbf{e} denotes a unit vector. The magnetic body force in Eq. (3.6) is determined by the gradient in the cross-magnetic energy, which is caused by the magnetization vector \mathbf{M} of the ferrofluid and the magnetic flux density \mathbf{B} generated by a system of magnets.

3.3. Constitutive equation

Eq. (3.1) yields three equations while there are four state variables. To arrive at a complete set of equations the pressure must be related to the velocity in a way that is specific for the fluid at hand. This type of relationship is called a *constitutive equation*. Based on the Hooke's law for fluids one may write as

$$P = -K \frac{\Delta V^e}{V^e}. \quad \text{Eq. (3.7)}$$

Here K denotes the *bulk modulus* of the fluid, which is the resistance of the medium to uniform compression. The modulus is the inverse of the more familiar compressibility κ used in acoustics. Note that the minus sign in Eq. (3.7) expresses that a decrease in volume will increase the pressure and vice-versa. To specify the volume change in terms of the state variables the displacements at the faces of the elementary cube are required. By denoting the displacement vector as $\xi = (\xi_x, \xi_y, \xi_z)$ the changes in volume of the cube are:

$$\begin{aligned} \Delta V^e = -V^e &+ [\Delta x + \xi_x(x + 0.5\Delta x) - \xi_x(x - 0.5\Delta x)] \times \\ &[\Delta y + \xi_y(y + 0.5\Delta y) - \xi_y(y - 0.5\Delta y)] \times \\ &[\Delta z + \xi_z(z + 0.5\Delta z) - \xi_z(z - 0.5\Delta z)] \end{aligned} \quad \text{Eq. (3.8)}$$

With some basic algebraic manipulation and taking limits for infinitesimal displacements, these equations may be written in the continuous differentiable form:

$$\Delta V^e = -V^e + V^e \left(1 + \frac{\partial \xi_x}{\partial x}\right) \left(1 + \frac{\partial \xi_y}{\partial y}\right) \left(1 + \frac{\partial \xi_z}{\partial z}\right). \quad \text{Eq. (3.9)}$$

By retaining the first order terms and substituting in Eq. (3.7), it is recognised that the constitutive equation may be specified as

$$P = -K \nabla \cdot \xi. \quad \text{Eq. (3.10)}$$

By applying a time differentiation to both sides of Eq. (3.10) the switch is made to velocity and we arrive at the desired form of the constitutive equation:

$$\frac{\partial P}{\partial t} = -K \nabla \cdot \mathbf{V}. \quad \text{Eq. (3.11)}$$

Eq. (3.11) may be generalized for later purposes by addition of a type of source called a *volume rate injection source*, denoted as Q [1/s]. This source is analogue in effect to the divergence of the displacements

$$\frac{\partial P}{\partial t} = -K \nabla \cdot \mathbf{V} + K Q. \quad \text{Eq. (3.12)}$$

3.4. The wave equation

The basic set of linear acoustic equations is determined as

$$\frac{\partial P}{\partial t} + K \nabla \cdot \mathbf{V} = K Q , \quad \text{Eq. (3.13)}$$

$$\nabla P + \rho \frac{\partial \mathbf{V}}{\partial t} = \mathbf{f}^{bf} . \quad \text{Eq. (3.14)}$$

When applying temporal and spatial differentiation operators to these equations, the second order wave equations may be obtained with the help of some basic algebraic manipulation. Assuming that K and ρ are space-independent:

$$\begin{aligned} \frac{\partial^2 P}{\partial t^2} - c^2 \nabla^2 P &= K \frac{\partial Q}{\partial t} - c^2 \nabla \cdot \mathbf{f}^{bf} , \\ \frac{\partial^2 \mathbf{V}}{\partial t^2} - c^2 \nabla^2 \mathbf{V} &= -c^2 \nabla Q + \frac{1}{\rho} \frac{\partial \mathbf{f}^{bf}}{\partial t} . \end{aligned} \quad \text{Eq. (3.15)}$$

Here the wave propagation velocity is introduced as:

$$c = \sqrt{K / \rho} . \quad \text{Eq. (3.16)}$$

It is noted that to arrive at the wave equation for the particle velocity, use has been made of the vector identity and the fact that a compression field is not rotational [Aki 2002]. The magnetic and gravity body forces are both time-independent and only give static contributions to the pressure. This allows their contribution to be taken into account separately from the solution for acoustic sources $\mathbf{f}(t)$. Moreover, since acoustic sensors are only sensitive at high frequencies the static sources of pressure go unnoticed in an acoustic experiment. It may be observed that there are two choices for the acoustic source: the body force and the volume injection rate. Later in Chapter 4 it is shown that both perform a separate role in the derivation of inversion and imaging algorithms. As a physical source, the body force is usually selected to represent the action of an ultrasound piezoelectric transmitter. In a mathematically related approach the transmitter may also be modelled by introducing the acoustic source in a boundary condition, by which the wave equation may be source-free in the propagation medium.

3.5. Static pressure distributions and the MDS principle

The sum of components of the static body forces in Eq. (3.6) is specified as

$$f_x = f_x^{mg}, \quad f_y = f_y^{mg}, \quad f_z = g\rho + f_z^{mg}. \quad \text{Eq. (3.17)}$$

By direct integration (taking the primitive) of Eq. (3.14) the pressure may be solved as

$$P(x, y, z) = g\rho(z - z_0) + \int_{x_0}^x f_x^{mg}(x')dx' + \int_{y_0}^y f_y^{mg}(y')dy' + \int_{z_0}^z f_z^{mg}(z')dz'. \quad \text{Eq. (3.18)}$$

The origins x_0 , y_0 and z_0 in the integral boundaries may be selected at arbitrary positions in the MDS channel.

The ferrofluid is composed of nano-sized ferrous particles suspended in a solute to which a surfactant has been added to prevent their agglomeration. In a stable ferrofluid the nanoparticles are therefore free to move individually under influence of Brownian motions. The solute may be oil or water, where the latter is preferred for a waste processing application. When subjected to a magnetic field the particles within a given small volume behave on average as a paramagnetic medium. Note that the applied magnetic field does not result in a flow of particles or in particles agglomerations at the magnet, since the Brownian motions are dominant. The magnetic force defined in Eq. (3.6) depends on the effective magnetization \mathbf{M} of the ferrofluid, which is proportional to the magnetic field strength \mathbf{H} using the magnetic susceptibility:

$$\mathbf{M} = \chi \mathbf{H}. \quad \text{Eq. (3.19)}$$

The susceptibility depends on the type and average amount of polarized nanoparticles per unit of volume solute and therefore varies with particles concentration. In a typical polyolefin MDS application the water-based ferrofluid is quite diluted with perhaps half a volume percent nanoparticles, which add only a few mass percent to the density of water. Still, for a fixed concentration the susceptibility is not constant as the particles will saturate with increasing magnetic field strength. In a typical MDS application the ferrofluid saturates perhaps at a magnetic flux density of 0.05 T. On the other hand, a saturated magnetic medium makes it easier to calculate the resulting magnetic force.

The principle of MDS may be demonstrated using a few simplifying conditions. Let's assume that a specially designed magnet system is suspended at the top surface $z=0$ of the ferrofluid, where z increases with depth into the fluid. The magnet system predominantly produces a vertically orientated magnetic field in the fluid, which saturates the nanoparticles at each relevant depth. A unit-

magnetisation vector with amplitude m_0 is assumed, which will align to the direction of the applied magnetic flux and is expressed as:

$$\mathbf{M} = m_0 \frac{\mathbf{B}}{\|\mathbf{B}\|}. \quad \text{Eq. (3.20)}$$

A simple divergence-free magnetic flux density field is given as

$$\begin{aligned} B_x &= b_0 \exp(-2\pi z/\lambda) \cos(2\pi x/\lambda), \\ B_y &= 0, \quad B_z = -b_0 \exp(-2\pi z/\lambda) \sin(2\pi x/\lambda), \quad z > 0, \end{aligned} \quad \text{Eq. (3.21)}$$

where, λ is a spatial wavelength of a Halbach array [Moon 2004]. Here, the objective is to find the equilibrium depth of a flat plastic particle (flake) and the effective mass density of the ferrofluid itself as a function of depth. The vertical component of the magnetic force is evaluated first:

$$f_z^{mg}(z) = -(2\pi/\lambda)m_0 b_0 \exp(-2\pi z/\lambda). \quad \text{Eq. (3.22)}$$

Note that the vertical force component is directed towards the magnet system, as it should. The assumed plastic particle is a square flake with surface A , thickness d and a mass density ρ^f lighter than water. Note that a flake will only suspend stably in a flat, horizontal orientation. Obviously, the size of the flake has no bearing on the equilibrium depth. Using the vertical component in Eq. (3.22) the equilibrium depth z is determined using Archimedes' law of displaced mass:

$$\begin{aligned} \rho^f g d &= \int_z^{z+d} \left(\rho g + f_z^{mg}(z') \right) dz' \\ &= \rho g d - m_0 b_0 \exp(-2\pi z/\lambda) (1 - \exp(-2\pi d/\lambda)), \end{aligned} \quad \text{Eq. (3.23)}$$

where ρ is the density of the ferrofluid without the presence of a magnetic field. The equilibrium depth as function of flake thickness and mass density is found as

$$z^{eq}(\rho^f, d) = \frac{\lambda}{2\pi} \ln \left(\frac{m_0 b_0 (1 - \exp(-2\pi d/\lambda))}{gd(\rho - \rho^f)} \right). \quad \text{Eq. (3.24)}$$

The effective mass density of the ferrofluid itself may also easily be found by dividing both sides of Eq. (3.23) by d and taking the limit of d to zero:

$$\rho^f = \rho - \frac{2\pi m_0 b_0}{g\lambda} \exp(-2\pi z/\lambda). \quad \text{Eq. (3.25)}$$

A few remarks are in order. First, in case the magnetization and the applied flux density are both quite strong the effective mass density in Eq. (3.25) can become negative close to the magnet. This means the pull of the magnetic force becomes stronger than gravity and the ferrofluid would exhibit an inverse effective mass density, i.e. an object released at the depth of zero effective density may move either up or down to reach equilibrium. For example, for $B=1$ T and using water density the effective density at the magnet becomes negative for $m_0=10000$ A/m. This magnetization is quite high for the ferrofluid used in polyolefin MDS, but may be reached in the laboratory using stronger nanoparticles concentrations and/or stronger magnetic fields. Second, for a general particle shape Eq. (3.23) must be replaced by an integral running over the particle surface. Third, in case the MDS deals with plastic particles heavier than water the magnetic configuration is exactly reversed, which means the magnet system is placed underneath the ferrofluid and the magnetic field effectively enhances the gravity force. This case may be analysed analogous.

3.6. Solutions to the wave equation

3.6.1. Plane waves

The physics of wave propagation may be understood better by studying generic solutions to the wave equation. The most basic are those for the homogeneous acoustic wave equation:

$$\frac{\partial^2 P}{\partial t^2} - c^2 \nabla^2 P = 0. \quad \text{Eq. (3.26)}$$

A solution is a time harmonic wave oscillating with period T , radial frequency $\omega=2\pi/T$ and spatial wavelength $\lambda=cT$. A wave is called plane if its phase is constant in each plane parallel to the wavefront. Using the observation coordinate vector \mathbf{x} , the functional form for such a wave is:

$$P(\mathbf{x}, t) = A \exp\left(i\omega t \mp i\mathbf{k} \cdot \mathbf{x}\right). \quad \text{Eq. (3.27)}$$

Here A is the complex amplitude and \mathbf{k} is the wave-vector, of which the components determine the direction of propagation in space with respect to a given coordinate system. The two types of solution, indicated by the minus/plus sign, indicate waves propagating in positive and negative directions with respect to the coordinate axes, respectively. This may be understood by regarding the propagation of a constant phase while keeping in mind that time is a positive and monotonically increasing parameter. Thus it may be found that a given phase can only be maintained, i.e. propagated, in either the positive or negative direction.

Functions given by Eq. (3.27) solve the wave equation under conditions to the wavenumbers. This may be determined after substitution of Eq. (3.27) into Eq. (3.26):

$$\left(\|\mathbf{k}\|^2 - (\omega/c)^2 \right) P(\mathbf{x}) = 0. \quad \text{Eq. (3.28)}$$

The bracketed term is called the *dispersion relation* and shows that frequency and wavenumber are connected. If the velocity and frequency are constants and it is noted that the absolute spatial direction is merely a convention of coordinate system, it is easy to show that the wavenumbers comply with

$$\|\mathbf{k}\| = k_0 = 2\pi/\lambda, \quad c = \omega/k_0. \quad \text{Eq. (3.29)}$$

The plane wave solutions in Eq. (3.27) are fundamental since they form an orthogonal, complete set. This means that any wavefield may be uniquely expanded in terms of these types of functions, which lies at the heart of the Fourier transformation. For an arbitrary wavefield this may be expressed using two-sided infinite integrals

$$P(\mathbf{x}, t) = \frac{1}{(2\pi)^2} \iint P(\mathbf{k}, \omega) \exp(i\omega t - i\mathbf{k} \cdot \mathbf{x}) d\mathbf{k} d\omega. \quad \text{Eq. (3.30)}$$

The complex amplitudes in the kernel may be obtained using the forward version of the Fourier integrals.

Figure 3.2 shows a snapshot of the pressure intensity of a plane wave in the observation plane $z=0$, which is at an angle to the wavefront. It is clear that the wave propagates either under $\varphi=45^\circ$ or $\varphi=-135^\circ$ with respect to the x -axis. However, the exact direction cannot be determined without looking at another snapshot taken a bit later; noting that every T seconds later the pressure pattern will be the same. In other words, if the wavefront cannot be observed then time information is required to determine the direction of wave propagation. The direction of the wave can also be determined by aligning a row of small sensors less than halve a wavelength λ apart, i.e. a linear sensor array, and logging their data (cf. Figure 3.2). By determining the phase evolution from sensor to sensor and measuring the projected wavelength across the sensors the direction of propagation can be determined. For example, if in Figure 3.2 the projected wavelength is λ_x , the wave would propagate under an angle determined by

$$\cos(\varphi) = \lambda/\lambda_x. \quad \text{Eq. (3.31)}$$

Note that the physical wavelength is assumed known through a-priori knowledge of the wave velocity while the related wave period T is preserved in the time signal

of each sensor. In addition, let's assume that the measured phase increases from the top sensor to the bottom sensor, which means that the phase increases in x -direction. In that case the propagation direction may be determined from Eq. (3.28) in the range $-90^\circ < \varphi < 90^\circ$. This implies that a second sensor array rotated with respect to the first is required to uniquely determine the direction of a plane wave. However, this situation is rare in practice and, moreover, piezoelectric sensors have a directional sensitivity by which the effective range in Figure 3.2 may be limited to $0 < \varphi < 90^\circ$.

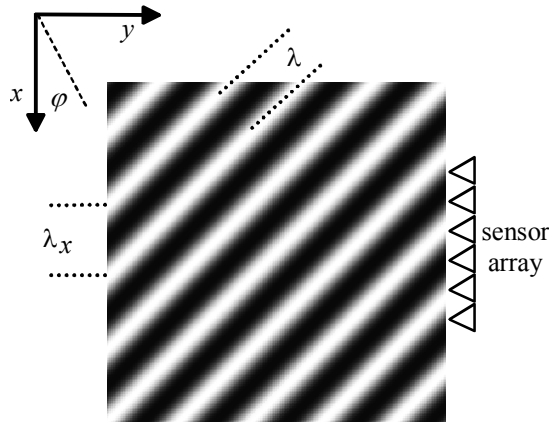


Figure 3.2. Intensity plot of a plane pressure wave. Physical and projected wavelengths are indicated. The linear sensor array allows detection of the direction of propagation.

Knowing the original directions of a number of detected waves offers the possibility to determine the origin of those waves by applying a procedure analogue to wave triangulation. This ability, offered by the sensor array data, is fundamental to the imaging techniques developed in Chapter 4.

3.6.2. Green function

Another generic type of solution besides the plane wave is the one for the inhomogeneous wave equation using a Dirac delta as a source, which is written using the traditional symbol G :

$$\frac{\partial^2 G}{\partial t^2} - c^2 \nabla^2 G = -p_0 \delta(t) \delta(\mathbf{x}). \quad \text{Eq. (3.32)}$$

A constant power p_0 [W] compensates for the physical unit so G represents pressure. The delta functions, which are distribution functions in the mathematical sense, may be thought of as describing an ideal point source which initiates waves

in an infinitely short pulse. This pulse introduces a constant frequency spectrum by which the function G , called *Green function*, is not band-limited. This property makes it difficult to accurately solve for the complete Green function using only numerical methods. The solution of Eq. (3.32) is extensively analyzed in literature [De Hoop 1995] and is reproduced here without details

$$G(\mathbf{x}, t) = -p_0 \frac{\delta(t - \|\mathbf{x}\|/c)}{4\pi c^2 \|\mathbf{x}\|} \quad \text{Eq. (3.33)}$$

The Green function may be generalized to source distributions and band-limited excitation using the convolution integral. If $S(\mathbf{x}, t)$ describes such a source distribution within an arbitrary spatial support D , the corresponding pressure at any point in space may be evaluated as

$$P(\mathbf{x}, t) = \int_0^t \iiint_D G(\mathbf{x} - \mathbf{x}', t - t') S(\mathbf{x}', t') dV dt'. \quad \text{Eq. (3.34)}$$

For example, if an acoustic source may be approximated by a point source and is located outside the axes origin in \mathbf{x}_0 where it produces a finite bandwidth pulse according to a time function $S(t)$, the pressure evaluates as

$$\begin{aligned} P(\mathbf{x}, t) &= \int_0^t \iiint_D G(\mathbf{x} - \mathbf{x}', t - t') S(t') \delta(\mathbf{x}' - \mathbf{x}_0) dV dt' \\ &= \int_0^t G(\mathbf{x} - \mathbf{x}_0, t - t') S(t') dt' \\ &= -p_0 \frac{S(t - \|\mathbf{x} - \mathbf{x}_0\|/c)}{4\pi c^2 \|\mathbf{x} - \mathbf{x}_0\|}, \quad t \geq \|\mathbf{x} - \mathbf{x}_0\|/c. \end{aligned} \quad \text{Eq. (3.35)}$$

Note again that the power constant is only there to match the physical unit. A few remarks are in order. First, care should be taken while evaluating this type of integrals to preserve causality of the wave solution. Second, in acoustic applications the convolution integral is amenable for numerical evaluation using efficient fast Fourier transformations because the bandwidth is naturally limited by the source time-function. Third, it may be observed that the wave field due to a point source in an infinite homogenous fluid preserves the pulse produced by the source. However, this no longer applies if the source is a distribution or when regarding the scattering of waves. The simplest explanation is that this kind of situations introduces the notion of a size into the equations, which implies wavelength and frequency dependent effects. This will cause the frequency content of the pulse produced by the source to be dispersed through space and time.

3.6.3. Specified Green functions

Specified Green functions are aimed at solving the velocity (\mathbf{V}) or pressure (P) in response to a specific type of source. These derived Green functions are obtained simply by recognition from the wave equations in Eq. (3.15) in a comparison with Eq. (3.32). Note that the superposition principle always applies, which is quite useful for constructing solutions to problems involving arbitrary vector sources. The results are given below.

$$\begin{aligned} G^{Pf}(\mathbf{x}, t) &= c^2 G(\mathbf{x}, t), & \nabla \cdot \mathbf{f} &= \delta(\mathbf{x})\delta(t), \\ G_i^{vf}(\mathbf{x}, t) &= -\frac{1}{\rho} \frac{\partial G(\mathbf{x}, t)}{\partial t} \mathbf{e}_i, & \mathbf{f}_i &= \delta(\mathbf{x})\delta(t)\mathbf{e}_i, \end{aligned} \quad \text{Eq. (3.36)}$$

$$\begin{aligned} G^{PQ}(\mathbf{x}, t) &= -K \frac{\partial G(\mathbf{x}, t)}{\partial t}, & Q &= \delta(\mathbf{x})\delta(t), \\ G_i^{vQ}(\mathbf{x}, t) &= c^2 G(\mathbf{x}, t) \mathbf{e}_i, & \nabla Q &= \delta(\mathbf{x})\delta(t)\mathbf{e}_i. \end{aligned} \quad \text{Eq. (3.37)}$$

The subscript i denotes vector component x , y or z , while the two letters in the superscript on the left-hand side refer to the state variable and the active type of source. The letters \mathbf{f} and Q represent the point body force and the point volume injection source respectively. A slight disadvantage of these Green functions is that the pairs in Eq. (3.36) and in Eq. (3.37) are not matched to the same source. However, for each Green function and source the matching Green function for the other state variable may be calculated using the related source-free equation in Eq. (3.13) or (3.14). The set of specific Green functions in Eqs. (3.36) and (3.37) will be used in Chapter 4 to formulate the relation of ultrasound imaging to inverse acoustic problems.

3.7. Acoustical characterization of polyolefin plastics

A potential quantitative application of acoustic waves, besides imaging, is classification or identification of plastics. The background is that the MDS separates plastics solely on the basis of mass density, but different types of plastic may share the same density. A typical example is LDPE and PP. The use of acoustic waves for detecting deviating particles within a supposedly clean product stream would make a potential online quality assessment tool for MDS. For linear acoustic waves the scope is limited to the detection of mass density, compressibility and material-specific attenuation. A paramount question to be answered in this section is how acoustically distinctive the different types of polyolefin are? The chemical and material scientists have proven quite successful in modifying polymers to just about any desired engineering application or customer property. Consequently, there are more than 100.000 polymer variants that all end up in the waste mixture. Fortunately, for polyolefin it is possible to

group them on the basis of mass density and dominant molecular structure. These groups are identified:

- Polypropylene (PP)
- Low-density polyethylene (LDPE)
- Linear low-density polyethylene (LLDPE)
- High density polyethylene (HDPE)
- Ultra-high molecular weight polyethylene (UHMWPE)

It is not implied that this grouping is absolute. For example, a compounder would also rank them according to physical properties such as melt-flow index and blow-mould or injection mould quality. It should also be mentioned that properties may be significantly modified by additives such as colours (e.g. carbon black or Titanium white) and flame retardants. Nevertheless, this grouping is relevant and represents most of the plastics found in household waste and car shredder residue, which are important sources of high-quality recycling plastics.

3.7.1. Attenuation in plastics

In nature the energy carried by acoustic waves is quickly lost. The attenuation may be due to several mechanisms: geometrical spreading of the energy in space, refraction and scattering at material boundaries, scattering on the micro scale in grainy materials and energy absorption (e.g. friction, phonon scattering) in the propagating medium. The physics behind acoustic wave absorption is complicated as it is usually nonlinear in nature and quite specific for the material at hand. Fortunately, acoustic practice shows that the absorption and micro-scattering mechanisms may both effectively be modelled as a type of viscosity. A causal, first order relaxation function is introduced that extends the constitutive equation in Eq. (3.11) to absorbing media.

$$\nabla \cdot \mathbf{V} = -\kappa(t) * \frac{\partial P}{\partial t}. \quad \text{Eq. (3.38)}$$

The asterisk denotes convolution in time and κ is the time-dependent compressibility. There are various choices that could be made for κ , and here is defined specifically as

$$\kappa(t) = \frac{\kappa_0}{2} \left(\delta(t) + H(t) \exp(-t/\tau) \right). \quad \text{Eq. (3.39)}$$

Here $\delta(t)$ and $H(t)$ denote the Dirac function and Heaviside step function respectively, and τ is relaxation time. A longer relaxation time corresponds to stronger material attenuation.

3.7.2. Measurement and classification of polyolefin groups

Figure 3.3 shows the calibrated set-up for measuring acoustic compressibility and relaxation time. Plastic plates of thickness $d=0.5\text{--}3$ mm were vertically immersed in the small water basin and subjected to a transmission measurement at a right angle of 90° with respect to the plate. The transducers fired wave pulses of 5 MHz centre frequency and 80% bandwidth. The acoustic wave speed of the plastic c_{pol} was calculated using the difference in transmission travel time T_r with and without the plastic sample as

$$c^{pol} = 1/(1/c^{water} - T_r/d). \quad \text{Eq. (3.40)}$$

The mass density was determined by weighing and using a Pico meter for volume measurement. All measurements were repeated a few times to confirm reproducibility.



Figure 3.3. Set-up for the measurement of acoustical properties of flat polyolefin plates.

In this setup the shear waves proved negligible as the transmission occurred at practically right angles through the relatively thin plates, which were homogeneous and isotropic. Each sample was flat and large enough to intercept the whole wave beam, which avoided scattering from edges and basin walls. Under these conditions, without loss of generality, the acoustic attenuation in the present measurements may be investigated using the acoustic fluid model. The advantage is that it required only one set of stiffness and compressibility parameters, while it would be double for the elastodynamic model. The applied 3D fluid model was based on numerical evaluation of the Fourier-domain Green function for acoustic waves in multi-layered attenuating media [Kennett 1983]. In the present case there are only three layers: water-plastic-water. The analytical approach, implemented in Matlab, also allowed exact modelling of the wave diffraction due to the circularly

shaped transducers used in this setup, cf. Figure 3.3. The plastic viscosity was modelled according to Eq. (3.39).

Attenuation and wave velocity were measured by matching the calculated signal to the acoustic data. For improved accuracy the characteristic source time function was calibrated first. For this purpose the signal of a measurement without sample was deconvolved with the corresponding Green function. This operation removes the influences of both wave propagation and transducer diffraction from the received signal and isolates the source time function. Table 3.1 compiles the measurements for the various plastic samples. The attenuation of water can be used as reference value which is 0.02 dB/cm/MHz [Hoskins 2010] and this is much lower than the plastic materials in Table 3.1.

Classification of the polyolefin groups may be performed by first plotting the data in Table 3.1 in a multi-dimensional scatter plot. Subsequently, a classification algorithm may be applied to determine in which parts of the scatter space the data for a certain polyolefin group may be found with highest probability. That probability will depend on the amount of overlap between the data from different groups, meaning that some plastic particles could be classified into different groups with different probabilities. Examples of classification methods are adaptive boosting and a neural network [Anthony 1999]. It is noted that to reach reliable statistics for these methods many more samples would have to be added to those of Table 3.1.

Table 3.1. Acoustic properties of polyolefin samples at room temperature and 5 MHz centre frequency.

Sample material	Density [kgm ⁻³]	Wave speed [ms ⁻¹]	impedance [MRayl]	relaxation time [ns]	attenuation [dB/cm]
PP	894	2540	2.27	5.3	43.8
PP	895	2337	2.09	3.5	31.8
PP	910	2671	2.43	3.6	29.0
HDPE	951	2370	2.25	1.6	14.4
LDPE	905	2174	1.97	2.5	24.5
LDPE	905	2170	1.96	3.8	37.1
LLDPE	906	2239	2.03	3.8	36.0
LLDPE	906	2253	2.04	5.2	48.4
UHMWPE	943	2338	2.20	1.6	14.6
UHMWPE	943	2312	2.18	1.8	16.6

The product of physical material stiffness and relaxation time is a sensitive parameter for classification and reflects the phenomenological inverse relation between the two. If the material stiffness of a polyolefin decreases, for example

due to a rise in temperature or a chemical-physical treatment, the acoustic attenuation usually increases and vice versa. The product is referred to as *specific stiffness* and is calculated as

$$S = Z c \tau. \quad \text{Eq. (3.41)}$$

Here Z is the acoustic impedance, c is wave velocity and τ is relaxation time. The specific stiffness and wave velocity scatter plots for the samples in Table 3.1 are plotted against mass density in Figure 3.4 and Figure 3.5.

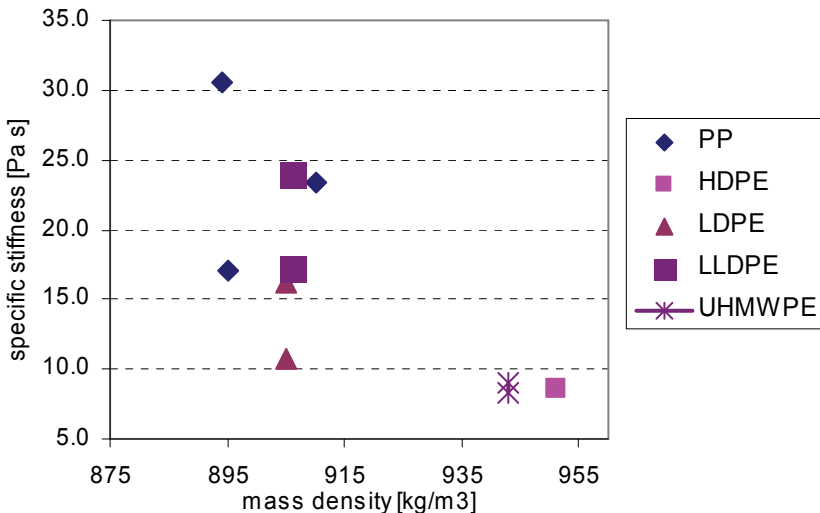


Figure 3.4. Specific stiffness against mass density as a sensitive 2D scatter plot to distinguish between different groups of polyolefin.

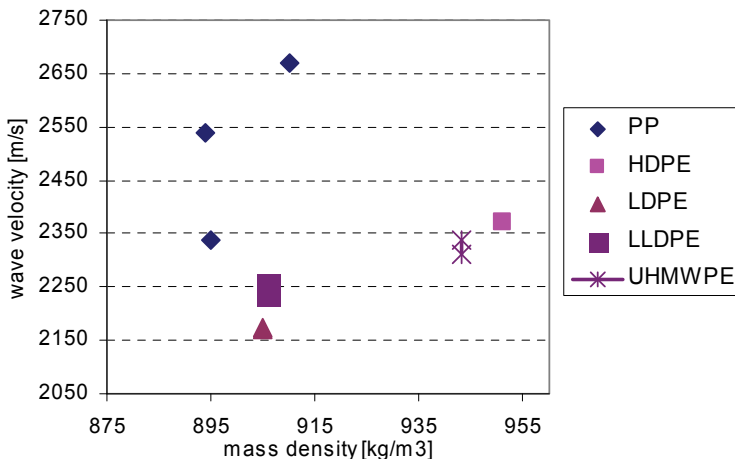


Figure 3.5. Acoustic wave speed against mass density as another example of a 2D scatter plot.

The 2D scatter plots already show the tendency of the plastics to form isolated groups. Polypropylene (PP) tends to have the highest velocity and specific stiffness and differs in that combination from all the other groups. LLPDE and LDPE seem to differ most noticeable in the specific stiffness. On the other hand, the heavier PE groups are quite different from the others but they appear quite close in these scatter plots. It is concluded from this limited dataset that polyolefin groups may be quite distinctive in their combined acoustic properties.

A few remarks are in order. First, the results on the basis of Table 3.1 only give an indication of the possible success of an acoustic technique for polyolefin classification or identification. No statistically relevant conclusions can be drawn based on this limited dataset. Second, practical situations offer a-priori information which simplifies classification, such as the fact that not all types of polyolefin will be found together in significant quantities in a waste stream. For example, UHWPE and LLDPE are special plastics which are not commonly found in household waste.

3.7.3. Signal strength in the MDS setting

Linear sensor arrays for medical applications produce experimental data with a typical dynamic range of 25dB. Because our objective is to image plastic particles in an MDS the obvious question is which signal-to-noise ratio (SNR) may be expected under those conditions? For example, is it possible to obtain quality data from a plastic particle by scanning through another particle floating above it? To gain some insight into these technological issues we analyse the situation in Figure 3.6, which shows a generic 1D layered configuration where two plastic sheets are positioned parallel in a fluid. This situation represents an idealised MDS situation with one type of particle floating above the other in a magnetised ferrofluid. The 1D transmitter/sensor is positioned above the fluid. The thickness of the plastic sheets is varied between 1 and 4 mm to study the range of achievable SNR.

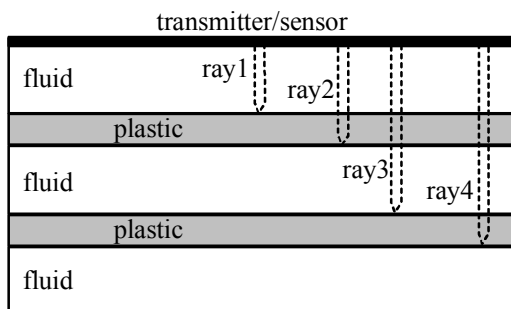


Figure 3.6. Idealised 1D configuration of an MDS scenario with two plastic sheets in ferrofluid.

The acoustic attenuation model used is a straightforward multiplication of plane wave transmission and reflection coefficients, combined with the viscous attenuation inside the plastics. The coefficients are introduced here from literature [Szabo 2004]. If the incident wave propagates downwards from material layer a to b , the coefficients are

$$\begin{aligned} R_{ab}^D &= (Z_b - Z_a) / (Z_a + Z_b), \\ T_{ab}^D &= 2Z_b / (Z_a + Z_b). \end{aligned} \quad \text{Eq. (3.42)}$$

If the incident wave propagates upwards from layer b to a , the coefficients are

$$\begin{aligned} R_{ba}^U &= (Z_a - Z_b) / (Z_a + Z_b), \\ T_{ba}^U &= 2Z_a / (Z_a + Z_b). \end{aligned} \quad \text{Eq. (3.43)}$$

Here, $Z = c\rho$ denotes the acoustic impedance of a layer. For the modelled attenuation only the four primary rays are regarded, i.e. wave trajectories with only one reflection. These are indicated in Figure 3.6. The two different types of plastics used in the simulations are polypropylene (PP) and polyethylene (PE). The resulting attenuation calculates as

$$\begin{aligned} \text{ray1: } & 20 \log 10 \left(\left| R_{f;pp}^D \right| \right), \\ \text{ray2: } & 20 \log 10 \left(\left| T_{f;pp}^D R_{pp;f}^D T_{pp;f}^U \right| \right) - 2\alpha^{PP} d, \\ \text{ray3: } & 20 \log 10 \left(\left| T_{f;pp}^D T_{pp;f}^D R_{f;pe}^D T_{f;pp}^U T_{pp;f}^U \right| \right) - 2\alpha^{PP} d, \\ \text{ray4: } & 20 \log 10 \left(\left| T_{f;pp}^D T_{pp;f}^D T_{f;pe}^D R_{pe;f}^D T_{pe;f}^U T_{f;pp}^U T_{pp;f}^U \right| \right) - 2\alpha^{PP} d - 2\alpha^{PE} d. \end{aligned} \quad \text{Eq. (3.44)}$$

Here, α denotes wave attenuation [dB/cm] and d [cm] denotes the thickness of a plastic sheet. The parameters used in the calculations are PP on the second line and PE on the fourth line of Table 3.1. The numerical result for a PP sheet on top is shown in Figure 3.7(a) and the situation for a PE sheet on top is shown in Figure 3.7(b).

The PE material is a bit more reflective than PP as the attenuation shown by Ray 1 is somewhat higher in Figure 3.7(a). Material attenuation is a dominant factor and causes the increase in attenuation with particle thickness. As mentioned, the average dynamic range in experimental data from a linear sensor array lies at ~ 25 dB. Since arrays are aimed at imaging the surface in direct view of the array, this means that in Figure 3.7 there is a margin for yet another 25 dB before the noise level is reached. This assumed noise level is shown in Figure 3.7 by the dashed horizontal line at -40 dB. As an interpretation, this noise level would indicate that for both cases the whole thickness of the bottom plastic sheet would be within the dynamic range of the sensor array if the thickness is below ~ 2.5 mm.

However, in the real MDS setting the waves are also attenuated due to geometrical spreading and scattering at the small sized, rather irregularly shaped flakes. In fact, each reflection and transmission coefficient in Eq. (3.44) should be complemented with an additional attenuation factor to account for these mechanisms. As 3 dB per coefficient seems possible, the 25dB noise margins in Figure 3.7 may just not be enough to put the lower plastic flake in the dynamic range of the acoustic data unless the top flake is quite thin or PE.

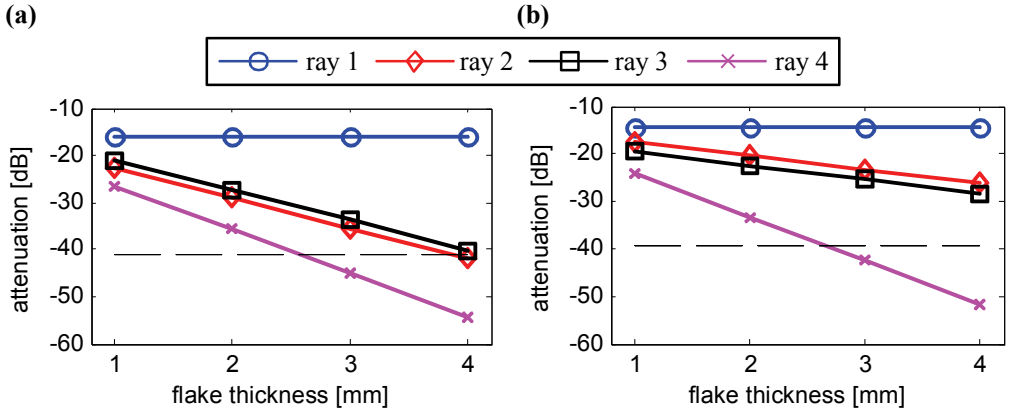


Figure 3.7. Estimated minimum attenuation of the primary rays depicted in Fig. 3.10 against flake thickness. (a) PP sheet on top, PE below it. (b) PE sheet on top, PP below it.

3.7.4. Wave shielding due to critical refraction

When an acoustic wave encounters a material boundary, part of the acoustic energy is transmitted and the complement is reflected. Physically, this partition of the incident energy is driven by the continuity of the acoustic pressure and displacement across the boundary. As far as the direction of the wave trajectory is concerned, the continuity conditions become manifest in the wavenumbers on both sides of the boundary. Figure 3.8(a) shows a ferrofluid-plastic boundary with an incident pressure wave. Figure 3.8(a) shows that the incident pressure wave produces both a transmitted compression wave and a transmitted shear wave in the solid plastic. The fact that the type of wave has changed, here from pressure to shear, is referred to as *mode conversion*. The wavenumbers in Figure 3.8(a) comply with

$$k_F \sin(\phi^I) = k_F \sin(\phi^R) = k_P \sin(\phi^P) = k_S \sin(\phi^S). \quad \text{Eq. (3.45)}$$

In fact, when expressing the wavenumbers in terms of frequency and wave velocities this may be recognized as Snell's law:

$$\frac{\sin(\varphi^I)}{c_f} = \frac{\sin(\varphi^R)}{c_f} = \frac{\sin(\varphi^P)}{c_p} = \frac{\sin(\varphi^S)}{c_s}, \quad \text{Eq. (3.46)}$$

where c_f , c_p and c_s represent the acoustic pressure wave velocity in ferrofluid, compressional wave velocity and shear wave velocity in plastic.

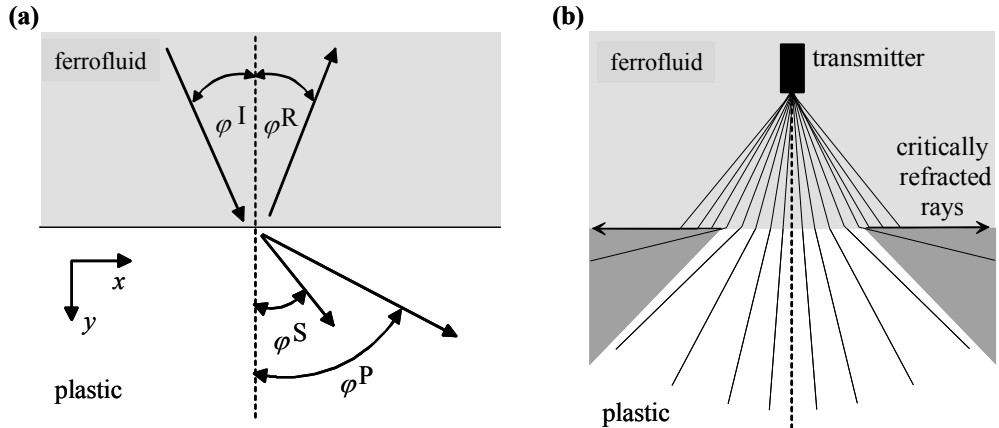


Figure 3.8. (a) Plane wave refraction at a material boundary. (b) A transmitter in the ferrofluid produces a beam of waves, here represented as discrete rays. The refracted beam is more dispersed, while the outer rays are critically reflected, leaving a part of the plastic to be poorly illuminated (dark grey regions).

Snell's law for transmitted waves loses its physically intuitive interpretation when the refraction angle becomes larger than 90° . This happens at a certain angle of the incident wave when the velocity of the transmitted wave is higher than that of the incident wave. The associated angle where the transmitted wave breaks under 90° is called the *critical angle*, causing the wave to effectively travel along the interface. For example, the critical angle for an incident pressure wave from a fluid to plastic is $\arcsin(C_f/C_p)$. When exceeding the critical angle, the transmitted waves no longer penetrate the material and that part of the interior becomes practically inaccessible to types of wave that are useful for imaging. This scenario is shown in Figure 3.8(b). Instead, the critically refracted wave will generate interface wave phenomena, such as head waves, Scholte, Stoneley or Rayleigh waves [Achenbach 1975], depending on the materials on either side of the interface and the interface conditions.

Figure 3.8(b) shows a typical setup with a transducer producing a beam of waves towards the interface with a plastic. The refracted beam inside the plastic is

more dispersed, meaning it is weaker and broader than in the ferrofluid, for example when measured between the -20 dB points. The parts of the generated beam that are incident above the critical angle are critically refracted along the interface. The combination of strong dispersion of the beam in the plastic towards the interface and the critical refraction of a part of the incident beam leaves the dark grey parts of the plastic to be very poorly illuminated. This makes it practically impossible to perform imaging in those parts of the plastic, unless the transmitter position is moved. For a small plastic waste particle these “shadow zones” also arise, but are obviously more complicated due to the 3D particle geometry.

The above situation applies to smooth interfaces and homogeneous materials. In cases where the interface is irregular or a material is inhomogeneous, on the scale of the propagation wavelength or smaller, all angles of incidence may effectively exist at the material boundary and transmission and reflection is solely determined by scattering.

References

- [Achenbach 1975] J. D. Achenbach, Wave propagation in elastic solids, Amsterdam, Elsevier Science Publishers B. V., 1975.
- [Aki 2002] K. Aki and P. G. Richards, Quantitative Seismology: Theory and Methods, University Science Books, 2002.
- [Moon 2004] Moon G. Lee, Sung Q. Lee and Dae-Gab Gweon, Analysis of Halbach magnet array and its application to linear motor. *Mechatronics*, 14, pp. 115-128, 2005.
- [De Hoop 1995] A. T. de Hoop, Handbook of Radiation and Scattering of Waves, London, Academic Press, 1995.
- [Kennett 1983] B. L. N. Kennett, Seismic Wave Propagation in Stratified Media. Cambridge, New York, Cambridge University Press, 1983.
- [Hoskins 2010] P. Hoskins, K. Martin and A. Thrush, Diagnostic Ultrasound Physics and Equipment, New York, Cambridge University Press, 2010.
- [Anthony 1999] M. Anthony and P. L. Bartlett, Neural Network Learning: Theoretical Foundations. New York, Cambridge University Press, 1999.
- [Szabo 2004] T. L. Szabo, Diagnostic Ultrasound Imaging: Inside Out. Elsevier 2004.

Chapter 4: Ultrasound imaging in space-time domain

4.1. *Introduction to imaging*

Acoustic imaging allows an object surface in direct view of acoustical sensors to be observed. To that end, the object is irradiated with acoustic waves and scattered waves are detected and recorded. The scattering is due to differences in acoustic impedance that always occur at material boundaries. The recorded data are processed using a mathematical algorithm that maps the data to an image that a human operator can interpret.

For example, Figure 4.1(a) depicts a typical situation where an object immersed in a fluid is interrogated using acoustic transmitters and the scattered wave field is received by sensors. The acoustic devices are preferably employed at many different positions relative to the unknown object to increase the effective range of angles under which the object surface is interrogated and data can be collected. The spatial range spanned by the transmitters or sensors is commonly called the *aperture*. A larger aperture improves the quality of the dataset in the sense that it contains more of the information required to obtain an accurate reconstruction of the object surface. To facilitate scanning over larger apertures the linear acoustic sensor array is commonly employed, rather than mechanical scanning of individual acoustic transducers. Moreover, the piezoelectric elements in the sensor array may be used both as a transmitter and/or a receiver to illuminate the object under different angles. A second general requirement for obtaining high quality data is a large bandwidth. To this end, the acoustic waves should be generated within a wide range of frequencies. This improves the contrast and sensitivity for small details in the image.

From the mathematical point of view an imaging technique may be regarded as a method for obtaining an approximate solution to the acoustic equations and boundary conditions for the configuration at hand. This is complicated due to the fact that it essentially deals with an inverse problem where a part of the configuration, i.e. the object, is unknown. Instead, some acoustic data is available that gives implicit information on the object in the form of scattered waves. To obtain an accurate object surface reconstruction requires a certain amount of information and thus quality data. Despite the current state of the art in imaging, it appears as yet impossible to predict with certainty which method of acquiring data, or indeed how much, is sufficient for obtaining an accurate reconstruction independent of the shape and acoustic properties of the unknown object. In addition to the uncertainty in data quality, the accuracy of the resulting image also depends on the type and possible grouping of multiple objects and the imaging technique used. This means the notion of ‘quality data’ remains subjective as it apparently depends on whether the obtained image quality is satisfactory for the human operators involved. Scientifically unsatisfactory as this may be, the technological potential of acoustic imaging is already duly recognised. In this

chapter and the next the most promising imaging techniques are investigated with a view towards application in wet plastic waste processing, particularly the situation where small plastic particles float inside a ferrofluid.

4.2. Relation to the inverse scattering problem

The mathematical-acoustic foundations of the imaging technique have to be explained to reveal generic properties and dependencies common to all imaging techniques. Figure 4.1(a) shows a generic scenario where transmitters emit an incident wave into the medium. The object has different acoustic properties than the surrounding fluid in which it is immersed. Therefore, the incident wave is scattered at object boundaries and the scattered field is then recorded by receivers. Note that, here, we start from a very generic scenario where the transmitters and receivers are located at arbitrary positions outside the object in space. The developed imaging formula may be adapted later to the data scanned by a linear array. If the object shape and its properties would be known the situation describes a *linear forward scattering problem* [De Hoop 1995]. The wave field solution to this type of problem may be obtained with any desired degree of accuracy by a variety of analytical-numerical approaches. However, commonly the object is unknown and instead only some wave scattering data is obtained. In this case the situation in Figure 4.1(a) defines a nonlinear type of problem called an *inverse scattering problem* and the objective is to reconstruct the object and its material properties. The solution to the inverse problem is considerably more complicated as it may prove to be non-unique (more solutions are possible) and ill-posed [Devaney 1978] (numerical instability of the solution).

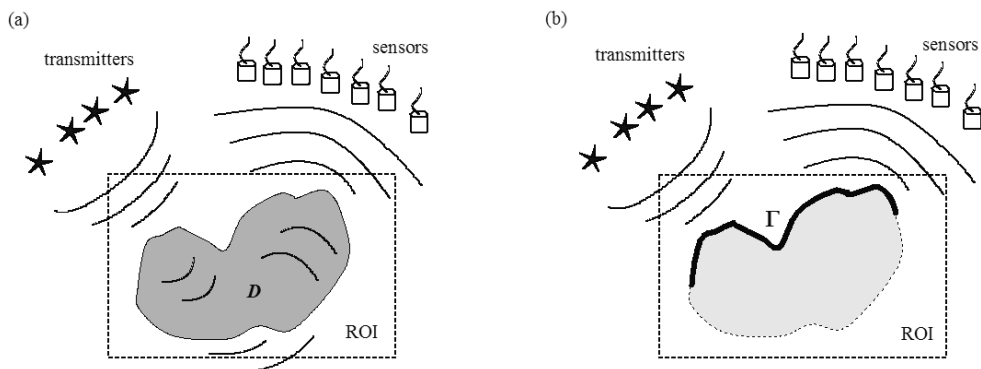


Figure 4.1. (a) Characteristic setup for scanning data of an immersed object in an inverse scattering problem with a suggested region of interest (ROI). (b) Imaging interpretation where only front surface waves are taken into account.

To appreciate the inverse problem the governing integral equation is written below, following manipulation of the basic acoustic equations according to a reciprocity theorem in the time domain [De Hoop 1995]. It is recalled that the general approach in this thesis is to effectively model small scattering solid objects as fluids, i.e. only compressional waves are regarded and mode conversions at the object surface are neglected:

$$P(\mathbf{x}^R, t) = P^{inc}(\mathbf{x}^R, t) + \iiint_D (\kappa^{fl} - \kappa^{ob}(\mathbf{x})) P(\mathbf{x}, t) *_t G^{PO}(\mathbf{x}, \mathbf{x}^R, t) dV + \iiint_D (\rho^{fl} - \rho^{ob}(\mathbf{x})) \sum_{i=1}^3 V_i(\mathbf{x}, t) *_t G_i^{vf}(\mathbf{x}, \mathbf{x}^R, t) dV, \quad \text{Eq. (4.1)}$$

$\kappa^{ob}(\mathbf{x}) = \kappa^{fl}$ and $\rho^{ob}(\mathbf{x}) = \rho^{fl}$ for $\mathbf{x} \notin D.V$

Note that in Eq. (4.1) the acoustic object parameters (i.e. inside the domain D) are a function of \mathbf{x} , and may be interpreted either as homogeneous functions (as in $\kappa(\mathbf{x}) = \kappa_0$) or as inhomogeneous functions, defining an inhomogeneous object. The asterisk denotes a time-convolution, the summation expresses the in-product between the velocity vector and the Green function vector, and the other symbols are explained in Table 4.1.

Table 4.1. Symbols used in Eq. 4.1.

symbol		superscript	
V_i	Acoustic velocity vector component	fl	surrounding fluid
P	Acoustic pressure	ob	object
G	Green's function	R	sensor positions (data collection)
κ	Compressibility	Q	point volume injection source
ρ	mass density	f	point body force
ROI	region of interest	inc	wave field in absence of object

Eq. (4.1) shows that the pressure data (left-hand side) is due to the superposition of the incident pressure field plus two terms that depend on the differences in acoustic properties between the object and the surrounding fluid. The incident wave field is the wave field generated by the transmitters in the absence of the scattering object. The last two terms on the right-hand side represent the wave field scattered by the object as a result of contrast in mass density and/or compressibility. The combination of a contrast function multiplying the unknown field term is called a *contrast source of the scattered field*, in analogy to a *forward source problem* involving only a known Green's function and source term. In case the object is a plastic waste particle inside ferrofluid both contrast sources clearly play a role in the scanned pressure data. Note that in Eq. (4.1) the Green's functions for pressure and/or velocity are linked to the specified Green functions in the pairs of Eq. (3.36) and Eq. (3.37).

The nonlinear nature of the inverse problem is due to the multiplication of the unknown field term and unknown specific acoustic property of the object in each contrast source. However, Eq. (4.1) lends itself to a range of numerical solving strategies since the integral conveniently runs over a bounded domain. Moreover, since the object position and its shape are unknown, it proves very convenient that the region of interest (ROI) may be chosen arbitrarily, and should of course contain the object.

4.3. Imaging principles

Inversion aims at solving for the acoustic object properties as a function of spatial variables using experimental scattered wave field data. Imaging aims only at revealing the position and shape of the irradiated object surface and is based on acoustic reflectivity. To arrive at a generic imaging approach the exact scattering equation Eq. (4.1) has to be approximated in some convenient way, for which a reflection function appears most appropriate. The data is then interpreted in terms of reflections at acoustic impedance jumps and wave propagation effects between the object front surface and the receivers.

A simple experiment is conducted to show this concept is consistent with Eq. (4.1). Suppose space is subdivided into two homogenous halfspaces with a plane interface. One of them is D that has acoustic properties different from the embedding fluid in the other halfspace. The interface is at $y=0$. Suppose a plane pressure wave field P^{inc} is excited at y^T in the embedding and propagates perpendicular to the interface. The pressure observed by a receiver in the embedding at x^R is easily determined as:

$$P(y^R, t) = P^{inc}(y^R - y^T, t) + R P^{inc}(y^R + y^T, t) \quad \text{Eq. (4.2)}$$

Here R is the plane pressure wave reflection coefficient. The first term on the right-hand side is the direct incident wavefield and the second term is the wave field reflected from the interface. When comparing to Eq. (4.1), it may be concluded that the two domain integrals will yield a simple reflected plane pressure wave in the embedding. The fact that a set of domain integrals can produce an external wavefield that is related only to the domain boundary demonstrates that Eq. (4.1) can be quite difficult to interpret physically. However, because Eq. (4.1) gives an exact description of the linear scattering problem, it is best suited for a rigid mathematical treatment or as a basis for numerical solving routines. For our imaging purposes we seek to develop a useful approximation to Eq. (4.1), based on this physically intuitive example.

First the two domain integrals in Eq. (4.1) are replaced by one boundary integral and a reflectivity function $R(\mathbf{x})$ is introduced to represent the acoustical material contrast. This makes the formulation independent of whether a difference in mass density and/or compressibility caused the scattering. Second, the total pressure inside the object is of course unknown, and is for simplicity represented

by a Green function that will only account for the propagation from the source to the scattering surface. This intuitive interpretation of Eq. (4.1) leads to the following approximation:

$$P^S(\mathbf{x}^R, t) \approx \iint_{\Gamma} R(\mathbf{x}) G(\mathbf{x} - \mathbf{x}^T, t) *_{\mathbf{t}} G(\mathbf{x}^R - \mathbf{x}, t) dA, \quad \text{Eq. (4.3)}$$

where, Γ is the domain boundary (see Figure 4.1(b)).

The superscript S indicates the received recorded scattered wavefield, by which we may ignore the direct incident wave field term. The reflectivity function is now amenable for direct reconstruction by using *back-propagation* and *stacking*. Back-propagation means applying an inverse Green function (or inverse operator) that propagates the data signal back in time and back to the (assumed) original scattering position. This is accomplished by a Green function G^{BP} (back-propagation operator). Stacking is the summation of the back-propagated data signals. A physical interpretation of stacking is that it mimics Huygens's principle where multiple small wavelets may produce a coherent wave front. The stacking amplitude that is assigned to the reflectivity function complies with the stacked amplitude at the arrival time of the incident wave at the object surface. This is logical since it is from the incident energy that the object surface scattered the detected waves with a coherent incident phase. The reflectivity becomes high in case of coherent summation and the pertaining position in the ROI must be consistently interpreted as being a part of the object surface:

$$R(\mathbf{x}) \approx \sum_n P(\mathbf{x}_n^R, t) *_{\mathbf{t}} G^{BP}(\mathbf{x} - \mathbf{x}_n^R, -t), \quad \text{for } t = \Delta t(\mathbf{x}), \quad \mathbf{x} \in \text{ROI}. \quad \text{Eq. (4.4)}$$

Here $\Delta t(\mathbf{x})$ denotes the arrival time of the incident wave field at the surface in absolute time, assuming the transmitter was activated at $t=0$. Since the ROI is spatially discretized it is common to associate the local reflectivity function with a *point scatterer*. In other words, the scattering from a surface may be approximated by a distribution of point scatterers spanning that surface. The basic imaging procedure implied by Eq. (4.4) hides a small deficiency, as the characteristic pulse produced by an acoustical transmitter is never zero-phase. This means the peak energy occurs slightly later than at the theoretical arrival time Δt of the incident wave at the object surface. Therefore the energy is still relatively small at the arrival time, which may result in a noisy image. To circumvent this problem, the stacked signal may be first cross-correlated with the source signature function. This operation produces a zero-phase spectrum in Fourier domain and this implies that in time-domain the peak energy will appear at the desired arrival time Δt . A side effect of this operation is that the data signals are no longer causal, meaning there is signal even before any physical acoustic wave could have arrived. This may cause some loss of image quality as reconstructed edges or small details are 'smeared out' in the image.

The analysis in this section linked the general imaging approach to the underlying inverse scattering problem to establish generic properties and dependencies of imaging techniques. First, they tend to ignore the multiple waves inside an object as well as possible multiple waves in between objects. Similarly, they cannot deal properly with strongly inhomogeneous materials. As a consequence, the related physical signals are not properly accounted for and that may cause artefacts to show up in the image depending on the relative signal energies. It is therefore customary during acoustic data scanning to avoid as much as possible the presence of disturbing reflectors in or near the ROI. Second, imaging techniques do not recognize whether a reflection is caused by differences in mass density and/or compressibility. However, if there is sufficient a-priori knowledge about possible object materials the reflectivity amplitude may be calibrated. For example, if the objects involve only a few types of polyolefin materials the reflectivity function may be a quite useful tool in plastics identification, as shown in Chapter 2.

Two remarks are in order. First, the analyses in this section and the preceding one could also be carried out in the complex Fourier domain. That gives the opportunity to replace computationally expensive space-time domain procedures, for example with an efficient direct mapping approach. In fact, application of the fast Fourier algorithm has given rise to quite a few efficient approaches to imaging, which will be addressed in Chapter 5. Second, the current trend in imaging techniques is to get closer to the physics, which is properly embedded in the inverse scattering problem, and thus to account more accurately for all acoustic wave data. The main challenge will be to achieve it efficiently without running into the typical complications associated with solving the full inverse wave scattering problem.

4.4. Time domain SAFT

The synthetic aperture focusing technique (SAFT) is based on radar techniques developed just after the Second World War. The radar data were recorded as a sequence of pulses while moving a small radar device, equivalent to building a pulse-echo data scan. These data are processed using delay-and-sum (DAS) techniques to create a synthetic focus in the observation points of interest. The resulting focusing proved equally effective as one obtained with a non-moving radar device with a very large aperture. This large virtual aperture is also known as a *synthetic aperture*. Later on the method was adapted to acoustic imaging, for example synthetic aperture sonar (SAS) [Hayes 2009], non-destructive testing (NDT) [Langenberg 1986] and medical imaging [Karaman 1995]. In fact, the space-time domain SAFT is equivalent to Kirchhoff migration method developed in seismic [Wiggins 1984]. The main difference would be that SAFT does not account for the attenuation due to geometrical spreading.

SAFT requires that the region of interest (ROI) is located in the far field of transmitters and sensors so their directivity does not play a role. This condition can

be difficult to fulfil in acoustics where the wavelengths are very much smaller than for radar waves and therefore acoustic sensors appear relatively large compared to the wavelengths. However, the influence of sensor diffraction may be suppressed in the SAFT image by applying weighting methods.

An advantage of time domain SAFT is its flexibility towards the scanned dataset, which does not have to comply with any orderly method of data scanning. In principle, transmitters and sensors may be positioned as deemed convenient. This flexibility allows SAFT also to make full use of the scanning capacity of a linear sensor array. Each piezoelectric sensor element may function as either a transmitter or a sensor, by which full use is made of the aperture of the array. This is also called a *full dataset* which contains all the possible information and different datasets which may be obtained using a linear array. In fact, an array of N sensor elements allows for N^2 permutations of transmitter-sensor positions, resulting in $N(N+1)/2$ independent measurements. For example, a sensor array with 128 elements may deliver 8256 independent measurements. Note that reciprocity implies that a measurement gives identical results when the sensor and transmitter positions are interchanged.

The SAFT principle is demonstrated using two different datasets. In Figure 4.2(a) a single acoustic transducer is scanned along the x -axis and transmits and detects acoustic waves from discrete positions. This results in a *pulse-echo* data scan. Note that in Chapter 3, z -axis was used to represent depth in a xyz -Cartesian coordinate system. From this point on in the thesis, y -axis will be used to express depth for a 2D imaging problem.

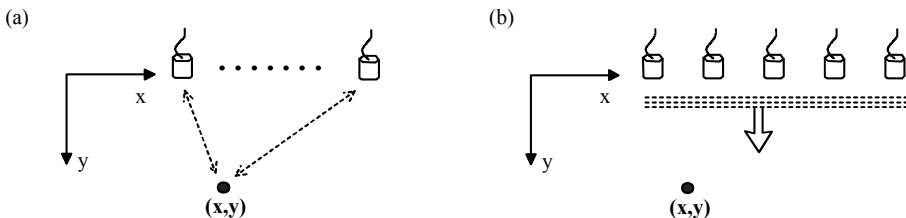


Figure 4.2. Set-up with a point scatterer. (a) Pulse-echo data scan. (b) Plane wave data scan.

By applying appropriate time delays to the data signals a synthetic focusing effect can be created that is comparable to that of a hardware focus. Thus, the data delays effectively replace the delays that should have been applied to the transmitters to produce the hardware focusing. But in contrary to hardware focusing, synthetic focusing allows complete elimination of the travel time from the transmitter to the scatterer, which for the pulse-echo scan is given by

$$\Delta t^{PE}(x, y) = \sqrt{(x - x_n)^2 + y^2} / c, \quad n = 1, 2, \dots . \quad \text{Eq. (4.5)}$$

Here c is the acoustic wave speed of the ferrofluid. What remains is to back-propagate the signals from the sensor to the scatterer and stacking them in accordance with the procedure explained for Eq. (4.4). The back-propagation for time domain SAFT is performed in a simplified way by merely shifting the data signals back in time. Since the wave path to and from the scatterer is the same in pulse-echo measurements, the reflectivity function may be assigned according to

$$R^{PE}(x, y) = \sum_n D(x_n, 2\Delta t^{PE}(x, y)), \quad (x, y) \in \text{ROI}. \quad \text{Eq. (4.6)}$$

In Figure 4.2(b) an array of acoustic sensors is positioned along the x -axis. At $t=0$ all sensors are excited simultaneously after which each sensor scans for data, resulting in a *plane-wave* data scan. The time delay from transmitter to scatterer, back-propagation and reflectivity function are

$$\begin{aligned} \Delta t^{PW}(y) &= y/c, \\ R^{PW}(x, y) &= \sum_n D(x_n, \Delta t^{PE}(x, y) + \Delta t^{PW}(y)), \quad (x, y) \in \text{ROI}. \end{aligned} \quad \text{Eq. (4.7)}$$

Note that the back-propagation time delay is the same as for pulse-echo. It is noted that before assigning the reflectivity a Hilbert transformation may be applied to improve the signal-to-noise ratio in the SAFT image.

4.5. Advancing on time domain SAFT

4.5.1. Aperture weighting

The conventional time domain SAFT does not take into account the directivity of the sensor and hence treats it as an ideal point element. The realistic, finite-sized sensor causes diffraction patterns which may affect the contrast and resolution in the SAFT image. The diffraction effects may be reduced by applying weighting to the synthetic data aperture. The idea behind it is to give less weight to signals back-propagated under large angles since they may be assumed to carry less energy than signals at steep angles, e.g. a surface reflection under a straight angle. Consequently, the signals from larger angles may contribute more noise than signal to the stack. The aperture weighting function is based on the spatial angle between the target location in the ROI and the sensor. Where the energy in the beam is reduced to a given minimum level is referred to as the beam divergence angle Φ_b . The weighting function is then defined as a number between zero and unity according to

$$W_n(x, y) = \exp\left(-\left(\Phi/\Phi_b\right)^2\right). \quad \text{Eq. (4.8)}$$

Here, Φ is the angle between the central sensor axis and the vector pointing from the sensor to the target location. The SAFT algorithm may be modified to include weighting according to

$$R(x, y) = \sum_n W_n D(x_n, \Delta t) . \quad \text{Eq. (4.9)}$$

4.5.2. Adaptive weighting

There are several causes why a reflectivity function may show a significant value even though there was no object surface in the synthetic focus. This may be due to:

- waves not accounted for in the approximations leading to the imaging principle
- modelling uncertainties (variation in acoustic wave speed, sensor positioning)
- deviating sensor properties (side lobes, bandwidth limitations)
- noise sources (dust or gas bubbles in the ferrofluid)
- limited data (non-uniqueness)

An erroneous high reflectivity causes artefacts to show up when the reflectivity function is interpreted by the operator as an image. Adaptive beam forming is aimed at improving image quality through better focusing despite unexpected small errors. Two methods are here introduced for suppressing artefacts in a SAFT image.

Coherence Factor (CF): The coherence of the N back-propagated signals in the stack is assessed according to [Liao 2004]

$$CF(x, y) = \frac{\left| \sum_n D(x_n, \Delta t) \right|^2}{N \sum_n |D(x_n, \Delta t)|^2} . \quad \text{Eq. (4.10)}$$

The numerator is proportional to the average energy per signal after back-propagation and stacking. The denominator is proportional to the sum of energies of the signals after back-propagation. This defines the CF as a real quantity between zero and unity, where unity indicates that signals are perfectly coherent across the synthetic aperture. The CF weighted reflectivity is implemented as

$$R^{CF}(x, y) = CF(x, y) R(x, y) . \quad \text{Eq. (4.11)}$$

In practice, if the CF is near unity the original image intensity is effectively maintained, while a low CF will reduce the image intensity proportionally and thus suppress artefacts.

Generalized Coherence Factor (GCF): As an ansatz, Parseval's theorem for discrete FFT data is written as (the details are presented in Appendix A):

$$\sum_{n=-N/2}^{N/2-1} |\tilde{D}(k_n)|^2 = N \sum_{n=1}^N D(x_n)^2. \quad \text{Eq. (4.12)}$$

The left-hand side sums the data in the wavenumber-time domain and the right-hand side sums them in the space-time domain. Both are the back-propagated signals, where the time argument is omitted for simplicity. Eq. (4.12) can be put to use when it is noted that the phase of low wavenumber components are much less sensitive to aberrations than high wavenumbers that are associated with much smaller wavelengths. This gives rise to an adaptive weighting technique called GCF [Li 2003], which is defined as the ratio of spectral energy in a range of low wavenumbers and the total spatial energy:

$$GCF(x, y) = \sum_{n=-n0}^{n0} |\tilde{D}(k_n)|^2 / \sum_{n=-N/2}^{N/2-1} |\tilde{D}(k_n)|^2. \quad \text{Eq. (4.13)}$$

Here $n0$ corresponds to the index of the chosen cut-off wavenumber of the selected range. The implementation of GCF is the same as Eq. (4.11) for CF. High values indicate that most of the spatial energy is contained within the low-wavenumber range and may be expected to result in correct focusing. As an advantage over CF, GCF also suppresses small noise-generating objects in the image, for example specks of dust in the ferrofluid. As a slight drawback, GCF takes more computational effort than CF due to the additional FFT.

4.5.3. Time-frequency domain SAFT

The complex data spectrum may contain most of its useful information in a certain frequency band, which property is already utilized in adaptive weighting. It may be of advantage if the specific frequency content could also be addressed in combination with a time-domain SAFT approach. This perhaps counter-intuitive idea has led to the development of what is called time-frequency domain SAFT. The one difference with time domain SAFT is that the back propagation is carried out only in a selected frequency band Ω . This is achieved by first transforming the data to frequency domain:

$$D(x_n, \omega) = \int D(x_n, t) \exp(-i\omega t) dt. \quad \text{Eq. (4.14)}$$

Next, only the selected frequency band of interest is shifted back in time (earlier in time) by applying the following operation in frequency domain for each (x, y) in space:

$$\begin{aligned} D^{BP}(x_n, \omega) &= D(x_n, \omega) \exp(i\omega^s \Delta t(x, y)), \\ \omega^s &= \omega \text{ for } \omega^s \in \Omega, \\ \omega^s &= 0 \text{ for } \omega^s \notin \Omega. \end{aligned} \quad \text{Eq. (4.15)}$$

Finally an inverse Fourier transform gives the desired data in time-domain:

$$D^{BP}(x_n, t) = \frac{1}{2\pi} \int D^{BP}(x_n, \omega) \exp(i\omega t) d\omega. \quad \text{Eq. (4.16)}$$

This data is now ready for the stacking procedure, and then the reflectivity function is obtained by summation at $t=0$:

$$R^{BP}(x, y) = \sum_n D^{BP}(x_n, t=0), \quad (x, y) \in \text{ROI}. \quad \text{Eq. (4.17)}$$

Since other frequencies are not back propagated they remain incoherent and will be suppressed by the stacking. The advantage of this approach is that it allows image reconstruction to be performed within a controlled bandwidth, while still allowing absolute freedom in the building of the dataset which is one of the major advantages of time-domain SAFT. A drawback is that it is even more time consuming than time-domain SAFT due to the additional FFT.

References

- [De Hoop 1995] A. T. de Hoop, *Handbook of Radiation and Scattering of Waves*, London, Academic Press, 1995.
- [Devaney 1978] A. J. Devaney, Nonuniqueness in the inverse scattering problem, *J. Math. Phys.* 19 (1978), pp. 1526-1531.
- [Hayes 2009] Michael P. Hayes and Peter T. Gough. Synthetic Aperture Sonar: A Review of Current Status, *IEEE Journal of Oceanic Engineering*, Vol. 34, No.3, pp. 207-224, July 2009.
- [Karaman 1995] Mustafa Karaman, Pai-Chi Li and Matthew O'Donnell. Synthetic Aperture Imaging for Small Scale Systems, *IEEE Transactions on Ultrasonics, Ferroelectrics, and Frequency Control*, Vol. 42, No.3, pp. 429-442, May 1995.
- [Langenberg 1986] K. J. Langenberg, M. Berger, Th. Kreutter, K. Mayer and V. Schmitz. Synthetic aperture focusing technique signal processing, *NDT International*, Vol. 19, Issue 3, pp. 177-189, June 1986.
- [Liao 2004] C.-K. Liao, M.-L. Li and P.-C. Li. Optoacoustic imaging with synthetic aperture focusing and coherence weighting, *Optics Letters*, Vol. 29, No.21, pp. 2506-2508, November 1, 2004.

[Li 2003] Pai-Chi Li and Meng-Lin Li. Adaptive Imaging Using the Generalized Coherence Factor, *IEEE Transactions on Ultrasonics, Ferroelectrics, and Frequency Control*, Vol. 50, No.2, pp. 128-141, February 2003.

[Wiggins 1984] J. W. Wiggins. Kirchhoff integral extrapolation and migration of nonplanar data, *Geophysics*, Vol. 49, No.8, pp. 1239-1248, August 1984.

Chapter 5: Ultrasound imaging in the Fourier domain

5.1. *Background and objectives*

Chapter 4 was dedicated to imaging principles in the physical space-time domain, but imaging may also be performed in a mathematical transform domain such as the Fourier domain. The Fourier domain based techniques are computationally more efficient, owing to the decomposition of the complex wave field into plane waves and the availability of the highly efficient fast Fourier transform (FFT). In particular, the plane wave decomposition of the wave field facilitates both the interpretation of the complex wave fields and the development of efficient approximating analyses. Fourier domain techniques were therefore soon adopted into the acoustic field, providing lower execution times at the acceptable technological cost of an increase in memory usage [Langenberg 1986]. The *frequency-domain SAFT*, F-SAFT for short, is a markedly successful wavenumber-frequency domain imaging method, and a platform for various performance enhancing adaptations. For example, in an adapted version of F-SAFT a direct mapping is applied between the frequency and depth wavenumber spectra to allow for full FFT evaluation of the image, which highly efficient method known as *Stolt migration* [Stolt 1978]. Nevertheless, as a general rule, the more efficient the method, the less flexible it is towards the method of data collection and the configurations it can handle.

The time-domain techniques from Chapter 4 were developed using the assumption that the finite size of plastic waste particles may be ignored. By that assumption only the boundary of the object in direct view of the probe was considered for imaging. An important step forward towards a more quantitative ultrasound imaging technique is to deliver shape-consistent images of both the front and the back surface of the plastic particle, i.e. to provide an accurate cross-section reconstruction. This will require more advanced imaging techniques that can utilize the waves emerging from the plastic. Size and shape consistent images of plastic particles can deliver different kinds of quantitative information that can be of great value for experimental studies and for plastic waste processing capability:

- Particle shape and size recognition improves particle tracking, as it allows a particle's centre of gravity and orientation in the fluid to be identified in different images. This capability helps to study the flow and turbulent conditions of the ferrofluid in an MDS. For example, the particle motions during mixing and density separation, detection of flow turbulence, or study of turbulence levels and size of flow eddies.
- More accurate volumetric measurements of plastic particles may be performed for estimating the uniformity of the MDS feed and mass

throughput as function of depth and relative position in the channel. This constitutes an improvement over the pixel intensity detection based method, introduced in Section 2.5.

- Cross section imaging may show if particles in the MDS are segregating, i.e. clustering according to size or shape, which could be occurring naturally in the feed or extraction units of the MDS where particles are abundant and the flow is turbulent.
- Plastic flakes may possibly be statistically linked to the original end-of-life (EOL) product types on the basis of shape, thickness, surface roughness and edge sharpness as a result of the waste shredding process. For example, in household waste we would expect to find flakes belonging to a range of shampoo bottles, soda bottles, butter cups, and cutlery. As another distinction, house hold waste is usually thin-walled while automotive industry commonly produces thicker plastics with also more distinguishing properties towards strength, stiffness, wear resistance and/or chemical resistance. These detectable ultrasound links will allow us to connect MDS product quality to specific EOL sources of plastic waste. This will lead to a more thorough understanding of the relation between product design, manufacturing and recyclability.

5.2. Fourier imaging overview

Ultrasound data allows imaging of the back surface (dashed line, indicated by Ψ in Figure 5.1) of an acoustically penetrable object, even when using one-sided access with a single, position-fixed sensor array. Note that the probe should preferably be fixed in a streamlined position in the MDS since it could otherwise disturb the laminar flow. The ultrasound wave field propagating out of the object supplies the information required for back-surface imaging. It may be comprised of different types of wave that are categorized as:

- Primaries, which reflected only once at the object back surface
- Multiples, which reflected more than once inside the object
- Mode-converted waves, (possibly a primary or a multiple) which interchanged (possibly more than once at boundaries) between the compression mode and shear mode of propagation.

In the above list only the isolated object is considered such that the possible exchange of acoustic energy between particles may be ignored, for example a plastic particle moving freely in ferrofluid. At an interface the propagation velocity, amplitude and angle of propagation of the transmitted wave can change, which complicates the reconstruction procedure for back surface imaging. Multiples and mode-converted waves are reputedly the most difficult to interpret and isolate in a

dataset, even though they hold (redundant) information on the material boundaries and could be potentially of use for imaging. However, the contribution of these waves is explicitly ignored in this chapter, but they could possibly be employed to confirm that the primaries-based reconstruction of the particle cross section is accurate by means of forward wave field modelling, i.e. as a check after the fact.

In principle, time-domain SAFT can be adapted to any type of wave, but it would result in a cumbersome approach due to the requirement of having to accurately match the correct refraction angles and wave velocities at both sides of the particle boundary. Therefore, this chapter is aimed at investigating the potential of Fourier domain algorithms, originally developed for geophysics and/or NDT purposes, and to adapt them to the configuration, ultrasound data and conditions imposed by an industrial MDS.

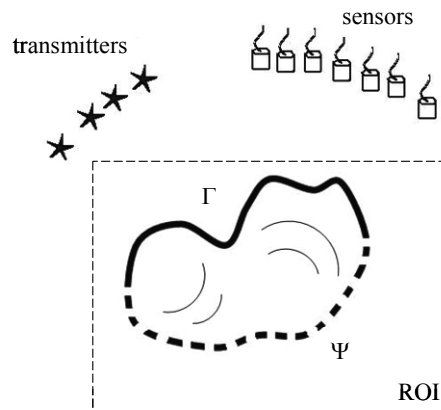


Figure 5.1. Wave reflections inside the object allows for back surface imaging.

Two different techniques related to cross section imaging are developed: *wave field redatuming* and *migration*. The aim of wave field redatuming is to approximate the data at receiver positions where it is either impossible or unattractive to place a real receiver. For example, we would like to place receivers in direct contact with the plastic particle front surface (Γ in Figure 5.1). This would eliminate the water wave paths in between the current sensor positions and the particle. Though physically impossible to realize for a freely moving particle, it is possible to approximate the data that would be obtained at those positions using the experimental data that is collected at a distance from the particle. This procedure has been studied rather extensively for geophysical applications [Wapenaar 1989]. Not unexpectedly, the conditions for obtaining a good approximation are quite similar to those for obtaining a good quality ultrasound image: the physical data should be well sampled and provide a wide range of viewing angles on the perceived virtual receiver locations.

In geophysics, migration is generally viewed as an acoustic image reconstruction technique that is based on the scalar wave equation. These methods typically downward-continue the acoustic data into depth, sometimes in small steps using for example finite differences [Etgen 2009]. Each step is accomplished by inverse wavefield extrapolation that is formulated using operators in the Fourier domain, while neglecting any horizontal variation of the wave velocity in the medium. The reconstruction is obtained by imposing the imaging condition, i.e. determining the extrapolated wavefield amplitude at the moment the incident wave reached the boundary. While forward extrapolation aims at creating the effects of wave propagation outside the data domain, migration applies to inverse extrapolation and aims at undoing the effects of wave propagation outside the data domain. Obviously, the success of migration will largely depend on the validity of the used forward wave model.

In the wavenumber-frequency domain the wave field extrapolator can be readily obtained from the wave equation, and may be applied either *recursive* or *non-recursive*. In a non-recursive approach (e.g. Stolt migration), the recorded wavefield at the level of the probe is used to compute the wavefield at a different level. However, in a recursive method, the wavefield at the next level is computed using the calculated wavefield at the preceding level, not necessarily the probe level. The advantage of recursive extrapolation is that medium velocity variations in the extrapolation direction, commonly in depth, can be taken into account in an efficient way. On the other hand, recursive techniques are sensitive to the accumulation of various types of error introduced in each step.

In seismology, *phase shift migration* was developed for imaging internal earth layers and performing imaging in a horizontal homogeneously layered configuration [Gazdag 1978]. This method employs operators that extrapolate recorded data to the subsequent plane interfaces, in which it proves computationally more efficient than Kirchhoff migration (SAFT). *Phase shift plus interpolation (PSPI)* was developed to deal with media involving smooth horizontal velocity variations [Gazdag 1984]. The PSPI principle is based on linear interpolation between apriori introduced reference velocities in each extrapolation step to account for the horizontal smoothly varying wave velocity. The success of PSPI depends heavily on the choice of the reference velocities, but it tends to improve when the number of reference velocities is increased. The PSPI method may be altered to obtain the *non-stationary phase shift (NSPS)* [Margrave 1999]. In NSPS, the choice of reference velocities and the method of interpolation are resolved by taking an exhaustive set of reference velocities for each real velocity value. In other words, the method interpolates extensively between the known horizontal velocities in the medium. For completeness, it is noted there are also space-time domain extrapolation methods, but these are ignored as they do not add much information to the present research.

Chapter 5 presents a theoretical investigation into Fourier-domain imaging methods and their advantages and limitations. As a rule, a method may deliver better quality images when it is more in line with physics. A general limitation of

FFT-based methods is that the dataset must be built in accordance with the spatial sampling theorem, i.e. according to the Nyquist criterion and with evenly spaced receivers. Fortunately, these conditions may be met with the linear sensor array.

The imaging methods in this chapter are based on the reflection-boundary integral model introduced in Eq. (4.3). This means that the scatterer is thought to be replaced by a virtual acoustic source that is activated at the arrival time of the incident wave and then effectively ‘produces’ the reflected wave. This constitutes an approximation of the exact forward scattering problem by two consecutively executed forward source problems, which are mathematically easier to solve. The first is the calculation of the incident wave field produced by the physical sources, which wave propagation effects are ignored in many imaging approaches. The second forward source problem is the virtual source response, mimicking the actual wave scattering process.

In imaging, the moment of arrival of the incident wave at the scatterer is commonly normalized to $t=0$, by which the backpropagated wave field will produce at $t=0$ the correct position of the cause of the physically recorded scattered waves. This is known as the *imaging condition*. A requirement for this condition to work is that the wave amplitude is maximum at $t=0$, which in reality cannot be realized to perfection. The reasons are that causality prevents any wave energy to exist before $t=0$, while all acoustic systems and data are bandlimited. It is noted that the Dirac delta pulse, i.e. the mathematically perfect jump at $t=0$, is therefore also not a physically realizable pulse. As a possible solution, the recorded data may be correlated with the recorded transmitter signature, which is the characterizing bandlimited acoustic pulse produced by the transmitters. This computational trick puts the maximum energy at the arrival time of the wave at the cost of some reduction in bandwidth. Note therefore that the amplitude spectrum is squared by correlation.

5.3. Wave field redatuming

The purpose of redatuming is to calculate the wave field at a different position in space than where the receiver data were recorded. For our purposes the physical wavefield is recorded by a line sensor array, but it will be shown that redatuming can completely change this simple acquisition geometry. At first sight there seem to be two possible applications for redatuming.

First, it may bring the data acquisition plane closer to a scattering object in a homogeneous medium. This may sound like a useful option, because when the acquisition plane is closer to the object it increases the range of viewing angles, i.e. also much more sloping viewing angles would contribute to the reflection data. However, the redatumed data is recalculated from the physical data, and if such sloping angles were not part of the data in the first place they will not show up after redatuming either. In other words, the redatumed data cannot contain more information than the physically recorded data. Therefore, it appears that

redatuming holds no advantage if the objective is to improve image quality in a homogenous medium.

The second application for redatuming is clearly useful, and that is to create the new acquisition plane on the interface between two different materials. This eliminates the wave paths in the first material, and would allow for imaging of scatters beyond the interface to be conducted without the complicating refraction effects of the interface, i.e. without the need to invoke Snell's law and coping with two wave velocities. This creates possibilities for applying efficient imaging methods that are usually limited in that they cannot deal with inhomogeneous media. Moreover, the redatuming may be applied recursively, thus allowing the redatumed data to be redatumed to yet another level or interface.

5.3.1 Redatuming to a parallel plane interface

The general idea is depicted in Figure 5.2. Figure 5.2(a) shows a 2D cross section of a plastic particle suspended in ferrofluid. The data are recorded at the level y_0 and denoted as $P(x, y_0, t)$. In Figure 5.2(b) an operation is conducted that replaces physical receivers with virtual ones on the front surface of the particle that is in direct view of the physical data acquisition plane. This new data acquisition surface directly samples the plastic particle. This new, non-plane acquisition surface can be realized in two steps. First, new acquisition planes are created at the levels (depths) of the virtual receivers. From each plane, only the data at the position x_p of the desired virtual receiver is retained. Of course, if all the target virtual receivers were already on one plane, the procedure would be much faster. The key issue is therefore to obtain the redatumed data at a certain plane, in this case at the depth y_p . The scattering objects causing the reflection data are located in the half-space $y > y_0$. The Fourier transform of the physically recorded wave field is

$$\hat{P}(k_x, y_0, \omega) = \iint P(x, y_0, t) \exp(-i\omega t) \exp(ik_x x) dt dx. \quad \text{Eq. (5.1)}$$

The acoustic field at the new depth y_p can be found by inverse extrapolation:

$$\hat{P}(k_x, y_p, \omega) = \hat{P}(k_x, y_0, \omega) \exp\left(ik_y (y_p - y_0)\right), \quad \text{Eq. (5.2)}$$

where the wavenumber k_y is defined as

$$k_y = \begin{cases} \sqrt{(\omega/C)^2 - k_x^2}, & (\omega/C)^2 - k_x^2 > 0, \\ 0, & (\omega/C)^2 - k_x^2 \leq 0. \end{cases} \quad \text{Eq. (5.3)}$$

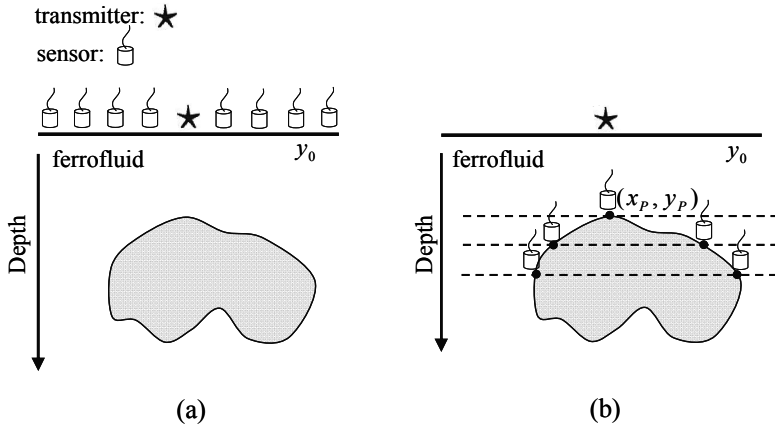


Figure 5.2. The general idea behind redatuming. (a) Physical experiment. (b) Experiment with a virtual data acquisition plane on the particle surface.

Here, C may be either a physical or an effective wave propagation velocity. In Eq. (5.3) the wave field must be necessarily limited to propagating waves, corresponding to real-valued wavenumbers, to avoid instability due to inversion of evanescent waves. A consequence of this truncation is that it may lead to artefacts, in particular non-causal ones that will be visible as events ahead in time of the correctly redatumed waves. The inverse Fourier transform is performed to produce the space-time data at the new depth:

$$P(x, y_p, t) = (1/2\pi)^2 \iint \hat{P}(k_x, y_p, \omega) \exp(-ik_x x) \exp(i\omega t) dk_x d\omega. \quad \text{Eq. (5.4)}$$

Two important examples concern the effective wave propagation velocities for a pulse-echo (PE) and a plane-wave (PW) dataset, where we assume the redatuming will take place in ferrofluid,

$$\text{PE data: } C = c_f / 2, \quad \text{PW data: } C = c_f. \quad \text{Eq. (5.5)}$$

The PE dataset is special because the transmitter and receiver are at the same position and the data obtained from any receiver is causally related to only one transmitter. In other words: the PE data is not blended. For this dataset the transmitter and receiver cannot be decoupled using redatuming, since it would imply creating a type of blended dataset for which the relation between the transmitted fields and the receiver data is lost. As a consequence, redatuming of a PE set can only be performed with half the wave propagation velocity to create a new PE dataset at the new depth. In contrary, redatuming of a PW dataset will leave the transmitters at the physical location and create only virtual receiver

positions and accompanying data at the new depth. Thus, depending on the type of dataset and targeted virtual acquisition surface, redatuming may completely change the original physical data acquisition geometry.

5.3.2 Redatuming to a sloping plane interface

In the special case where the interface with the next medium layer is plane and sloping under a not too steep angle, it is possible to create a virtual data acquisition plane on the slope in one single step. To that end, the physical data is extrapolated under an angle towards the sloping interface in a procedure which in essence is identical to beam steering. To demonstrate the concept, the analysis starts with the space-time domain data. To extrapolate line sensor array data under an angle means to propagate it back in time and space as an angled beam of waves, which beam is projected orthogonal onto the slope. Appropriate time delays dt are required for each transmission element of the sensor array to achieve beam steering. For this purpose it is convenient to introduce the concept of a moving trigger with constant velocity v , which is thought to activate the transmitter elements on its arrival at $t=x/v$, upon which the transmitters will generate a wavefront under the beam angle φ :

$$\tan(\varphi) = C/v, \quad 0 \leq \varphi < \pi/2. \quad \text{Eq. (5.6)}$$

As before, C may be either a physical or an effective wave propagation velocity of the medium above the sloping interface. The beam-steering concept may be easily adapted to the mirror-image case of beam forming in the opposite horizontal direction, keeping in mind that the trigger then starts moving from the other end of the sensor array. Next, the time-delayed data are transformed to the Fourier domain, similar to Eq. (5.1)

$$\hat{P}(k_x - k_v, y_0, \omega) = \iint P(x, y_0, t - x/v) \exp(ik_x x) \exp(-i\omega t) dt dx, \quad \text{where } k_v = \omega/v. \quad \text{Eq. (5.7)}$$

This shows that beam steering results in a phase shifted wavenumber spectrum, which was expected since the beam is aimed off-axis in a horizontal direction. Obtaining the virtual recorded data on the sloping interface runs analogous to Eq. (5.2)-(5.4) and is presented here without further details.

$$\begin{aligned}
\bar{P}(\bar{k}_x, \bar{y}, \omega) &= \hat{P}(k_x - k_V, y_0, \omega) \exp(i k_y R), \quad \text{with } R = \Delta y \cos(\varphi), \\
P(\bar{x}, \bar{y}, t) &= (1/2\pi)^2 \iint \bar{P}(\bar{k}_x, \bar{y}, \omega) \exp(-ik_x x) \exp(i\omega t) dk_x d\omega, \quad \text{Eq. (5.8)} \\
k_y &= \begin{cases} \sqrt{(\omega/C)^2 - (k_x - k_V)^2}, & (\omega/C)^2 - (k_x - k_V)^2 > 0, \\ 0, & (\omega/C)^2 - (k_x - k_V)^2 \leq 0. \end{cases}
\end{aligned}$$

Figure 5.3 indicates the reference distance R , the depth Δy to the interface, the enclosed beam steering angle φ , and the new receiver coordinates (\bar{x}, \bar{y}) with the origin on the sloping interface. The collected PE and PW datasets may be redatumed in accordance with the effective wave velocity in Eq. (5.5). The redatumed data are then amenable for application in efficient, single wave velocity imaging methods.

The redatumed data will be sampled more closely due to the downsizing skew projection from the original aperture to the virtual, cf. Fig. 5.3. This implies improved spatial resolution for scatterers that are well in view of the new virtual receiver aperture. However, the reduction in aperture also reduces the range of viewing angles available for imaging, which will negatively affect the obtainable resolution for objects that do not nicely fit inside the view of this smaller aperture.

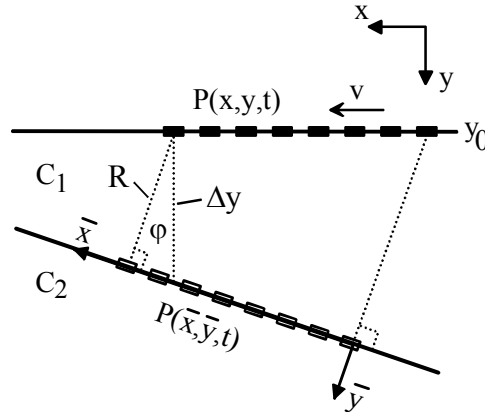


Figure 5.3. One-step redatuming concept for a sloping interface. A trigger moves with constant speed v to activate transmitters that generate a plane wavefront, orthogonal to the slope under the angle φ . On arrival, this plane wave produces the virtual data.

5.4. F-SAFT

F-SAFT is an imaging technique based on the redatuming principle. The method basically uses redatuming and employs the imaging condition, eliminating the transmitter-to-scatterer delay time to achieve focusing at $t=0$. As mentioned before, signature correlation may be required first to achieve the best results for this method. We start from Eq. (5.2), which is modified to

$$\hat{P}(k_x, y, \omega) = \hat{P}(k_x, y_0, \omega) \exp(i k_y (y - y_0)) \exp(i \omega \Delta \tau^T(y)). \quad \text{Eq. (5.9)}$$

The wavenumber k_y is defined in Eq. (5.3). The delay $\Delta \tau^T$ is the time it takes the incident wave to propagate from the transmitter to the scatterer at (x, y) , which is compensated for with a phase shift backward in time. As with redatuming in Eq. (5.5), two important examples concern the PE and a PW datasets. Assuming imaging will take place in ferrofluid:

$$\begin{aligned} \text{PE data: } \quad \Delta \tau^T(y) &= 0, & C &= c_f / 2, \\ \text{PW data: } \quad \Delta \tau^T(y) &= |y - y^T| / C, & C &= c_f. \end{aligned} \quad \text{Eq. (5.10)}$$

The superscript T indicates the transmitter depth. Again, the PE dataset is special since taking half the wave propagation velocity already eliminates the transmitter-to-scatterer delay time. These Fourier data are transformed back to the space-time domain to obtain the reflectivity function by applying the imaging condition $t=0$,

$$R(x, y) = (1/2\pi)^2 \iint \hat{P}(k_x, y, \omega) \exp(-ik_x x) d\omega dk_x, \quad (x, y) \in \text{ROI}. \quad \text{Eq. (5.11)}$$

The purposely chosen object surface (2D) that contains the scattering object is referred to as the *region of interest* (ROI). Evaluation of a PE dataset requires just one evaluation of Eq. (5.11). However, due to the depth dependent time delay in Eq. (5.10), the evaluation of a PW dataset will produce a focused result only at depth y , i.e. only the image line corresponding to depth y will be imaged correctly. Therefore, the full focused image will have to be assembled line-by-line, which increases the computational burden correspondingly.

5.5. Stolt migration

Stolt migration, also known as (ω, k) migration, appears to be the fastest method currently known when combined with a PE dataset. To that effect it uses Fourier transforms and interpolation techniques to map the recorded wave field to an image in a single processing step. In this section, Stolt migration is explained specifically

for the PE data. First, the derivation follows the F-SAFT approach up to Eq. (5.11). The wavenumber integral may be solved using the fast Fourier transform, but the omega integral is different. The exponential term $\exp(ik_y(y-y_0))$ of the kernel in Eq. (5.9) suggests that it can be used to transform the omega integral in Eq. (5.11) into a Fourier-type integral by a change of variable from ω to k_y . This change of variable is performed by employing the dispersion relation in Eq. (5.3). The Jacobian $J(k_x, k_y)$ of this transformation follows from the dispersion equation from which Eq. (5.3) and then Eq. (5.11) may be rewritten as:

$$\begin{aligned} R(x, y) &= (1/2\pi)^2 \iint \left[J(k_x, k_y) \hat{P}(k_x, k_y) \exp(ik_y(y-y_0)) dk_y \right] \exp(-ik_x x) dk_x, \\ k_y &= \sqrt{(\omega/C)^2 - k_x^2}, \\ J(k_x, k_y) &= Ck_y / \sqrt{k_x^2 + k_y^2}, \quad C = c_f / 2. \end{aligned} \quad \text{Eq. (5.12)}$$

This expression forms the basis for developing the Stolt technique, which enables evaluation of the image using only fast Fourier transforms. In a discretized version using FFT, a complication arises in that the discrete wavenumbers k_y will not be equidistant when mapping them from discrete frequencies ω . The following Stolt procedure presents in four steps a solution to this problem by interpolating the pressure data to make it conform to equidistant wavenumbers K_y (denoted here by a capital to indicate equidistant sampling). Finally, the steps involved in Stolt algorithm can be summarized as follows:

1. Perform a 2D Fourier transform on $P(x, y_0, t)$ to get $\hat{P}(k_x, y_0, \omega)$.
2. Interpolate pressure data to equidistant K_y according to

$$\hat{P}\left(k_x, K_y = \sqrt{(\omega/c_f)^2 - k_x^2}\right);$$

3. Multiply the interpolated pressure data with the Jacobian $J(k_x, K_y)$;
4. Take the 2D inverse FFT to obtain $R(x, y)$.

It is noted that the interpolation process may cause some artefacts in addition to the artefacts already caused by truncation of the wavenumber spectrum in Eq. (5.3).

5.6. SAFT and Redatuming

Plastic particles will not always be flat, meaning that the redatumed data has to be distributed over the curving front surface of a particle in accordance with the redatuming approach described in Section 5.3.1. As a consequence, the new virtual data is not on a flat plane and cannot be handled by the preceding Fourier domain techniques. Fortunately, in these cases the combination of redatuming and time-

domain SAFT (cf. Section 4.4) offers a very flexible and effective solution strategy for imaging of the particle back surface.

Suppose we have N virtual receivers distributed over the front surface of the particle. The coordinates of the transmitters and receivers are indicated with superscripts T and R, respectively. The travelled distance from a transmitter to the (assumed) scatterer at (x, y) and the distance back to the receiver are denoted by R , according to

$$\begin{aligned} R_n^T &= \sqrt{(x - x_n^T)^2 + (y - y_n^T)^2}, & (x_n^T, y_n^T) &= \text{transmitter coordinates}, \\ R_n^R &= \sqrt{(x_n^R - x)^2 + (y_n^R - y)^2}, & (x_n^R, y_n^R) &= \text{receiver coordinates}. \end{aligned} \quad \text{Eq. (5.13)}$$

By denoting the data belonging to receiver n as D_n and referring to Eq. (4.4), the reflectivity function for the particle back surface can be written as:

$$\begin{aligned} \text{redatumed PE dataset: } R(x, y) &= \sum_{n=1}^N D_n \left(t = 2R_n^T / C \right), \\ \text{redatumed PW dataset: } R(x, y) &= \sum_{m=1}^N \sum_{n=1}^N D_n \left(t = |y_m - y_0| / c_f + (R_m^T + R_n^R) / C \right). \end{aligned} \quad \text{Eq. (5.14)}$$

Here, C denotes the homogeneous wave propagation velocity of the plastic particle and c_f the ferrofluid. Note that the reflectivity function extracts the signal amplitude at the arrival time of the calculated ray. This implies that correlation of the raw data with the transmitter source signature may also improve the performance of this hybrid method. To emphasize the special nature of the PE dataset the delay time is defined by twice the transmitter-to-scatter point travel time. Note that the transmitters of the incident plane wave are still at the physical data acquisition depth y_0 , which delay time through the ferrofluid to the SAFT trial transmitter positions on the particle must also be accounted for. The redatumed plane wave dataset requires a double summation, since the curving particle surface refracts, and possible scatters, the incident plane wave by which the incident field is no longer planar inside the particle.

5.7. Phase shift migration

Phase shift migration is applied to horizontally homogeneously layered media and employs a procedure of layer-by-layer F-SAFT imaging and recursive redatuming to the next interface. The concept is depicted in Figure 5.4, which shows an idealization of the vertical cross section of the MDS channel with different flakes of plastics flowing at different depths (alternating layers of plastic and ferrofluid). First, F-SAFT is employed to perform imaging of scatterers in the top layer using the physical data. Subsequently these data are redatumed to the next interface, where it serves as the dataset for F-SAFT imaging in the next layer. Then the

redatumed data is redatumed to the next interface, and so on. This procedure may be repeated for all the deeper layers.

The effectiveness of the method will run out due to accumulating errors in the redatuming or the lack of signal strength from the deeper lying scatterers. Another limitation of phase shift migration is that the interfaces should be sufficiently plane, typically on the scale of a wavelength, since this may also introduce imaging errors. And last, any error in estimating the depth of the next interface from the last image reconstruction will also translate in imaging errors in the next layers.

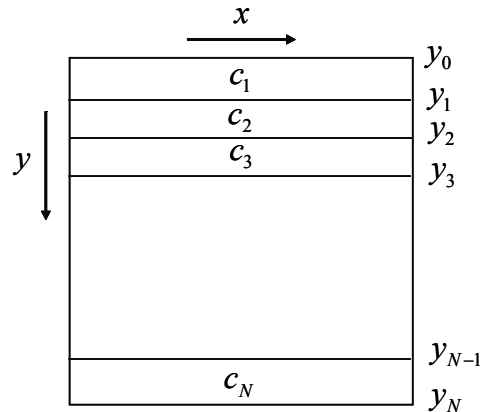


Figure 5.4. A horizontally layered medium allows for phase shift migration.

The pixel strength of the reconstructed scattering objects in the different layers may easily be normalized in the combined image to enhance the visibility. Note therefore that the reflected wave energy decreases with depth and repeated transmission through interfaces.

We remind here that it is possible to redatum to a sloping interface and then perform imaging from the slope into the next layer (cf. Section 5.3.2). However, it should be emphasized that image quality always depends on the availability of good quality (physical) data. In this case, the signal strength and bandwidth obtained from scatterers below a sloping interface is a matter of some concern. In case such a slope is in direct view of the sensor array, physical beam steering by the array may be employed to steer the beam straight onto the interface and provide good irradiation of the scatterers. However, when the sloping layer is embedded in a multi-layered configuration it is much more challenging to provide optimum ultrasound irradiation and collect good quality data at the physical data acquisition plane.

5.8. Non-stationary phase shift migration

The non-stationary phase shift migration (NSPS) method was developed to cope, to a certain degree, with horizontally inhomogeneous media. To that end, imagine a 2D configuration in which the wave velocity $c(x)$ varies only in the horizontal direction. As usual, the first objective is to extrapolate the recorded wave field from the data acquisition plane to a new depth. First, the a priori known wave velocity profile within the horizontal range of the sensor array is discretized using a set of N piecewise constant velocities, denoted as C_n with $n=1..N$. Then, the main idea is to perform F-SAFT as if the medium were homogenous and to perform this for each of the N real velocity values. However, the ROI for each reflectivity function is limited to the horizontal range where the used velocity is valid. Thus, Eq. (5.9) is evaluated with $C=C_n$ in Eq. (5.10), after which the reflectivity function in Eq. (5.11) is evaluated for the ROI where this velocity approximated the real wave velocity of the medium.

Discretization of the inhomogeneous velocity profile in horizontal strips of constant velocity and treating them as if they were piece-wise homogenous has a limited range of validity. However, the method is efficient and valid if the object is close enough to the sensor array or when the viewing angles on the object are quite limited, by which mainly the almost vertically propagating waves contribute to the reflection data. In other cases, i.e. for waves with a significant horizontal direction of propagation, the data may be imaged out of focus and quite likely cause artefacts.

5.9. Computational cost analysis of imaging algorithms

Computational cost translates into economical costs, as it increases the requirements for real-time capability of processing hardware and/or memory storage capacity. A software and hardware independent method for analyzing computational cost of an algorithm is to determine the order of the number of arithmetic operations. In this approach, N_x denotes the total number of sensor positions and N the number of time samples for each sensor position. The total number of backpropagation/extrapolation depths is assumed equal to N , which seems a reasonable assumption for many practical applications. The order of the number of evaluations per processing step for the different imaging methods is presented in Table 5.1. The reader is referred to Appendix B for details on the calculation.

The overall computational effort of an imaging method is shown in Table 5.2, and is determined by the step with the highest order, while a distinction has been made between time samples and sensor positions. The values may be multiplied to indicate the order for both N and N_x .

Stolt migration has the lowest order of evaluations, which confirms its reputation as the fastest migration method known to date. The order with regard to the number of sensor positions is the same for all the algorithms. The fact that the

order for time samples in Table 5.2 is the same for F-SAFT and phase shift migration favours phase shift migration, because it outperforms F-SAFT. The latter is demonstrated in Chapter 6 using experimental data. The NSPS method has the same order for time samples in Table 5.2 as phase shift migration, but unfortunately NSPS has four steps of complexity of order $O(N^2)$ in Table 5.1 against two for phase shift migration. If the size of the data set increases sufficiently this drawback of NSPS with respect to phase shift diminishes and NSPS would always be the best choice in view of its better performance.

Table 5.1. Order of the number of evaluations for processing steps in an imaging algorithm. N is the number of time samples and N_x is the number of sensor positions

Stolt migration		F-SAFT	
Operation	Complexity	Operation	Complexity
FFT (x, t) to (k_x, ω)	$N_x N \log N_x N$	FFT (x, t) to (k_x, ω)	$N_x N \log N_x N$
Interpolation to (k_x, k_y)	$N_x N$	Backpropagation	$N_x N^2$
Amplitude scaling	$N_x N$	Summate ω	$N_x N^2$
IFFT (k_x, k_y) to (x, y)	$N_x N \log N_x N$	IFFT k_x to x	$N_x N \log N_x$
Phase shift migration		NSPS	
Operation	Complexity	Operation	Complexity
FFT (x, t) to (k_x, ω)	$N_x N \log N_x N$	FFT (x, t) to (k_x, ω)	$N_x N \log N_x N$
Extrapolation	$N_x N$	Backpropagation	$2N_x N^2$
Backpropagation	$N_x N^2$	IFFT k_x to x for each y	$2N_x N^2 \log N_x$
Summate ω	$N_x N^2$	FFT x to k_x for each y	$N_x N^2 \log N_x$
IFFT k_x to x	$N_x N \log N_x$	Summate ω for each y	$N_x N^2$

Table 5.2. Order of the number of evaluations for the whole imaging algorithm with respect to N and N_x separately.

Algorithm	N	N_x
Stolt migration	$N \log N$	$N_x \log N_x$
F-SAFT	N^2	$N_x \log N_x$
Phase shift migration	N^2	$N_x \log N_x$
NSPS	N^2	$N_x \log N_x$

References

[Etgen 2009] John Etgen, Samuel H. Gray and Yu Zhang. An overview of depth imaging in exploration geophysics, *Geophysics*, Vol. 74, No.6, pp. WCA5-WCA17, November-December 2009.

[Gazdag 1978] Jeno Gazdag. Wave equation migration with the phase-shift method, *Geophysics*, Vol. 43, No. 7, pp. 1342-1351, December 1978.

[Gazdag 1984] J. Gazdag and P. Sguazzero. Migration of seismic data by phase shift plus interpolation, *Geophysics*, Vol 49, No 2, pp 124-131, February 1984.

[Langenberg 1986] K. J. Langenberg, M. Berger, Th. Kreutter, K. Mayer and V. Schmitz. Synthetic aperture focusing technique signal processing, *NDT International*, Vol. 19, Issue 3, pp. 177-189, June 1986.

[Margrave 1999] G. F. Margrave and R. J. Feguson. Wavefield extrapolation by nonstationary phase shift, *Geophysics*, Vol 64, No 4, pp 1067-1078, July-August 1999.

[Stolt 1978] R. H. Stolt. Migration by Fourier Transform, *Geophysics*, Vol. 43, No. 1, pp. 23-48, February 1978.

[Wapenaar 1989] C. P. A. Wapenaar and A. J. Berkhouit. Elastic wave field extrapolation: redatuming of single and multi-component seismic data, Elsevier, Amsterdam, 1989.

Chapter 6: Imaging performance

This chapter presents and discusses ultrasound images obtained using experimental data with the theory developed in Chapters 4 and 5. The raw ultrasound data are acquired in the laboratory, using dedicated setups that were designed to retrieve high quality ultrasound data from a static scene, i.e. when nothing moves. Doing so, care was taken that the setup mimicked the basic conditions found in a magnetic density separator (MDS). In this study two typical types of data were used: pulse-echo (PE) and plane-wave (PW) data. These data types are complementary since PE has the broader transmitting aperture and PW has the broader receiving aperture.

The possibility to perform cross-section imaging is investigated by simultaneously reconstructing both the front and back surface of an object using the same dataset. This should facilitate the characterisation (i.e. based on shape) or quantitative measuring (e.g. volume) of plastic particle properties. First it is demonstrated that imaging methods are capable of reconstructing the cross section, provided the ultrasound data contain the minimally required information. The available information is investigated more quantitatively by analyzing datasets using ray-tracing. This leads to the insight that only a few types of wave are actually suitable for imaging the whole back surface of a particle, which wave types are subsequently employed for cross section imaging using polymer test objects. The study is completed with recommendations for the applicability of ultrasound imaging in MDS processing and an analysis of the statistical error when measuring properties of large quantities of plastic particles.

6.1. *Data collection*

The commercial probe from the real-time experiments in Chapter 2 was also used in our laboratory experiments, but here it was connected to the dedicated laboratory data acquisition system. The semi-automated data acquisition setup was in principle designed to enable automated scanning of a PE dataset. Fortunately, by a small modification it could also be used to create a PW dataset. To that end, a full dataset would be scanned that was subsequently summed on the computer over all the transmitter positions. The acquisition procedure is shown in Figure 6.1.

The full dataset is obtained by utilizing all the possible permutations when one sensor element acts briefly as a transmitter while subsequently all elements act as receivers. A slight drawback of the present hardware was that in full data scan mode it could not scan data from the transmitting element, which means the pulse-echo signals were not recorded. It is noted that the source signature of PE-data scanned in PE-mode was different and could not be used to replace the missing PE data in the full data scan mode. This, though, did not prove a limitation, since the missing data may be extrapolated on the computer using redatuming in the element direction (x -direction, cf. Section 5.3.2), although it proved also valid to use direct

interpolation from neighbouring sensor signals. All 127 receiving elements were activated in turn by a matrix-switch, which was controlled through a LAN interface by the computer. The transmitting element, having fired 127 times, was changed manually from one element to the next. Thus, the full dataset before PE-interpolation comprised 128x127 measurements.

The transmitter element was excited by a rectangular pulse of 100 V/100 ns and data were recorded using a 40 MHz/16 bit digitizer. This resulted in a bandwidth of typically 2-7 MHz in the recorded reflection data. The acquisition procedure takes several minutes, which is why only static scenes could be imaged using the laboratory setup. However, this did not pose a limitation to the research as far as the envisioned real-time application is concerned, since a static particle may be perceived as a snapshot of the moving particle. In case of a moving particle a small Doppler shift could be observed in the recorded frequency. Assuming a flow velocity of 500 mm/s for a plastic particle in the MDS channel, a ferrofluid wave velocity of 1480 m/s and 5 MHz probe frequency, the maximum Doppler shift is still only 1.7 kHz. This is very small with respect to the frequencies of the probe and may be ignored in real-time imaging.

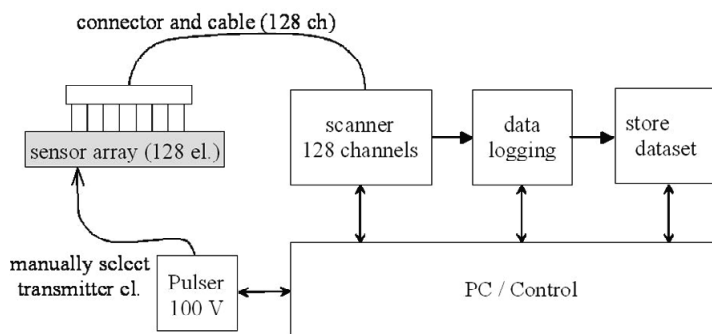


Figure 6.1. Experimental procedure for collecting data of a static scene, using a semi-automated data scanner to control the 128 sensor elements in either PE mode (no manual transmitter element select) or full dataset mode.

6.2. Image quality

An ultrasound image may be subjected to all kinds of image processing tricks to enhance the features that could be of importance for a human interpreter. The quality of the resulting image is therefore quite subjective, also because human visual perception and cognitive capabilities differ from person to person. To fully overcome this limitation, the interpretation of image quality should preferably be carried out using image processing software and be measured on a unit scale. Unfortunately, this is as yet impossible. Therefore, all image processing done in

this chapter only served to ensure visibility of the reconstructed object boundaries, because the objective is to compare imaging techniques and not image processing techniques. Moreover, here, image quality may readily be judged by the reader according to the following four performance indicators. All four are to be judged in a comparison to the pixel levels of the background (noise) and/or surrounding objects:

- Sharpness: Degree to which the object boundaries are distinctive.
- Resolution: Smallest object that is still sharply discernable.
- Contrast: Degree to which the object pixel levels stand out.
- Shape consistency: Match between the reconstruction and the object shape.

In the following test cases image quality is investigated in relation to signal-to-noise-ratio and spectral contents of the data. For this purpose a setup with three thin plastic plates was used of which a cross-section, direct in view of the sensor array, is shown in Figure 6.2(a). The plates were 50 mm long (in out-of-plane direction) to approximate a 2D cross section for the sensor array. The plates were fully immersed in a water tank and PE and PW data were collected.

6.2.1. Sharpness and signal-to-noise-ratio

When evaluating image quality, an obvious question that comes to mind is what sharpness may we expect in an image and how is it affected by different scanning methods and/or different imaging algorithms? It seems obvious that it should improve with a better SNR of the data, but the exact relation is unclear. In Figure 6.2(a), a setup is introduced with thin, flat plastic plates with sharply defined edges, which is ideal for investigating image sharpness. A PE dataset was scanned and first a SAFT image is shown in Figure 6.2(b), demonstrating what kind of image may be expected.

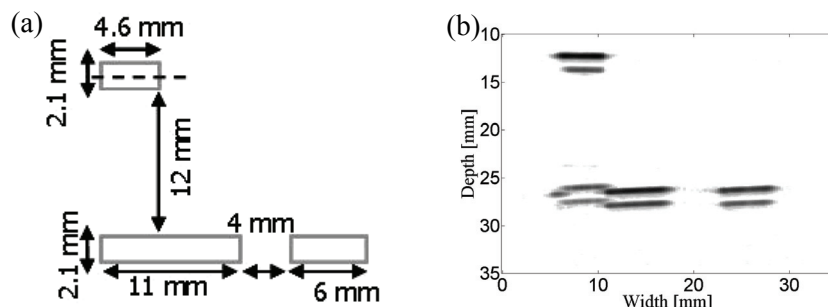


Figure 6.2. (a) Cross-section of the setup with three thin plastic plates. The probe was placed at zero depth, oriented downwards. (b) SAFT image using a PE dataset.

Next, the same PE data was used in four different SAFT methods. By this approach we test the imaging performance while using the same dataset as a reference. The performance could be compared more sensitively by plotting the maximum pixel intensities along the dashed line that is indicated through the top plastic object in Figure 6.2(a). That pixel line is shown in Figure 6.3. The standard time-domain SAFT method produced blurring at the edges of the plastic object at an amplitude level of -12 dB (line 1). The same scene was processed using CF-weighting to the standard SAFT image (line 2), which effectively improved the sharpness of the edges. Subsequently, the standard SAFT image was processed using GCF-weighting, which further suppressed the lobe at the left side of the object by another 10 dB (line 3). Moreover, the background noise in the GCF-weighted image is lowered by more than 10 dB compared to the CF-weighted image. The standard SAFT image with optimized weighting was judged as giving the best image quality because it further enhanced the SNR in the image by yet another 10 dB (line 4). This optimal weighting algorithm effectively restricts the aperture angles from the sensor array, which it is achieved by giving less weight to waves propagating under largely inclined angles with respect to the object surface (Eq. 4.8). Such inclined waves are associated with stronger surface scattering at object surfaces, which causes phases to be less coherent and produces relatively stronger noise or artefacts. Although the optimized weighting method demonstrated the best sharpness in this test case, the optimum must be tuned to each situation and the algorithm is therefore not as flexible as CF or GCF.

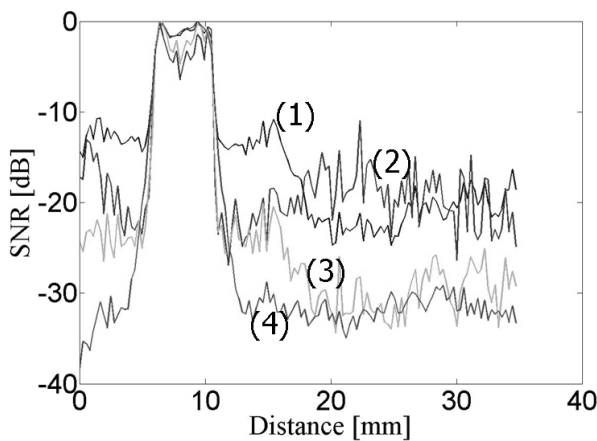


Figure 6.3. Pixel intensities in a SAFT image reconstruction of a 4.6 mm wide plastic reflector. Different weighting methods were applied in the SAFT method. Line (1): no weighting. Line (2): CF weighting. Line (3): GCF weighting. Line (4): Optimized weighting.

Next, we investigate how image sharpness may be improved by using different datasets with the same imaging method. Figure 6.4 shows the projected point-spread function of the plastic object in Figure 6.2(a), as produced by Stolt migration. The Stolt method, when using PE data, blurred the plastic object edges at -20 dB (line 1). This blur was effectively suppressed when using a PW dataset (line 2), at the cost of 140 times more computation time. For PE data, the Stolt imaging could be efficiently performed by using half the propagation wave velocity as shown in Section 5.5. However, for PW data one should compensate for the time-delay from the transmitter to the reflector. This means that in addition to the Stolt mapping, extrapolation should be used in a line-by-line approach to remove the transmitter time-delay for each corresponding imaging depth which consequently increases the computation effort. The sharpness could be improved even further with the PW dataset by suppressing the causally unrelated data during line-by-line image forming (line 3). This improvement comes at the cost of another factor 4 increase in computational effort. The sharpness produced by the PW dataset may be attributed to the effectively wider range of viewing angles during receiving, which clearly enhances the sensitivity for surface details.

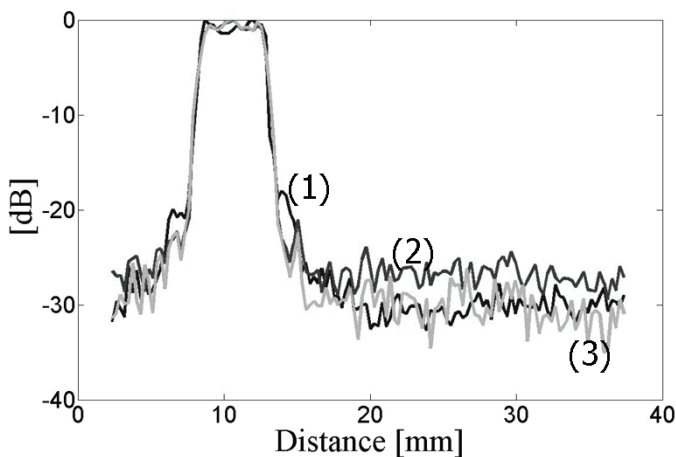


Figure 6.4. Pixel intensities in a Stolt image reconstruction of a 4.6 mm wide plastic reflector. Different datasets were applied. Line (1): PE dataset. Line (2): PW dataset. Line (3): PW dataset and improved Stolt method (line by line imaging).

6.2.2. Spectral content of a dataset

The sharpness and resolution in an image are known to be affected by the centre frequency and the bandwidth of the data. In a direct and practical approach, different probes operating at different frequencies and bandwidths may be used to collect datasets and judge the image quality. A much more efficient approach is to

use a single probe and employ only pre-defined frequency components in the image forming process. This allows the imaging to be carried out in a selected frequency sub-range within the effective frequency range of the probe. In the present setup, the transmitters were excited with a rectangular pulse of 100 ns that produced a bandwidth (-6dB) of 2-7 MHz in the received data.

In the first test case, Stolt migration was selected as a representative imaging method to reveal the performance of spectral sub-range imaging. First, an image was formed using the full bandwidth in Figure 6.5(a). Next, the centre frequency (5 MHz) was kept the same but the bandwidth was reduced to the narrow range of 4.5-5.5 MHz, the result of which is shown in Figure 6.5(b). The reduction in bandwidth caused a loss of sharpness in the image. Moreover, so-called ‘ringing’ occurs, i.e. wavy patterns near object boundaries, which is typical for band-limited imaging. It may be concluded that increasing the bandwidth will generally improve image sharpness and resolution.

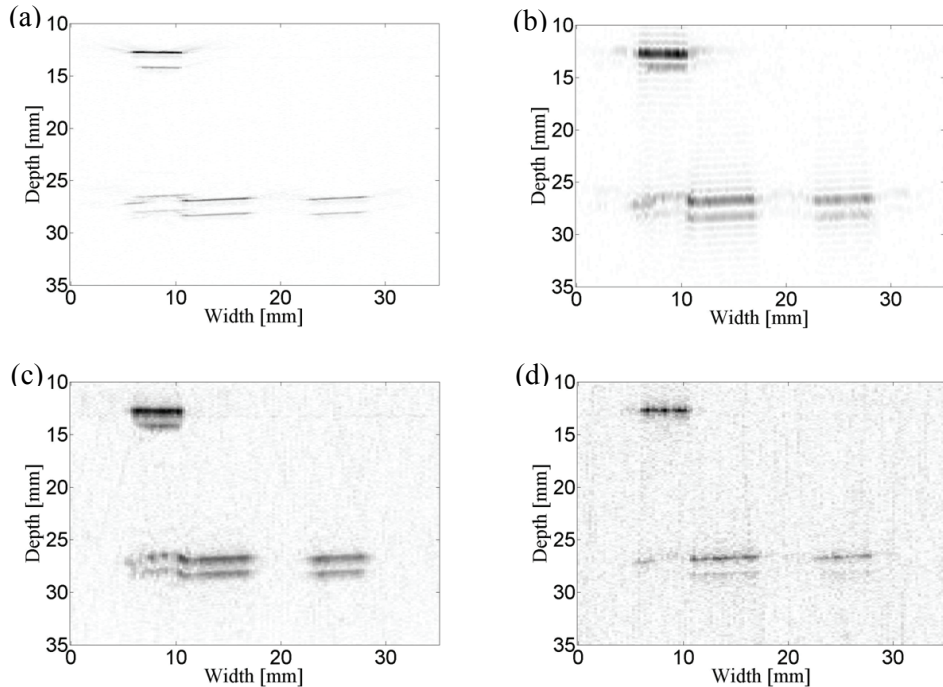


Figure 6.5. Stolt images of the plastic objects using different frequencies available from a PE dataset. The probe was placed at zero depth, oriented downwards. (a) Full bandwidth. (b) Bandwidth 4.5-5.5 MHz. (c) Bandwidth 0.5-3 MHz. (d) Bandwidth 7-10 MHz.

The effects of a different centre frequency were studied in the following two test cases. Distinctly different frequency ranges are used, but the bandwidths are kept practically the same. Figure 6.5(c) shows the image of the plastic object for the bandwidth 0.5-3 MHz. The front and back surface of both the upper and the lower plate are present and well visible, i.e. the image shows a good contrast. If the frequency range of 7-10 MHz is used instead for the image in Figure 6.5(d), the front surface indications are sharper by which the width of the plastic object can be estimated with higher accuracy, i.e. it shows a better shape consistency. On the other hand the image shows less contrast, in particular the back surface appears weaker and locally a part of the lower plate (underneath the upper plate) has disappeared. The local loss of contrast is due to acoustic absorption in the upper plastic plate, which increases rapidly with increasing frequency.

The general loss of contrast in Figures 6.5(c) and 6.5(d) when compared to Figures 6.5(a) and 6.5(b) is that the used frequency ranges were mostly outside the main bandwidth of data. Concluding, higher ultrasound frequencies (smaller wavelengths) may increase the resolution and sharpness, but the used frequencies should eventually be set to a range where the contrast remains acceptable. This finding links to the analysis in Section 3.7.3, which discusses the minimum signal strength required for imaging overlapping particles as function of particle type and thickness.

In the same scenario as for Figure 6.5, the spectrum dependent imaging performance was investigated using a space time-domain imaging method, in this case time-domain frequency SAFT (cf. Section 4.5.3). Figure 6.6 shows that the results are very comparable to the Stolt method, since the best space-time domain imaging performance is also achieved when using the full bandwidth.

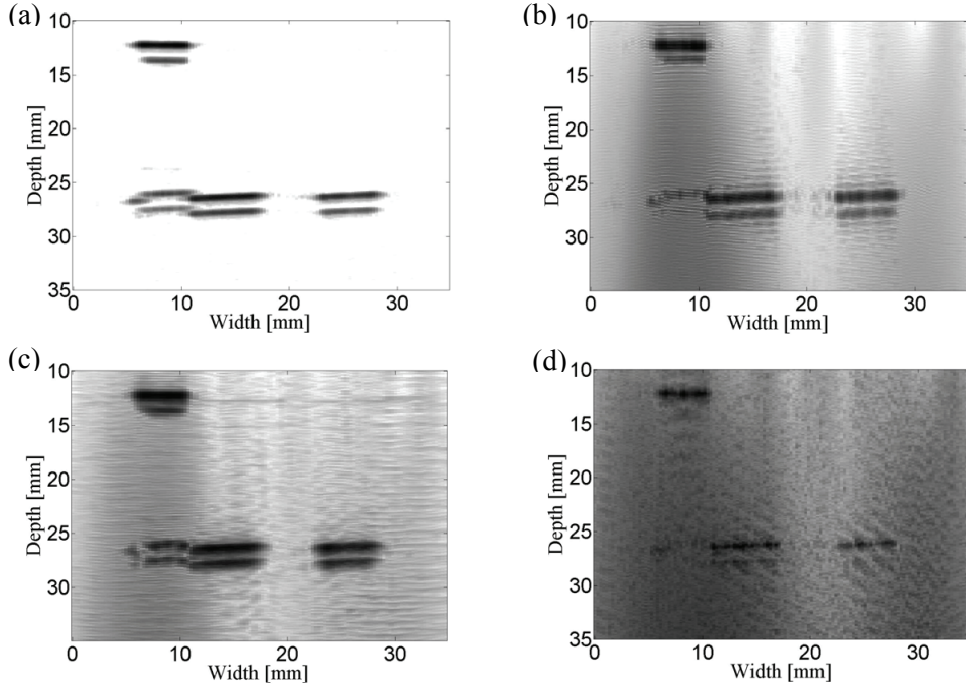


Figure 6.6. Time domain SAFT images of the plastic objects using different bandwidths available from a PE dataset. The probe was placed at zero depth, oriented downwards. (a) Full bandwidth. (b) Bandwidth 4.5-5.5 MHz. (c) Bandwidth 0.5-3 MHz. (d) Bandwidth 7-10 MHz.

6.3. Particle cross-section imaging

6.3.1. Imaging test objects

The feasibility of visualizing the cross-section size and shape of a particle is investigated using three representative test objects. These objects are shown in Figure 6.7. To that end, both the front and the back surface of the objects are to be imaged. The results validate the functionality of imaging methods for this purpose, though they will also show that shape consistent reconstruction requires acoustical information to be present in the dataset. That information relates to recorded reflected waves from the surfaces in question, which may be either related to ideal reflection or surface scattering. The implications of this requirement will be investigated in Section 6.3.2.

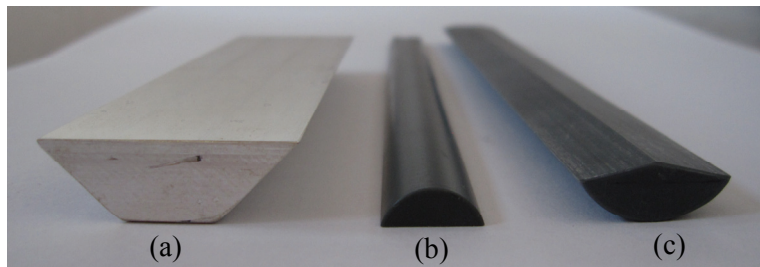


Figure 6.7. Test objects used for cross-section imaging. (a) Aluminium test object. (b) Generic polymer test object. (c) Polymer test object.

Aluminium test object:

An aluminium test object is used to investigate the main principles of cross-section imaging. A metal is selected as it leads to conservative imaging conditions, which relates to a scattering object with a much higher acoustic impedance and wave velocity than ferrofluid. This means that any assumption on similarity in wave velocity, such as employed in single velocity imaging methods, or smoothness of horizontal wave velocity variation, such as in NSPS (cf. Section 5.8) is really put to the test. The cross-section dimension of the smooth aluminium object is shown in Figure 6.8(a). It has an out-of-plane length 37 mm to allow simulation of a 2D cross section. The object is plane on one side and the other side is shaped like a trapezium. The 2D cross section observed in imaging is then thought to consist of water (pressure wave velocity 1480 m/s) and aluminium (compressional wave velocity 6400 m/s). Behind the back surface of the test object was of course also a layer of water, but this was deep enough so as not to contribute any reflected waves within the time frame in which the data were collected.

Polymer test object:

The MDS applicability of the imaging methods is first investigated using the PVC object in Figure 6.9(a), which out-of-plane length was 80 mm to simulate a 2D situation. The object is caret-shaped on one side and the other side is round. The 2D cross section then thought to consist of a layer of water and a layer of polymer (compressional wave velocity 2341 m/s) and at the bottom a deep layer of water.

Generic polymer test object:

A second PVC object with a generic shape is used to further test the imaging performance, as it closer represents different shapes of waste particles. Shredded plastic waste particles may show a wide variation in shape, but the relevant issue for acoustic data collection is that acoustic waves may be incident on the particle

surface under every possible angle. A possible approach to study the consequences for imaging performance would be to rely on statistics, imaging several hundreds or even thousands of ‘real’ waste particles. Instead, the polymer test object in Figure 6.12(a) is used (again with an out-of-plane length 80 mm), which has a rounded side and a flat side that may represent all possible reflection and refraction angles occurring for shredded consumer waste particles. Those waste particles tend to be either (locally) flat, as in flakes, or (locally) rounded, which occurs more commonly for thicker shredded plastics. Specifically, using this generic test object we will demonstrate the possibilities for cross-section imaging. The 2D cross section is then thought to consist of water and polymer (compressional wave velocity 2341 m/s, shear wave velocity 1060 m/s). At the bottom is again a deep layer of water.

6.3.2. Principles of cross-section imaging

As a first case, the plane surface of the aluminium object in Figure 6.8(a) was turned upwards to face the sensor array in a symmetrical position and a PE dataset was collected. Figure 6.8(b) shows the image using the Stolt method. The plane front surface is accurately reconstructed but the back surface is distorted since the compression waves reflected from the non-plane back surface are interpreted wrongly. The underlying cause is that the compressional wave velocity of aluminium is quite different from water and, since the Stolt imaging can only employ the wave velocity of water, the method reconstructs the back surface reflections at the wrong position. This makes it impossible to accurately determine the cross section shape and thickness of the object with the Stolt method.

The same PE dataset was processed using phase shift migration in Figure 6.8(c). This method produces a much better shape consistent cross section and, moreover, the size of the cross section is also accurate. It is noted that, in this particular object position, the acoustic information from the sloping parts of the back surface is dominantly related to wave scattering since the steep 45° angles easily cause critical wave reflection. Since the aluminium was milled to make it smooth, this indicates that scattering already occurs when the material surface has an average roughness of several micrometers. Figure 6.8(c) shows that phase-shift migration can focus these scattered waves at the back surface, allowing for shape consistent cross-section imaging. During image forming, the amplitudes of the back-surface scattered waves were enhanced to compensate for the transmission losses at the aluminium-water interface. This so-called ‘amplitude compensation’ improves the contrast of the back surface with respect to the much higher contrast of the reconstructed front surface. This correction is common practice in medical imaging, where the human operator tries to maintain the image quality using either the TGC controls or logarithmic compression tools (cf. Section 2.2.2). Some artefacts may be observed in Figure 6.8(c), but even for the less skilled person these will have little bearing on the correct interpretation of the image.

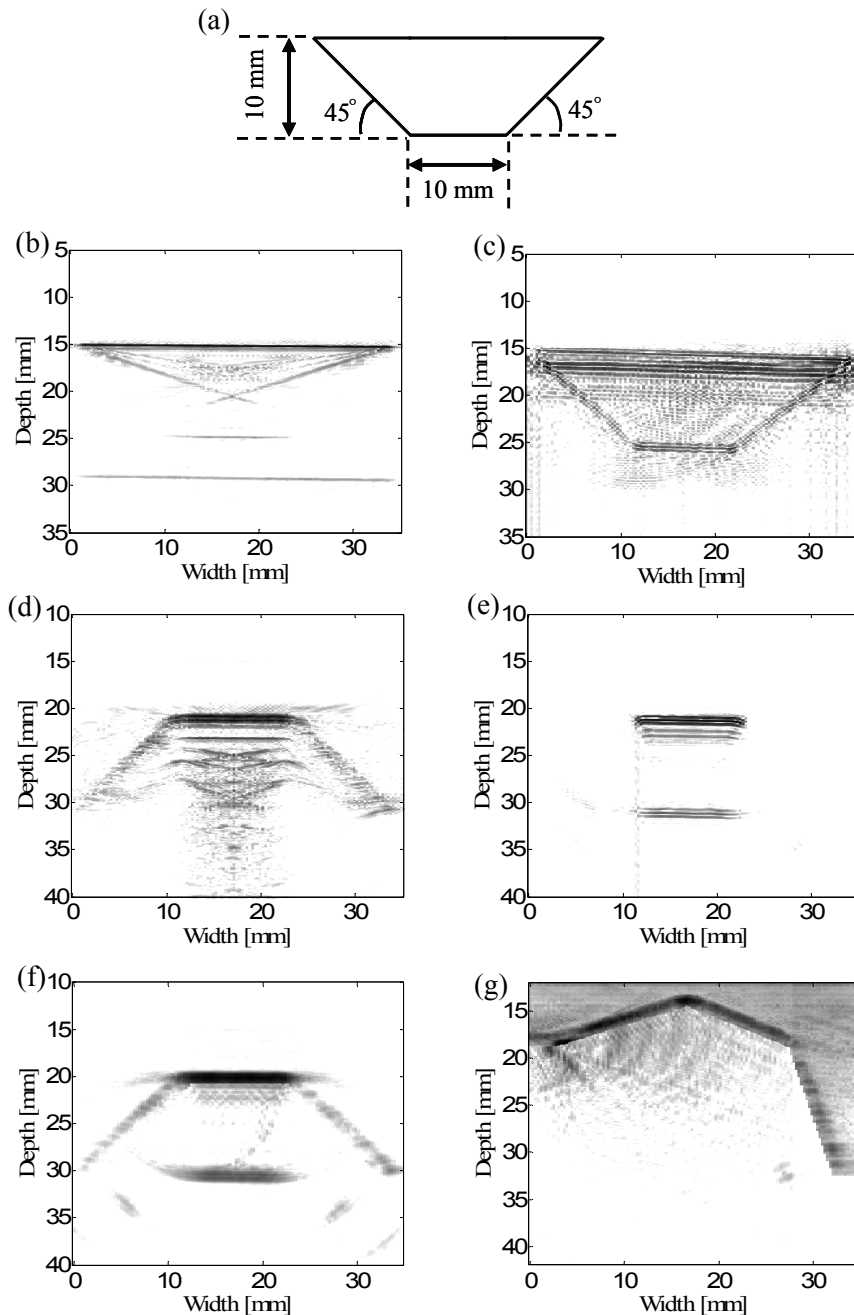


Figure 6.8. (a) Cross section of the aluminium test object using PE data. The probe was placed at zero depth and oriented downwards. (b) Stolt: plane surface upwards. (c) Phase-shift migration: plane surface upwards. (d) Stolt: trapezium surface upwards. (e) Phase-shift migration: trapezium surface upwards. (f) Redatuming and SAFT: trapezium surface upwards. (g) Redatuming and SAFT: trapezium surface upwards, rotated under 23°.

As a second test case the aluminium object was flipped upside down so the trapezium surface faced the sensor probe. A PE dataset was collected and the Stolt image is shown in Figure 6.8(d). It is observed that here the top trapezium surface is reconstructed correctly, which was expected because of the direct water path between the object and the probe. Note that also here the 45° sloping parts are reconstructed thanks to surface scattering. However, the back surface is again distorted into a few artefacts.

The same PE dataset was also processed using phase-shift migration. For that purpose the top of the aluminium object provided the reference depth for the artificial divisional plane between the water and aluminium layer, as required for this method. The image is shown in Figure 6.8(e). When comparing with Figure 6.8(d), it is observed that only the horizontal parts of the object cross section are present and correct. The reason is that only the plane top part coincided with the artificial divisional plane to where the redatuming took place, and the top surface scattered waves could not successfully contribute to the front surface reconstruction. This case demonstrates that, as long as the object in question has a reasonably plane and parallel front surface part facing the probe, that part will offer a ‘keyhole view’ into the object and phase-shift migration will at least yield a partially correct cross-section image of the particle.

As a next test case, the same PE dataset was processed by the combination of SAFT and redatuming, where the back surface was reconstructed using the redatumed data along the front surface of the object. The result is shown in Figure 6.8(f). The combination of redatuming and SAFT correctly reconstructed the trapezium front surface, but it did not succeed in reconstructing the whole back surface. This is caused by critical angle reflection at the 45° front surface slopes, by which the underlying parts of the plane back surface remained shielded and, apparently, the PE set did not contain any relevant information.

As a last test case with the aluminium object it was rotated by 23°, so that the sloped left-side is exposed to the probe under a less sharp angle. A PE dataset was collected and processed using the same hybrid approach of SAFT and line-by-line redatuming. The image in Figure 6.8(g) shows that the front surface is correct with a good contrast, despite the steep angle of the right slope. However, the plane back surface is now completely missing due to critical angle shielding.

A possible improvement for the back surface reconstruction in this particular object position could be to apply more accurate sloped redatuming (cf. Section 5.3.2) to each of the three plane parts of the front surface before applying SAFT. However, the success would still depend on the presence of surface scattering information in the PE dataset. But judging from the complete absence of any back surface indication in Figure 6.8(g), it is rather doubtful there is any such information in this dataset.

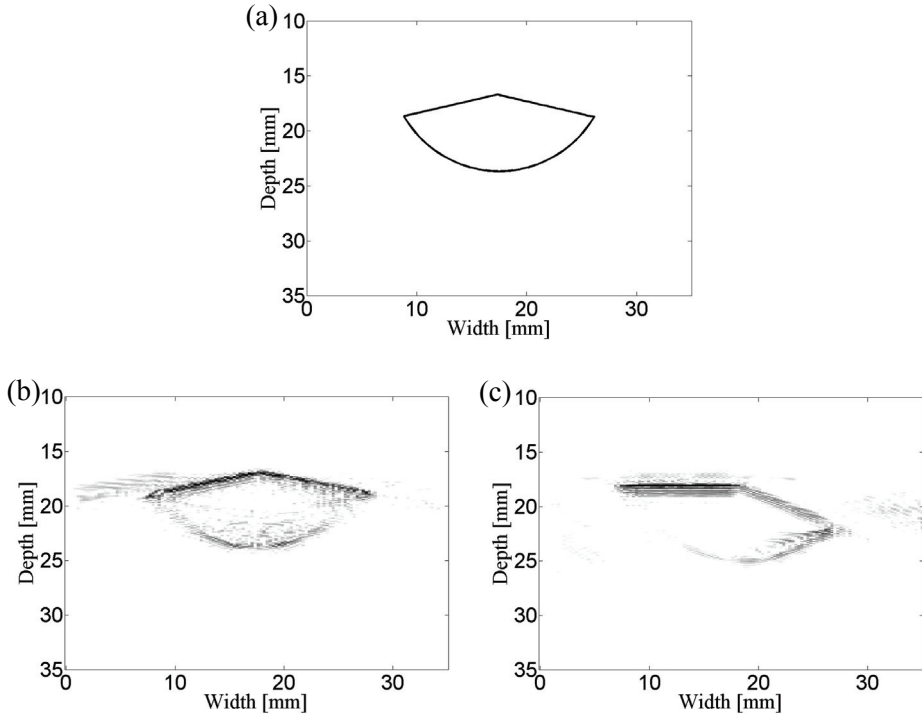


Figure 6.9. (a) Cross section of a caret-shaped PVC object using NSPS migration. The sensor probe was placed at zero depth, oriented downwards. (b) Triangular surface upwards. (c) Triangular surface upwards, rotated at an angle.

6.3.3. Acoustic information and signal strength

We start with the polymer test object which caret-shaped side was turned upwards to face the probe, as shown in Figure 6.9(a). A PE dataset was scanned and processed using NSPS migration to deliver the image in Figure 6.9(b). The cross section shape is quite shape consistent, but the outer parts of the back surface are missing due to critical angle shielding. This may be confirmed by rotating the object to expose one of the edges in a different way to the probe. In this case the object was rotated 12° clockwise and the resulting image for the new PE data is shown in Figure 6.9(c). Clearly, the right part of the back surface now shows a better contrast but more of the left part is missing. This shows that back surface information in the PE scan has increased for the right part at the cost of the left part, which must be due to critical angle shielding.

The test case of Figure 6.9 shows that a condition for correct imaging of a cross section is availability of acoustic information from both the front and back surfaces. To that end, the data should ideally contain acoustic waves which were directly (not multiply) reflected or scattered from every part of the surface in

question, since these are most useful for imaging purposes. In general, the acoustic data will consist of waves which followed different wave paths and were associated with possibly different modes of wave propagation, i.e. compression-mode or shear-mode. Surface skimming waves, which may arise at the particle-water interface, may be shown to involve a combination of shear- and compression-type deformations. The surface skimming waves may in turn radiate their energy as pressure waves, but these types of wave are as yet of little use for imaging.

To closer investigate the acoustic information in a dataset we examine the generic plastic object of Figure 6.12(a) with its rounded side facing the probe. Figures 6.10(a) and 6.10(b) show the B-scan of a PE and PW dataset, respectively. The SNR in the PW data was 40dB and in the PE data 60 dB, since the PE data was produced by averaging 100 measurements for each sensor element.

A straightforward ray-tracing algorithm, based on Snell's law and plane wave reflection and transmission coefficients (cf. Section 3.7.3), was employed to help identify the different types of wave in the datasets, especially those related to the back surface. The rays taken into account are primary rays, i.e. wave paths with just one reflection and involving at most one mode conversion upon either transmission or reflection at an interface. This family of rays proved sufficient to explain all the significantly energetic waves found in the data. Each identified ray was counted as a 'hit' for a specific small part (point) of the back surface. The relative energy of a ray was estimated using the two plane-wave transmission coefficients at the front surface and the reflection coefficient at the back surface of the object.

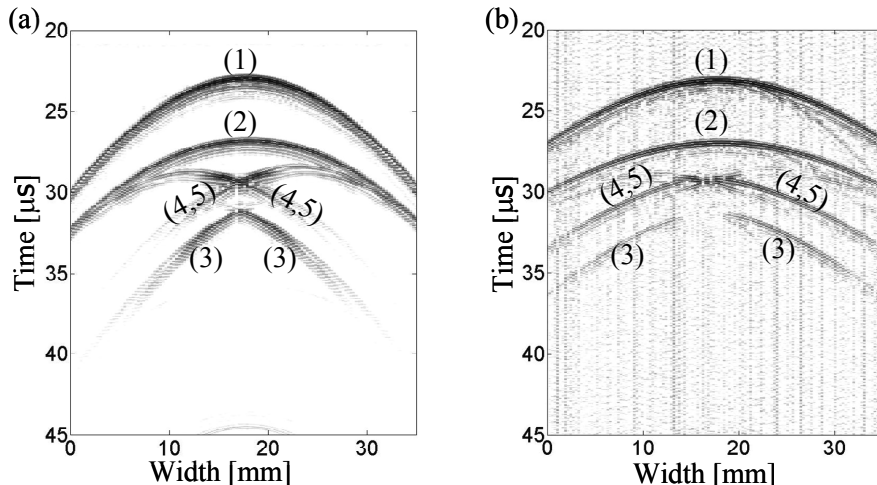


Figure 6.10. Different wave types in a B-scan of the generic plastic test object in Figure 6.12(a). Using ray-tracing the identified waves are: (1) PP, (2) PCCP, (3) PSSP, (4) PCSP and (5) PSCP. (a) PE data. (b) PW data.

Five dominant types of wave could be identified according to the successive modes of the ray paths to the particle and back to the probe. The modes are water pressure waves (P), solid compression waves (C) and shear waves (S). The rays labelled (1)-(5) in Figure 6.10(a) and 6.10(b) are: PP (1), PCCP (2), PSSP (3), PCSP (4) and PSCP (5). For a PE dataset, the average hit-rate for PCCP and PSSP waves along the plane back surface were 1 and 2, respectively. Both hit-rates were zero near the corners of the test object due to critical reflection at the rounded front surface. This means that critical reflection shielded the back surface from being irradiated by either compression waves or shear waves. Therefore, the rays covered 89% (PCCP) and 67% (PSSP) of the particle's back surface. The hit-rates for PCCP and PSSP rays increased in the PW dataset to 2 and 4, respectively, thanks to the larger synthetic receiving aperture in this type of scan. However, in the PW dataset the rays covered only 67% (PCCP) and 58% (PSSP) of the particle's back surface, indicating the particle's cross section could only be partially reconstructed, no matter which dataset or imaging method would be used.

The amplitude for PCCP waves in PE data varied 2 dB (cf. Figure 6.11(a)), while it varied up to 90 dB for the PSSP waves (cf. Figure 6.11(b)). Similar large differences were observed for a PW dataset (cf. Figures 6.11(c) and 6.11(d)). Note there is practically no reflected energy at the centre of the back surface for PSSP waves, since the compression waves are transmitted at the normal angle to the front surface, which excludes mode conversion. Therefore, even though PSSP waves have relatively higher hit-rates, they mostly carry little energy. Moreover, as shown by Figures 6.11(b) and 6.11(d), the strongest PSSP waves are quite localized and therefore do not carry information by which the whole back surface could be reconstructed. The mode-converted waves 4 and 5 were weak compared to the PSSP waves and also carried only partial information about the back surface (cf. Figures 6.11(e) and 6.11(f)). Therefore, it must be concluded that only PCCP rays, and perhaps also the PSSP rays, are suitable for reliable cross section imaging. This finding will be put to the test in the next subsections. It is noted that essentially the same conclusion applies when the plane side of the test object in Figure 6.12(a) would face the probe.

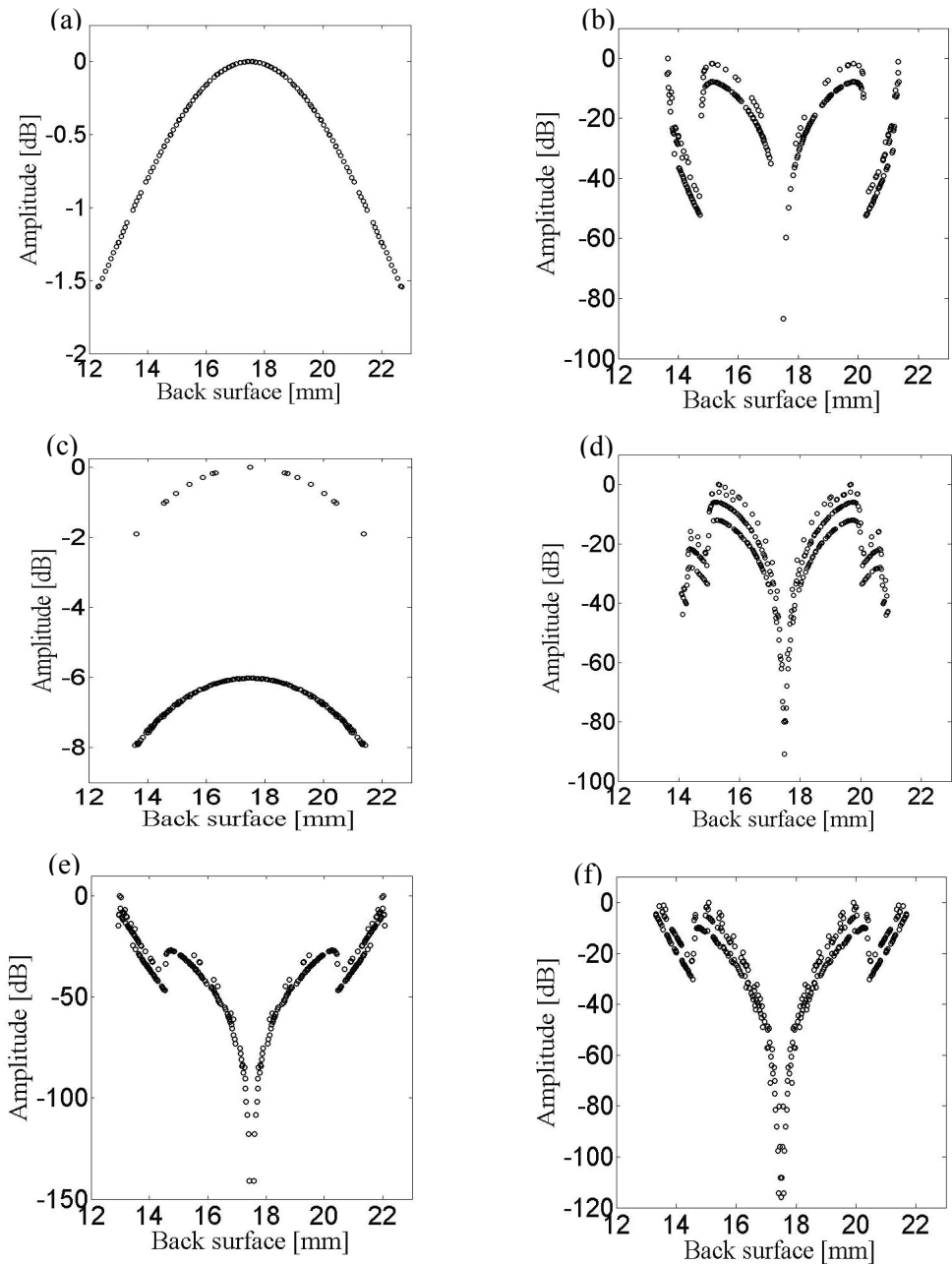


Figure 6.11. Amplitude distribution of wave types for different datasets for the generic plastic test object in Figure 6.12(a). (a) PCCP rays in a PE dataset. (b) PSSP rays in a PE dataset. (c) PCCP rays in a PW dataset. (d) PSSP rays in a PW dataset. (e) PCSP rays in a PE dataset. (f) PCSP rays in a PW dataset.

6.3.4. Cross-section imaging performance

Generic test object case: Rounded side up, PCCP imaging

The rounded side of the polymer object in Figure 6.12(a) faced the probe and PE and PW datasets were collected. Using the PE data, Figure 6.12(b) shows the image using a hybrid imaging approach. The front surface is reconstructed in a SAFT algorithm by virtue of the PP waves. Only the horizontal middle part of the rounded front surface shows up correctly, since elsewhere the waves reflected under critical angles and are missing in the PE data. For the back surface the PCCP waves were employed in a combination of redatuming and SAFT, where the reconstructed back surface is scaled up by 30 dB to compensate for the additional transmission losses of waves entering and leaving the object. The plane back surface in Figure 6.12(b) comes out rather curved towards the edges, which is because there is no data available from these edges. In other words, critical reflection shields these parts of the back surface.

Figure 6.12(c) shows the image using the PW data. The front and back surface reconstructions are quite comparable to that one in Figure 6.12(b) but the artefacts are slightly different. The higher number of hit-rates (cf. Section 6.3.2) has contributed to reducing the background noise by 3 dB within the particle cross section, which improved image contrast.

The same PE and PW datasets were also processed using the NSPS method in Figures 6.12(d) and 6.12(e), respectively. The PE dataset produces a somewhat better reconstruction of the cross section compared to the redatuming method in 6.12(b). The reason is that redatuming is based on a mapping of the detected wave field to new, virtual receiving positions on the object front surface. Since this is done in a horizontal line-by-line approach, a part of these mapped waves were propagated through the plastic to reach that new position. Since this involved an inhomogeneous ray path that wave field redatuming does not account for, it produced artefacts in the image. The NSPS method is better suited to handle this. To that end, the ROI was divided into many vertical sublayers (100 μm wide), where each layer consists of water and/or plastic media. The back propagation is performed for both wave speeds in each layer, while the procedure is repeated recursively for the whole ROI. Noting the slight blurring of the particle front surface in Figure 6.12(d), the PW dataset is used with the NSPSP method to produce the image in Figure 6.12(e), which shows different artefacts. The blurring of the particle front surface is better suppressed thanks to the broader receiving aperture of PW data. This suggests that a combination of both datasets could improve overall image quality.

The curving of the object edges in the reconstructions of Figures 6.12(b) to (e) is a typical imaging artefact, caused by a lack of acoustic information on those parts of the object. This may be significantly improved by employing a wider scanning aperture, for example by adding data scanned with a probe under a different viewing angle with respect to the particle. To investigate the potential of

this idea, the probe was rotated 20° anticlockwise by which it better irradiated the left edge of the object. A PE dataset was scanned and processed using the NSPS method in Figure 6.12(f). The left side, both the front and back surface, is reconstructed more accurately and the curving artefact is effectively suppressed. The consequence of this viewing angle is a loss of contrast at the right side of the object reconstruction. To get an overall improved reconstruction of the cross section the images from at least two different viewing angles may be compounded. It is concluded that the main limitation for obtaining a complete and accurate reconstruction of the object cross-section is the amount of information in the datasets, and that in principle the imaging methods are capable of rendering a shape-consistent image.

Generic test object case: Rounded side up, PSSP imaging

In Figures 6.12(a)-(f) PCCP waves were used to reconstruct the back surface. The consequence is that other wave modes are imaged out of focus and, at most, could only contribute artefacts. This is the case for the so called *leakage artefacts*, which may be observed in Figures 6.12(b)-(f) as a smearing below the reconstructed front and back surfaces. The effect may be demonstrated by checking the present leakage of the PSSP waves below the reconstructed back surface. In order to turn the artefact into a contribution to the image contrast, the PSSP waves should be focused by imaging with the relevant shear wave velocity. To this end all waves in the data except the PSSP and PP waves (cf. 1 and 3 in Figure 6.10) were filtered from the datasets except where they overlapped with the two target wave types. The PP waves were included so the front surface reconstruction provides a spatial reference.

The NSPS method produced Figure 6.12(g) using PE data and Figure 6.12(h) using PW data. Observable is that only two symmetrically positioned small parts of the flat back surface at 22 mm depth are reconstructed using the shear waves. This corresponds to what the ray-tracing procedure predicted for the distribution of reflected wave energy in Figures 6.11(b) and 6.11(d).

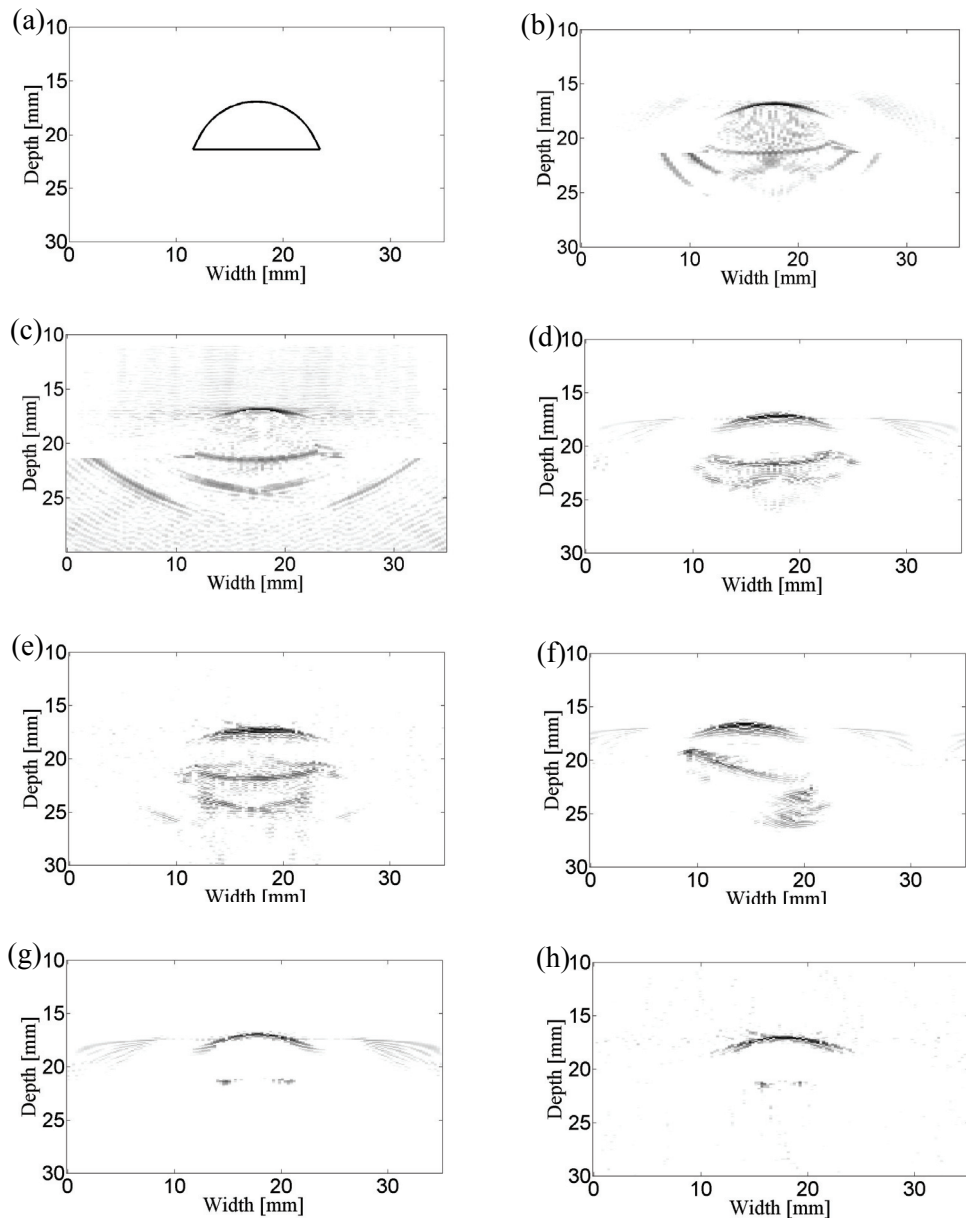


Figure 6.12. (a) Cross section of the generic PVC object with the rounded side facing the probe, placed at zero depth, facing downwards. (b) PE data; redatuming and SAFT with PCCP (back) and PP waves (front). (c) PW data; redatuming and SAFT with PCCP (back) and PP waves (front). (d) PE data; NSPS with PCCP (back) and PP waves (front). (e) PW dataset; NSPS with PCCP (back) and PP waves (front). (f) Probe rotated under 20° , PE data; NSPS with PCCP (back) and PP waves (front). (g) PE data; NSPS with PSSP (back) and PP waves (front). (h) PW data; NSPS with PSSP (back) and PP waves (front).

Generic test object case: Flat surface up, PCCP imaging

The flat side of the object faced the probe and PE and PW data were collected. Wave redatuming and SAFT was used to produce the images in Figure 6.13(a) (PE data) and Figure 6.13(b) (PW data). The back surface reconstruction in Figure 6.13(a) is a perfectly half circle, but the radius is small and it is not the true shape of the back surface. The cause is that after redatuming the only PE data left of the back surface proved to be concentrated in one virtual sensor in the centre of the front surface. In other words, practically only the centre point of the back surface contributed to the physical PE data (and has a nonzero hit rate in ray-tracing terms). In this exceptional case of lacking data, non-uniqueness dictated that a perfect half-circle can be reconstructed the size of the distance from the virtual sensor to the back surface, since all over this half-circle the imaging condition is perfectly fulfilled for the only available sensor signal. This peculiar test result may be attributed to the space-time SAFT principle; it tests systematically all the positions in the ROI for a constructive focussing effect, which is principally different from F-SAFT.

The PW data in Figure 6.13(a) performs better in the sense that it at least provides sufficient information to prevent the perfect circle, i.e. the back-surface data still forms a small hyperbolic curve in the B-scan after redatuming. However, the information is still too little to enable reconstruction of a larger part of the back surface.

The same PE and PW datasets were also processed using phase-shift migration. It is noted that the flat top surface of the test object provided the reference depth for the artificial divisional plane between the two layers (i.e. water and plastic) that is required for this method. The images are shown in Figures 6.13(c) and 6.13(d). The FSAFT imaging in phase-shift migration could not improve the time-SAFT result where it concerns PW data, but at least for the PE data it does not result in the peculiar semi-circle, thanks to the back propagation principle. Instead, the solely available PE data from the centre of the back surface has been smeared out in the image to a sort of line which coincidentally runs in the direction of the true curving of the back surface, which is a general indication of a lack of information in the data.

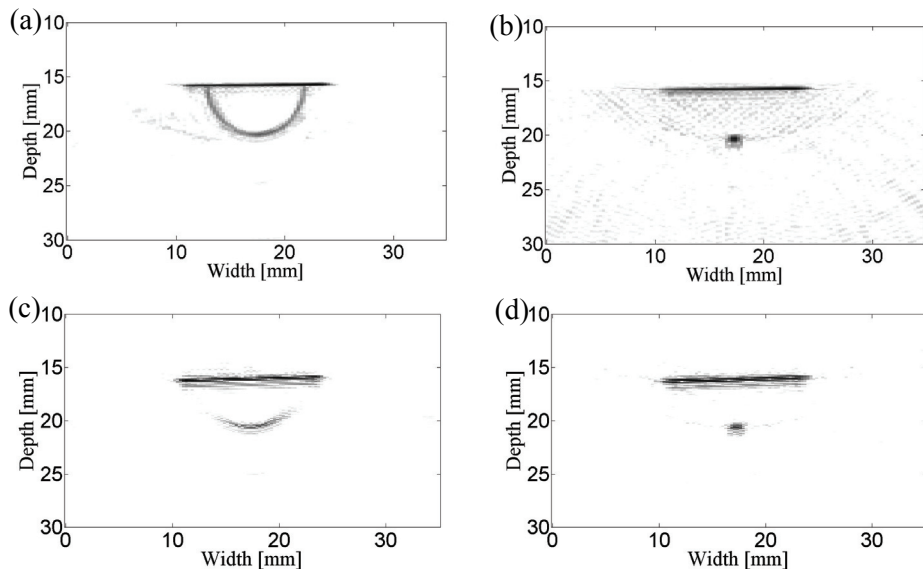


Figure 6.13. Ultrasound images of the generic test object with the flat side facing the probe. The probe was placed at zero depth, facing downwards. (a) PE dataset; redatuming and SAFT. (b) PW dataset; redatuming and SAFT. (c) PE dataset and phase shift migration. (d) PW dataset and phase shift migration.

6.4. Evaluation and recommendation for MDS applications

From the family of the primary rays, including the ones with at most one mode conversion, it proved that only the pressure-compression rays (PCCP) carried sufficient information and signal strength to allow for complete and accurate cross-section imaging. The pressure-shear rays (PSSP) provided at best only partial reconstruction of the back surface.

In principle, all the demonstrated imaging methods were capable of giving a good shape consistency for the front surface. For a PE dataset, phase shift or NSPS migration techniques gave the best performance, especially if the front surface is plain. With a PW dataset the phase-shift, NSPS migration and hybrid SAFT-redatuming techniques showed a similar performance.

However, due to critical angle shielding and the related missing information in the datasets, none of the imaging methods proved capable of always providing a reliable cross-section image. It should be emphasized that this was not a drawback of any method, but a physical limitation imposed by the setup and method of scanning data. For example, it proved that by rotating the probe to a different viewing angle on the test object the desired acoustic information could be collected in the data. This finding has led to the recommendation for an improved MDS data acquisition strategy, which is to use at least two probe views and

compound their images. Since the MDS channel is not suitable for quickly moving or rotating probes, the economical option appears to be a combination of just two linear arrays placed under a fixed angle, as depicted in Figure 6.14. These two viewing angles could lift to a large degree the physical data scanning limitations of the single probe. Using this option does require the two images to be compounded, which requires basically a rotation of the image pixels to a common coordinate system. Another interesting feature of this setup is that it may be employed to produce transmission data, which could be utilized in methods for advanced materials identification.

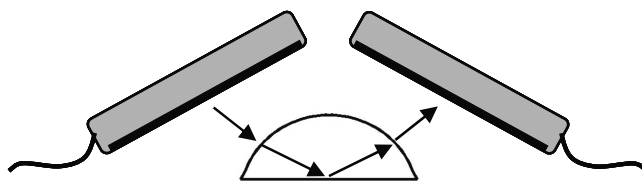


Figure 6.14. A combination of two probes with different viewing angles overcome much of the critical angle shielding and, in addition, may provide transmission data for advanced materials identification techniques.

6.5. Statistics in online quantitative ultrasound

The research in this chapter was focused on imaging of a single particle in a static scene and then accurately reconstructing its cross-sectional shape and surface area. However, the future purpose of the ultrasound method is to serve as a real-time quantitative tool for measurements on a stream of particles in an industrial version of the MDS. Due to the limited width of the sensor array, its application will be necessarily restricted to the detection and measurement of a representative sample from the particles stream, i.e. a limited number of particles can be detected spatially and per unit of time. To assess the accuracy of a quantitative measurement it is required to quantify all the errors. This requires some statistical theory, which is demonstrated here assuming the objective is to measure per unit of time the average volume (m^3/s) of particles in the MDS. The following assumptions apply:

- The probe is placed inside the MDS channel in positions 1a or 1b as depicted in Figure 2.14, to have a cross-section view of the moving particles;
- Each time interval Δt a sample consisting of N particles can be measured;
- Using imaging, the cross-section A of each particle is measured;
- The average length l of the particles in the direction of the flow is known apriori from the statistics of the plastics waste heap.

Imaging accuracy: The cumulative volume of a sample of N particles is determined as:

$$V_{\text{measurement}} = \sum_{n=1}^N l(A_n + \Delta A) = V_{\text{sample}} + l\sqrt{N}\sigma_{\text{imaging}}. \quad \text{Eq. (6.1)}$$

Here, V_{sample} is the real volume of all the N particles, A_n is the measurement of the cross-section of a particle using imaging and ΔA is the error made in the imaging, complying with a normal distribution with standard deviation σ . Eq. (6.1) shows that for a cumulative measurement the error increases by the square root of the sample size. This error may be reduced by averaging over M different samples, according to

$$V_{\text{measurement}} = (1/M) \sum_{m=1}^M \sum_{n=1}^N l(A_n + \Delta A) = \bar{V}_{\text{sample}} + l\sqrt{N/M}\sigma_{\text{imaging}}. \quad \text{Eq. (6.2)}$$

Here, \bar{V}_{sample} is the average volume of all the particles in the M samples. This way the quantitative imaging system delivers an accurate average sample volume each time interval $M\Delta t$. This result shows that a higher imaging accuracy allows for faster measurements, since there is less need to improve accuracy by averaging over subsequent samples.

Sampling error: Even if perfect measurements are performed on a limited sample of N particles, randomly taken from a larger particles stream, the measurements for many of such equal sized samples from the same stream will vary among the samples. This is called the sampling error. It should be emphasized that the sampling error is not related to natural variations in particle properties, but is related to the chance that certain types of particle end up in the sample. Different scenarios may arise for the MDS channel.

If the probe, which is in channel cross-section view, measures the surface area of all the particles that flow through the channel cross-section, the sampling error will be zero. Since the channel is much wider than the probe the requirement is that the channel waste particles feed is uniform along the channel width. If this is not the case, the measurement of Eq. (6.2) should be repeated along the full width of the channel. In case the image rate of the ultrasound imaging system is too low to capture all the particles flowing through the view of the probe (cf. Section 2.4.2), it means that the measurement in Eq. (6.2) is effectively applied to a subsample of the particles stream and a sampling error will occur. However, the feed rate of the MDS is necessarily limited, since a too high feed would negatively affect the MDS separation performance. Therefore, even in the extreme case it is expected that more than 25% of the stream could be sampled by an ultrasound imager. This presents a quite large sample and the sampling error is expected to be negligible. Note that increasing the sample size (N) or number of samples (M) will also further reduce any sampling error.

Chapter 7: Conclusions and recommendations

7.1. *Conclusions*

The research is dedicated to ultrasound techniques with a high potential for inline quality control in wet solid waste processing techniques, specifically magnetic density separation. The originality of the work mainly lies in the introduction and investigation of quantitative ultrasound imaging technology in the field of recycling. The main challenge was to integrate the different fields of expertise and form the multidisciplinary basis that is required for research in sensor-based recycling. Another challenge was to incorporate as close as possible the physics of acoustic wave propagation in the imaging algorithms and still maintain efficiency in visualizing plastic particles. The measurement equipment was developed around dedicated hardware and data processing software. In particular, the challenges of ultrasound data acquisition strategies and image forming techniques were investigated both theoretically and experimentally for qualitative and quantitative analyses of plastic waste particles moving in the ferrofluid filled channel of a magnetic density separator. The ultrasound system provided valuable information on the waste particles and flow profile, which may be utilized in an industrial inline system for studying flow turbulence, particle streams and quantitative types of analyses. For recycling this will contribute to the optimization and accurate control of plastic separation performance. The introduction of this multidisciplinary type of research will transform the recycling process by introduction of an intelligent, sensor-based technology to assist and safeguard product quality. This should lead to higher quality secondary plastics and a wider acceptance for reuse in high-end products.

As a departure point, state-of-the-art medical ultrasound technology was adapted to investigate the potential of ultrasound in real-time scenarios. First, from the qualitative point of view, the ultrasound system proved capable of producing good quality images of moving particles in the separation channel. In particular, shape-consistent images including detailed features up to 0.5-1 mm resolution were obtainable, provided that the probe had the favourable viewing angle towards the particle. Second, for the quantitative analysis, the capacity of the ultrasound system was theoretically characterized for different probe positions in the MDS channel. Using a linear array of 35 mm aperture, the ultrasound system had the capacity to monitor 20 – 60 particles per second. Depending on the probe view on the particle streams, a redundancy of 3 images per particle is achievable, which provides a way to track an individual particle in the ferrofluid flow.

Image processing was applied to ultrasound video-streams to produce inline the quantitative information required to evaluate MDS performance. The particle density distribution (PDD) was obtained over a 100 mm probe range from which the optimum position of product splitters in the MDS extraction unit could be determined. Data processing techniques were able to give an indication of the

convergence of the plastic streams towards their equilibrium depth as they floated towards the extraction unit. In addition, the individual particles were successfully traced in consecutive ultrasound images from which their horizontal and vertical displacements and velocities could be quantified, leading to insight into the ferrofluid flow profile and scales of turbulence.

The performance of the applied commercial medical ultrasound technology proved quite dependent on the presence of a human operator to adapt the probe viewing angles and maintain image quality. This strongly limits the usefulness of this technology for industrial plastics recycling. To maintain image quality for the moving, acoustically hard plastics in a mechanically poorly accessible separation channel will require a re-thinking of the sensor positioning, the data acquisition strategy and the desired software functionalities that are highly dependent on data quality. Moreover, retrieving a type of quantitative information like particle cross-section shape requires a different imaging method than other potential MDS applications such as monitoring and tracking of particles during separation. This has motivated the research into the different advanced ultrasound imaging methods and methods for more quantitative analysis.

To that end, the most promising imaging methods from acoustically better established fields such as geophysics, medical ultrasound diagnostics and non-destructive testing have been selected and adapted. As a major challenge for quantitative analysis, the focus was on 2D cross-section imaging of plastic particles. Optimum data acquisition strategies in combination with different imaging techniques were investigated for their performance. This demanded the introduction of suitable performance indicators to achieve an objective assessment of image quality. The ultrasound data for these tests were scanned from static scenes with a number of representatively shaped test objects. The tests showed the dependency of imaging performance on data quality, which is linked to the physical information content. In particular, it has been demonstrated that the availability of acoustic information from both the particle's front and back surface is a necessary condition for good quality data for cross-section imaging. It is concluded that all the imaging methods tested in this work are in principle capable of delivering image quality, provided the data are of sufficient quality. What set them apart are the substantial differences in computational costs and the ability to process different types of data.

It has also been shown that the smooth plastic materials show little scattering and the reflection of waves played the dominant role in the collected data. In particular, for cross-section imaging, the detected reflected waves were strongly angle-restricted due to Snell's law at the smooth plastic surfaces. It has been shown that critical refraction occurring at the particle front surface will prevent the effective penetration of compressional waves into the particle interior, which renders it impossible to image the particle back surface. For polyolefin particles the critical refraction angle is around 38°. In such case, another data acquisition strategy is required that can enhance the effective aperture of the collected data.

Recommendations for industrial implementation of ultrasound technology have been compiled in the next section.

7.2. *Recommendations*

With regards to the deployment of the ultrasound techniques in industrial waste processing, the following recommendations are derived from this research:

Imaging methods: Each imaging method tested in this work is in principle capable of delivering image quality. The main difference lies in the computational burden and the type of data it can handle. Since image quality is closely connected to the quality of the data, different data acquisition scenarios may require different imaging methods.

Data quality: The data quality is determined by wave accessibility to the target surface or detail in question, range of viewing angles on the target, bandwidth and SNR. This determines and limits the possibilities for accurate imaging of details and object cross-sections. The choice of sensors (arrays) and their strategic positioning requires due consideration.

Physical accessibility: Improved access of the probe (using smaller probes or adaptations of the MDS channel design) allows the data to be scanned with different views on the particle streams, offering more quantitative information on particles and stream profile. For example, positions 2a/2b in Table 2.1 offer a potentially higher capacity and redundancy for studying particles, but these positions were unobtainable in this research.

Acoustical accessibility: Common conveyor belt materials cannot be penetrated by the used frequencies of acoustical waves. However, thinner polymer materials exist of which the impedance is closer to that of water, which possibly allows acoustic imaging to be conducted through the conveyor belt. This could solve part of the accessibility problem for the MDS channel.

Dual arrays: A combination of two fixed linear arrays placed under an angle (cf. Figure 6.14) increases the synthetic aperture and may overcome critical angle shielding observed for low-scattering plastic particles and it facilitates reliable cross-section imaging. The setup in Figure 6.14 also allows transmission data to be scanned, which may allow for more methods delivering more accurate identification of plastic properties.

Matrix arrays: Observation and studying of particle behaviour and trajectories is improved by the 3D viewing space offered by 2D matrices. For that purpose any of the imaging methods studied in this thesis may be extended to 3D imaging.

Doppler imaging: The motions of particles may in principle be studied in two or even three dimensions using Doppler ultrasound techniques. This presents an essential tool for diagnosis of the flow problems such as turbulence. The best detectable motions of the particle will be more or less in the direction toward (or away from) the sensor. In an MDS the sensor is preferably located at the bottom or top of the channel to prevent it from causing flow turbulence. This will give an excellent detection of up or downward particle motions, but a much less good detection of horizontal motions. Surface scattering may enlarge the range of detectable angles, but unfortunately plastic materials show little scattering. Scattering is determined based on the ratio of the wavelength to the scatterer size. An alternative to enhance scattering is to use larger wavelengths (lower frequencies). However, a compromise should be made between enhancing scattering and resolution since the larger wavelengths have the disadvantage of lowering the imaging resolution.

Promoting surface scattering: Scattering improves the image quality for cross-section imaging as it increases the accessibility to target surfaces and does not suffer from the critical angle shielding as do plane waves. However, most plastics show relatively little surface scattering, probably because of the smooth polymer build up of the material and the high acoustic absorption. Possible options to improve scattering, if affordable, are to apply peening to the particles using small glass beads, or to strongly adhere fine particles to its surface. This may be helpful, for example if the objective is to study particle trajectories in an MDS.

Appendices

A: Fourier transform

A.1. Fourier integral

The basis of Fourier analysis of a continuous non-periodic signal $f(t)$ is the Fourier integral transform, defined as

$$F(\omega) = \int_{-\infty}^{+\infty} f(t) \exp(-i\omega t) dt, \quad \text{Eq. (A.1)}$$

where ω is the angular frequency. The inverse transform is given by

$$f(t) = 1/2\pi \int_{-\infty}^{+\infty} F(\omega) \exp(i\omega t) d\omega. \quad \text{Eq. (A.2)}$$

A.2. Discrete Fourier Transform (DFT)

The direct output of an ultrasound sensor is an analogue electrical time signal. In the acoustic data collection, the electric signals are digitized so that time samples can be used for processing by computer. In that case, the digitised signals should be processed by the discrete version of the Fourier transform. According to the DFT formulation, a sequence of N complex numbers $x[0], x[1], \dots, x[N-1]$ are transformed into an N -periodic sequence of complex numbers $X[0], X[1], \dots, X[N-1]$:

$$X[k] = \sum_{n=0}^{N-1} x[n] \exp(-i2\pi kn/N). \quad \text{Eq. (A.3)}$$

The inverse discrete Fourier transform is given by

$$x[n] = \frac{1}{N} \sum_{k=0}^{N-1} X[k] \exp(i2\pi kn/N). \quad \text{Eq. (A.4)}$$

A.3. Parseval's theorem for DFT

For discrete functions, the relation between power computed in the time domain and the same power computed in the frequency domain is given by:

$$\sum_{n=0}^{N-1} |x[n]|^2 = \frac{1}{N} \sum_{k=0}^{N-1} |X[k]|^2. \quad \text{Eq. (A.5)}$$

To prove this relation, the left hand side is expanded using Eq. (A.4) as follows:

$$\begin{aligned} \sum_{n=0}^{N-1} |x[n]|^2 &= \frac{1}{N} \sum_{n=0}^{N-1} x[n] \sum_{k=0}^{N-1} X[k] \exp(i2\pi kn/N) \\ &= \frac{1}{N} \sum_{k=0}^{N-1} X[k] \sum_{n=0}^{N-1} x[n] \exp(i2\pi kn/N) \\ &= \frac{1}{N} \sum_{k=0}^{N-1} X[k] \cdot \bar{X}[k] \\ &= \frac{1}{N} \sum_{k=0}^{N-1} |X[k]|^2. \end{aligned} \quad \text{Eq. (A.6)}$$

B: Evaluation of complexity for imaging algorithms

In Section 5.9, computational cost analysis was presented for the different imaging algorithms. In this Appendix the details for the evaluation of complexities given in Table 5.1 and 5.2 are presented. The idea is to express the complexity of an algorithm as a function of the input data rather than indicating execution time. To that end, the effectiveness of an algorithm can be studied by monitoring the growth of number of arithmetic operations as the size of the input data tends toward infinity. Here, the complexity of an operation is denoted by big-*O* notation in the following analysis.

For each element position, N_t time samples are recorded, corresponding to time instants t_1, t_2, \dots, t_{N_t} . The measurement is repeated at N_x different positions along the x -axis corresponding to x_1, x_2, \dots, x_{N_x} . This discrete input data set has the structure of a 2D matrix of size $N_t \times N_x$ expressed by $\mathbf{D}_{t,x}[y_0]$. After an initial Fourier transform to (k_x, ω) domain, the result denoted by $\mathbf{D}_{k_x, \omega}[y_0]$ is also a 2D matrix of the same size $N_t \times N_x$. The number of extrapolation lines to depth y , and the number of k_y are denoted by N_y and N_{k_y} respectively, and are proportional to N_t . For some simplicity in complexity analysis, we may ignore such proportionality constants and assume $N_t = N_y = N_{k_y} = N$.

We analyze the algorithms in the following order: Stolt, F-SAFT, phase shift migration and NSPS as their order of complexity increases from one to the other. The initial Fourier transform from (x, t) to (k_x, ω) is a two-dimensional transform which is a common step in all the algorithms. We assume that FFT is employed as an efficient method for computing the forward discrete Fourier transform (DFT) and also for its inverse transform. The complexity of this transform is $O(N_x N \log N_x N)$. In Stolt migration, the calculation of $\mathbf{D}_{k_x, \omega}[y_0]$ is followed by an interpolation step. The complexity of this step is $O(N_x N)$.

Multiplication with the Jacobian of the transform is $O(N_x N)$, and the final 2D inverse Fourier transform to produce the image is $O(N_x N \log N_x N)$.

For the F-SAFT algorithm, the wave field $\mathbf{D}_{kx, \omega}[y_0]$ is multiplied by a phase-shift factor to backpropagate the field to the depth y . This multiplication is performed N times, once for each image line, and thus the complexity for all image lines is $O(N_x N^2)$. The summation over ω is also performed N times, resulting in a total complexity of $O(N_x N^2)$. Finally, the last operation is the inverse Fourier transform of a N_x length vector, which is also repeated N times and thus the complexity is $O(N_x N \log N_x)$.

For the phase shift migration, $\mathbf{D}_{kx, \omega}[y_0]$ data has to be first multiplied with a phase-shift factor to calculate $\mathbf{D}_{kx, \omega}[y_{particle}]$ which is the field at the boundary interface between ferrofluid and the plastic particle. This operation is performed only once and its complexity is $O(N_x N)$. All other steps for phase shift migration are exactly the same as for the F-SAFT algorithm.

In NSPS each image line is composed of two real wave velocities, which are those for the ferrofluid and plastic. First, $\mathbf{D}_{kx, \omega}[y_0]$ data is backpropagated to the depth y and this operation is performed twice (corresponding to the two distinct wave velocities of ferrofluid and plastic). Therefore, the complexity of this operation for all the imaging lines is $O(2N_x N^2)$. The field data is subjected to a double inverse Fourier transform, and the windowing function assigns the wave field to corresponding spatial values to get $\mathbf{D}_{x, \omega}[y]$. This operation is done for all the image lines and all ω and its complexity is given by $O(2N_x N^2 \log N_x)$. This field is then Fourier transformed to get $\mathbf{D}_{kx, \omega}[y]$, which has a complexity of $O(N_x N^2 \log N_x)$. Finally, the wave field $\mathbf{D}_{x, \omega}[y]$ is summed over ω to get the final image which complexity is $O(N_x N^2)$.

Summary

This thesis is dedicated to an investigation of the potential and technological possibilities of an inline ultrasound system as a quality control system for wet recycling of solid waste. The main targeted recycling technology is *magnetic density separation (MDS)*, a novel technique that was investigated and technologically matured in a project running in parallel to this work. In MDS, the easily magnetisable ferrofluid is used as the separation medium to sort different materials based on their mass densities. The MDS is very accurate compared to conventional recycling separation techniques as it is effective even when the densities are very close (< 1 weight percent), such as for different polyolefin plastics. The special attention for plastics in this work is motivated by the economical and environmental gains that are obtained from the separation of plastics from large waste flows such as automobile scrap and household waste. Due to the inherent optical opaqueness of ferrofluid, the ultrasound imaging system is the only effective method that allows accurate observation and study of the waste particles as they separate in the channel. Moreover, the intrinsic properties of ultrasound make it suitable for quantitative analyses, such as particle tracking and measurement of particle sizes, volume and density distributions as the particles flow in large quantities towards the extraction units.

The main objectives for this work have been achieved. It was shown that commercial medical 2D ultrasonic imaging systems provide a good technological point of departure for the desired inline system. They are capable of generating good quality images of moving particles, provided the view of the probe onto the particles is well controlled. Moreover, it has been shown that real-time ultrasound is capable of delivering online quantitative information that is crucial to the performance of an MDS. In particular, image processing techniques have been applied on the real-time ultrasound video-streams to evaluate the particles density distribution in the channel, measure the particle velocity and to analyze their motion behaviour as they float in the ferrofluid. The limitations of the medical commercial technology are that it cannot serve as a reliable stand-alone machine and also cannot provide all types of quantitative analyses that are desirable in an industrial recycling operation.

As a next step, the investigation turned towards the imaging methods themselves. For that purpose the general linear acoustic theory for waves in ferrofluids and acoustic imaging was reviewed, first to establish the basic physics and main principles of imaging. The potential of quantitative ultrasound analysis was determined by focusing on cross-section imaging, which is the biggest challenge for accurate 2D imaging. It has been shown that probe positioning and the overall data acquisition strategy deserve due consideration, since data quality proved paramount for good quality images.

For the imaging research, the most technologically promising ultrasound methods were adapted from the fields of seismology, medical ultrasound and non-destructive testing. These imaging methods were developed in either the space-

time domain or the Fourier domain, as each approach proved to have its own advantages and limitations for data requirements and computational costs. The methods were implemented in Matlab and supplied with raw ultrasound data, scanned from static scenes with just a few generic test objects. These objects were generic in the sense that all possible shapes and size-dependent acoustic wave effects were captured that could be expected with 'real' waste particles. Two complementary data sets were used to investigate the possible benefits of having either a wider sensor array aperture during transmission (pulse-echo data) or during data reception (plane wave data). The resulting images were evaluated in terms of performance indicators, which were introduced to obtain a more objective judgement of image quality. This research showed that accurate ultrasound cross-section imaging is quite feasible if good quality data can be scanned, i.e. if the data contain the necessary acoustic information. In particular, the availability of acoustic information from both front and back surfaces was found to be the key factor for good quality data. It is also concluded that all the imaging methods tested in this work are in principle capable of delivering good image quality, provided the data are of sufficient quality. What sets them apart are the substantial differences in computational costs and the ability to process different types of data.

Finally, the research conducted in this thesis has also led to the compilation of a set of recommendations for future realization of an ultrasound system, dedicated to inline quality control in recycling.

Samenvatting

Dit proefschrift is gewijd aan onderzoek naar de impact en de technologische mogelijkheden van een inline ultrasoon inspectiesysteem voor kwaliteitscontrole in natte recycling van vast afval. Meer specifiek, de beoogde toepassing is magnetische dichtheidsscheiding (MDS). Dit is een nieuwe techniek die werd onderzocht en technologisch doorontwikkeld in een project dat parallel liep met dit werk. In MDS wordt een gemakkelijk magnetiseerbare ferrovloeistof gebruikt als scheidingsmiddel om materialen op basis van massadichtheid te sorteren. MDS is veel nauwkeuriger dan conventionele scheidingstechnieken voor recycling, en kan zelfs toegepast worden wanneer de dichthesen zeer dicht bij elkaar liggen (<1 gewichtsprocent), zoals bij de verschillende typen polyolefine kunststoffen. De speciale aandacht voor kunststoffen in dit werk komt voort uit de economische en ecologische voordelen van de scheiding van kunststoffen uit grote afvalstromen zoals autoschroot en huishoudelijk afval. Ferrovloeistof is compleet ondoorzichtig, waardoor het ultrasone beeldvormingsysteem de enige effectieve en efficiënte methode is om nauwkeurige observaties te kunnen verrichten en tegelijkertijd onderzoek te kunnen doen naar de scheidingsprocessen in het MDS kanaal. Bovendien maken de intrinsieke eigenschappen van ultrageluid kwantitatieve analyses mogelijk, zoals het volgen van deeltjes en het meten van grootte, volume en dichtheidsverdelingen terwijl de deeltjes in grote hoeveelheden naar de extractie-eenheid stromen.

De belangrijkste doelstellingen (zie Hoofdstuk 1) voor dit werk zijn bereikt. Er is aangetoond dat commerciële medische 2D ultrasone beeldvormende systemen een goed technologisch uitgangspunt bieden voor het gewenste inline systeem. Zij kunnen beelden van goede kwaliteit genereren van bewegende deeltjes, mits de observatiehoeken tussen de probe op de deeltjes goed wordt gecontroleerd. Bovendien is aangetoond dat real-time ultrageluid kwantitatieve informatie kan leveren die cruciaal is voor de prestatie van een MDS. Beeldbewerkingstechnieken werden toegepast op real-time ultrasone videotracks om de dichtheidsverdeling van de deeltjes in het kanaal te evalueren, de deeltjessnelheid te meten en hun beweging te analyseren wanneer zij in de ferrovloeistof voorbij stromen. De beperkingen van de medische commerciële technologie zijn dat het niet in een betrouwbare stand-alone machine werkt en ook niet voor verschillende soorten kwantitatieve analyses toepasbaar is die wenselijk zijn voor industriële recycling.

In een volgende stap concentreerde het onderzoek zich op de beeldvormende methoden zelf. Voor dit doel werd de algemene lineaire akoestische theorie voor golven in ferrovloeistoffen en akoestische beeldvorming ontwikkeld, om in eerste instantie de fysische basis en belangrijkste principes van beeldvorming vast te stellen. Het potentieel van kwantitatieve ultrasone analyse werd bepaald door te focussen op het afbeelden van doorsneden van plastic deeltjes. Dit vormt tegelijkertijd de grootste uitdaging voor nauwkeurige 2D beeldvorming. Het is aangetoond dat de positionering van de sonde en de algemene strategie van de data-acquisitie extra aandacht verdienen. Dit door het feit dat de

kwaliteit van de ruwe data grote invloed heeft op de uiteindelijke kwaliteit van de beelden.

Voor het onderzoek aan de beeldvorming werden de technologisch meest veelbelovende ultrasone technieken geadaptiert uit de seismologie, de medische echografie en het niet-destructief onderzoek. Aangezien elke aanpak zijn eigen voordelen en beperkingen heeft en andere eisen stelt aan data en rekenkracht, werden deze methoden van beeldvorming ontwikkeld in zowel het ruimte-tijd domein als ook het Fourier domein. De methoden werden in Matlab geïmplementeerd en met ruwe ultrasone data gevoed, welke is gescand van statische scènes met slechts een paar generieke testobjecten. Deze objecten waren generiek in de zin dat alle mogelijke vormen en grootteafhankelijke akoestische golfeffecten die verwacht kunnen worden met 'echte' afvaldeeltjes gesimuleerd konden worden. Twee complementaire datasets werden gebruikt om de voordelen te onderzoeken van een bredere sensor aperture tijdens het zenden (pulse-echo data) als ook tijdens ontvangst (vlakke golf data). De resulterende beelden werden geëvalueerd in termen van prestatie indicatoren om een objectieve beoordeling van de beeldkwaliteit te verkrijgen. Dit onderzoek toonde aan dat een nauwkeurig ultrasone afbeelding van een doorsnede goed haalbaar is zo lang de data met goede kwaliteit worden gescand en de nodige akoestische informatie bevatten. In het bijzonder werd gevonden dat de beschikbaarheid van akoestische informatie van de gehele voorzijde en achterzijde van een deeltje een cruciale factor vormden om beeldkwaliteit te garanderen. Er is ook geconcludeerd dat alle beeldvormende methoden die in dit werk getest zijn in principe in staat zijn om goede beeldkwaliteit te leveren, mits de ruwe data van voldoende kwaliteit zijn. Wat de methoden onderscheidt zijn de vereisten qua beschikbare rekenkracht en de mogelijkheid om verschillende soorten data te verwerken.

Ten slotte heeft het onderzoek in dit proefschrift ook geleid tot het opstellen van een reeks aanbevelingen voor de toekomstige realisatie van een ultrasoon systeem dat toepasbaar is voor inline kwaliteitscontrole in de recycling industrie.

Acknowledgement

I would like to express my gratitude and acknowledgment to all the people who have supported me during my PhD work at Delft University of Technology during the last years.

I am very grateful to my supervisor Dr. Maarten Bakker for his continuous guidance, advice and scientific discussions during the development of this work. This research work has integrated ultrasound imaging technology and wet solid waste processing techniques to form a high quality multidisciplinary field of activity. I would like to thank my promoters for their important comments and scientific feedback on these two fields. In particular, I would like to thank my promoter Professor Peter Rem for providing valuable advice and guidance for analyzing the technological issues regarding the plastics recycling. I would like to also express my appreciation and gratitude to my promoter Professor Kees Wapenaar for his precious comments on the acoustical point of view including wave equation redatuming and migration techniques. I would like to thank the members of the doctoral committee for their willingness to review and judge my work.

This research was financially supported by the European Commission in the framework of FP7 collaborative project “Magnetic sorting and ultrasound sensor technology for production of high purity secondary polyolefins from waste (W2Plastic)”. I would like to thank Oldelft Ultrasound for their support in developing the ultrasound hardware. Herewith, I would like to also express my gratitude to all other Work Package members of the W2Plastic project for their pleasant collaboration and feedback. Indeed, it was quite a nice feeling and good experience to work on such a large-scale and complex project with international partners from different parts of Europe.

The past few years have formed quite a special period in my life. The present work has been the first implementation of a quantitative ultrasound imaging system designed for recycling. It has opened an entirely new application field of ultrasound and therefore it demanded new ideas and perspectives on ultrasound technology. This created a lot of interesting technological challenges for me which I faced during my PhD work. On the other hand, my social life has also been quite interesting and pleasant in the Netherlands. I have got to know many nice people and colleagues in the university who made me enjoy the research work even more. I am really grateful to all the colleagues in the Resources & Recycling group for their company and support both on a professional level and also personal level and all the nice conversations we had at the office. My appreciation goes to Francesco Di Maio, Peter Berkhout, Mohamed Khodabaks, Guus Lohlefink, Ron Penners, Claudia Baltussen, Abdur Rahman, Somi Lotfi, Walter de Vries, Bin Hu, Valentina Luciani and Han Xia. I would like to thank Jinga Vlad for his nice company and help during the experimental ultrasound measurements we performed together. I would like to also thank my good friends: Hooman, Ali, Sadegh, Reza, Mohamad and all my other nice friends in Delft.

Finally, my lovely family has been quite supportive to me to deliver this work in the present form. Indeed, I am so happy and lucky to have the best mother Minoo and the best father Ahmad in the world. They have given me the ultimate kindness and they have been always giving much attention to my professional development. I am also very grateful to my kind aunt Maryam for thinking and caring about me all the time. I really appreciate my nice and lovely sister Samira for her warm support.

Curriculum Vitae

Seyed Ali Sanaee was born on September 5, 1983 in Tehran. He did his high school education in the field of physics and mathematics at Danesh Nemoone Mardomi high school in Tehran and received his high school diploma in 2001. Soon after his high school education, he was awarded the Japanese Government Scholarship Program (Monbukagakusho: MEXT) to study at Japanese universities. This offer motivated him to pursue his university education in Japan and also to experience a different culture and obtain an international background.



In April 2002, he entered Tokyo University of Foreign Studies where he took an intensive Japanese language course for one year. This resulted in a diploma in Japanese language proficiency in March 2003.

In April 2003, he entered Tohoku University in Sendai city and took courses in the School of Engineering, in the field of Mechanical Engineering. In April 2005, he joined the System Robotics Laboratory where he was trained in basics of robotics engineering such as controlling the 6-degree of freedom robotic manipulators in real-time. His graduation thesis concerned the manipulator control based on a joint torque feedback and the research was conducted at the System Robotics Laboratory. He received his Bachelor degree in March 2007 and then soon in April 2007 he entered the Graduate School of Engineering at Tohoku University for continuing his master studies in the field of Mechanical Engineering. He worked on ultrasound measurement techniques for characterization of cast iron materials. His master graduation thesis was about modeling of acoustic properties for graphite dispersed metals and fundamental investigation for its application to non-destructive testing. In November 2008, he received a presentation award from The Japanese Society for Non-destructive Inspection for his research results. His academic achievements in the end resulted in a Master degree in Mechanical Engineering in March 2009.

From February 2009 to the present, he is working as a PhD researcher at the group of Resources and Recycling at the Faculty of Civil Engineering and Geosciences at Delft University of Technology in the Netherlands. His PhD research was funded by the European Commission in the framework of FP7 collaborative project “Magnetic sorting and ultrasound sensor technology for production of high purity secondary polyolefins from waste (W2Plastic)”. In particular, his research was concerned about the development and investigation of a quantitative ultrasound measurement system for application in recycling of plastic materials which has led to this PhD thesis.

List of publications

1. Seyed Ali Sanaee and M. C. M. Bakker, “Ultrasound imaging techniques in density separation of polyolefin waste”, *Environmental Technology*, vol. 33, no. 22, pp. 2585-2593, November 2012.
2. Seyed Ali Sanaee and Maarten C. M. Bakker, “Ultrasound Imaging for Quantitative Measurement of Immersed Plastic Waste Particles”, *The Proceedings of 18th World Conference on Nondestructive Testing*, April 16-20, 2012, Durban, South Africa.
3. S. A. Sanaee and M. C. M. Bakker, “Ultrasound Techniques for Control and Quantitative Measurements in Density Separation of Polyolefins” ,*Proceedings of the International Conference on Solid Waste 2011-Moving Towards Sustainable Resource Management*, May 2-6, 2011, Hong Kong SAR, P. R. China.
4. S. A. Sanaee and M. C. M. Bakker, “Ultrasound for Characterization of Recycled Concrete”, *The Abstract Proceedings of The 12th PhD Symposium Research School Integral Design of Structures*, December 2-3, 2010, Zeist, The Netherlands.
5. M. C. M. Bakker and S. A. Sanaee, “Capabilities of Ultrasound for Monitoring and Quantitative Analysis of Polyolefin Waste Particles in Magnetic Density Separation (MDS)”, *The Open Waste Management Journal*, Vol. 3, pp. 117-126, 2010.
6. Seyed Ali Sanaee and Maarten Bakker, “Ultrasound For Monitoring And Quality Inspection In MDS Plastics Recycling”, *The Proceedings of The ISWA World Congress*, October 12-15, 2009, Lisbon, Portugal.
7. Seyed Ali Sanaee, Tetsuya Uchimoto, Toshiyuki Takagi and Hak-Joon Kim , “Evaluation of graphite forms in flake graphite cast irons by acoustic testing” ,*Proceedings of The conference of The Japanese Society for Nondestructive Inspection (JSNDI)*, November 2008, Sendai, Japan.
8. Seyed Ali Sanaee, Tetsuya Uchimoto, Toshiyuki Takagi and Hak-Joon Kim , “Evaluation of graphite forms in flake graphite cast irons by acoustic testing” , *Proceedings of the Eighth International Symposium on Advanced Fluid Information and Transdisciplinary Fluid Integration (AFI/TFI-2008)*, December 19-20, 2008, Sendai, Miyagi, Japan.

